Antiferromagnetic Dipolar Ordering in $[Co_2MnGe/V]_N$ Multilayers

DISSERTATION

zur Erlangung des Grades eines Doktors der Naturwissenschaften
der Fakultät für Physik und Astronomie an der
Ruhr-Universität Bochum

vorgelegt von

Andre Bergmann

Bochum 2006

Mit Genehmigung des Dekanats vom 24.03.2006 wurde die Dissertation in englischer Sprache verfasst.

Mit Genehmigung des Dekanats vom 24.03.2006 wurden Teile dieser Arbeit vorab veröffentlicht. Eine Zusammenstellung befindet sich am Ende der Dissertation.

Erstgutachter: Prof. Dr. K. Westerholt
Zweitgutachter: Prof. Dr. Dr. h.c. H. Zabel
Tag der Disputation: 23.06.2006

Contents

Contents

Contents

4

1. Introduction

In recent years an upsurge of interest has been noticed in the new material class of ferromagnetic metals with 100% spin polarization, so called half-metals, since they have the potential to play an important role in the rapidly evolving field of magneto-electronics (spintronics) [1, 2, 3]. The half-metallicity has first been predicted 1983 by de Groot et al. for the half-Heusler alloy NiMnSb. For a long time the half-metals were considered as exotic ferromagnets of mainly academic interest. This attitude has changed completely with the appearance of the new field of spintronics. While in conventional electronics the charge of the electrons plays the essential role, spintronic devices are designed to control both the charge current and the spin current of the electrons in one single functional unit. Ferromagnetic half-metals with only one spin direction at the Fermi level are ideally suited as electrodes in these devices, e.g. for spin injection into semiconductors, spin filtering, or in giant magnetoresistance (GMR) and tunneling magnetoresistance (TMR) applications. This should support the design of non-volatile magnetic random access memories (MRAM), since a high TMR ratio is a key parameter for the magnetic tunnel junctions building the MRAM cells.

In the last 10 years a lot of materials have been predicted theoretically to have half-metallic character, among them are some oxides (e.g. CrO_2 and Fe_3O_4) [4], the manganites (e.g. $La_{0.7}Sr_{0.3}MnO_3$) [4], the diluted magnetic semiconductors (e.g. GaAs or ZnO doped with magnetic transition metal ions) [5, 6] and the fully spin polarized Heusler alloys, which are the subject of the present thesis. Heusler alloys are ternary intermetallic compounds with the general composition A_2BX, A and B being transition metal atoms and X a non-magnetic atom. The fully ordered Heusler structure is a cubic lattice with four interpenetrating fcc sublattices occupied by A, B or X atoms ($L2_1$ structure). Recent intense theoretical investigations using energy band structure calculations predicted more than 20 different Heusler phases to exhibit half-metallic behaviour until now [7, 8, 9, 10, 11]. The most prominent are the half-metals NiMnSb and PtMnSb (so-called half-Heusler compounds, since one A sublattice is empty), the pseudo-ternary phase $Co_2Cr_{0.6}Fe_{0.4}Al$, and the phases Co_2MnSi and Co_2MnGe. Currently the half-metallic Heusler phases are considered to be the most attractive candidates for application in

1. Introduction

spintronic devices, since they exhibit extremely high Curie temperatures (905 K for Co$_2$MnGe) and a structure, which is closely related to conventional semiconductors.

Regardless of these promising properties of the Heusler half-metals experimental investigations in the last years revealed that it is very difficult to realize the predicted full spin polarization even in single crystals. The performance of TMR devices using Heusler thin films as an electrode has been somewhat disappointing at first. NiMnSb integrated into a magnetic tunnel junction showed only 25% spin polarization at 4.2 K [12]. Later these results could be improved and actually the highest value obtained for spin polarization in a MTJ using a Co$_2$MnSi electrode is 89% [13, 14]. However, irrespective of the experimental method applied to determine the degree of spin polarization quantitatively, it is always definitely less than 100%. The main reason, which has been suggested for this reduction, is site disorder in the film and at the interfaces, since only the perfectly ordered Heusler alloy exhibits a gap in the minority spin band [15, 16]. Interfaces in thin film heterostructures combining the Heusler alloys with other materials are of utmost importance for spintronic devices, since the spin polarization has to be stable down to the first few monolayers of the interface. However, these compounds are prone to interdiffusion and site disorder, which both have the tendency to suppress the full spin polarization [15, 16].

Within the framework of this thesis a systematic investigation of single thin films of the Heusler phase Co$_2$MnGe and subsequently metallic multilayers of Co$_2$MnGe combined with other metals like V, Au and Cr [17] has been carried out. The aim of this research has been twofold. On the one hand, high quality multilayers or superlattices are ideally suited to study the structural quality of interfaces by x-ray or neutron reflectivity methods. On the other hand, the basic question should be answered whether an oscillatory interlayer exchange interaction (IEC), which exists in most magnetic/nonmagnetic multilayer systems of the transition metals [18], can also be observed in Co$_2$MnGe based multilayers. This is interesting both from the fundamental point of view and also for potential application in magneto-electronic devices. If an interlayer coupling could be realized, the preparation of antiferromagnetically coupled multilayers with a large GMR effect would be possible.

In fact, of the many different multilayer systems studied up to now in our group [17], only the [Co$_2$MnGe/V] system showed first indications from magnetization measurements that an antiferromagnetic interlayer coupling might exist.

This thesis presents a detailed investigation of the structural and magnetic properties of [Co$_2$MnGe/V] multilayers with variable thickness of the V layers and investigates in detail their magnetic ordering. It will turn out that the interlayer magnetic ordering in

the multilayers is unconventional and definitely different from the IEC mechanism. The magnetic order is directly related to peculiarities of the magnetism in very thin Heusler layers.

In this thesis first conventional x-ray scattering was used to determine the structural properties of the [Co_2MnGe/V] multilayers. Since the ferromagnetism and the half-metallic character of the thin Heusler layers might be lost at the interfaces due to disorder and interdiffusion, it is valuable to resolve the magnetization profile or the magnetic moment density profile. For this purpose systematic investigations of the Heusler multilayers with x-ray resonant magnetic scattering (XRMS) using synchrotron radiation in the soft x-ray regime have been carried out. XRMS combines the depth-resolving power of conventional x-ray reflectivity with the element sensitivity of the x-ray resonant scattering with circular polarized light [19, 20]. By tuning the energy to the Co and Mn $L_{2,3}$ edges, the element specific magnetization depth profile across the interface to the non-ferromagnetic layer can be determined. As a complementary tool magnetic neutron scattering has been applied on the multilayers. While resonant x-ray scattering is sensitive to the atomic magnetic moment, neutrons probe the magnetic induction in the sample. Spin polarized neutron reflectivity has been irreplaceable for the analysis of vector magnetization profiles, magnetic domain distributions and for the proof of antiferromagnetic coupling in the [Co_2MnGe/V] multilayers.

The present thesis is divided into three parts: The first part introduces the basics for the understanding of the physical properties of the [Co_2MnGe/V] multilayers studied here. An overview of the general properties of Heusler alloys is given in Chap. 2. Recent applications in spintronic devices and the open questions will be discussed besides the structural, magnetic and electronic properties. Chap. 3 gives an introduction to spin glasses, whose characteristics turn out to be important for the understanding of the magnetization measurements of the [Co_2MnGe/V] samples. The second part of the thesis explains the experimental scattering methods used. After a theoretical introduction specular reflectivity and off-specular diffuse scattering is discussed both for the case of neutron scattering (Chap. 4) and resonant soft x-ray scattering (Chap. 5). The experimental results on the Co_2MnGe based single layers and multilayers are presented in the third part of the thesis. First, the measurements on single very thin Co_2MnGe layers are reported (Chap. 6). Their structural quality and magnetic properties are needed for an understanding of the structural and magnetic properties of the [Co_2MnGe/V] multilayers presented in Chap. 7. Conclusions and a summary are provided in Chap. 8.

1. Introduction

Part I.

Basics

2. Heusler Alloys

The Heusler compounds have a long history in magnetism, starting more than 100 years ago with the detection of the ternary metallic compound Cu_2MnAl by A. Heusler in 1903 [21]. Remarkably, this alloy is a ferromagnet even though none of its constituents is one. Further investigations showed that a whole class of isostructural ternary metallic alloys with the general composition X_2YZ exists, where X denotes a transition metal element such as Ni, Co, Fe or Pt, Y is a second transition metal element, e.g. Mn, Cr or Ti and Z is an atom from 3rd, 4th or 5th group of the periodic system such as Al, Ge, Sn or Sb. More than 1000 different Heusler compounds have been synthesized until now, a comprehensive review of the experimental work until the year 1987 can be found in Ref. [22]. They attracted considerable interest due to their very versatile magnetism. Actually the driving force for the intense study of the Heusler compounds is the predicted half-metallic ferromagnetic nature for some of these alloys [7, 10, 23, 24, 25]. Half-metals are particular ferromagnetic materials, which can be considered as hybrids between metals and semiconductors. They possess an energy gap for one spin direction at the Fermi level (E_F) leading to a complete spin polarization at E_F. This makes them ideal candidates for the application in spintronics.

This chapter gives a short review of the structural, magnetic and electronic properties of the Heusler compounds in general with emphasis on the half-metallic Heusler alloys, especially the Co-based ones, since Co_2MnGe is the alloy studied within this thesis. After the basic properties of the bulk Heusler compounds are discussed, some of the recent results in spintronic applications and the open problems are presented.

2.1. Structural Properties

The Heusler alloys are defined as ternary intermetallic compounds with the stoichiometric composition X_2YX and the crystal structure $L2_1$. Moreover there exist so-called half-Heusler phases with the general formula XYZ, having $C1_b$ structure. The $L2_1$ or $C1_b$ structure, respectively, is most important for the predicted half-metallic properties of the Heusler compounds, since the theoretical band structure calculations usually re-

fer to this structure. The $L2_1$ unit cell is depicted in Fig. 2.1. It can be imagined to be combined of four interpenetrating fcc sublattices occupied by X, Y and Z atoms, respectively. The sublattices are shifted along the space diagonal with the corner of the Z sublattice at (0,0,0), the first X sublattice at (1/4, 1/4, 1/4), the Y sublattice at (1/2,1/2,1/2) and the second X sublattice at (3/4, 3/4, 3/4). In the $C1_b$ structure the second X sublattice remains empty.
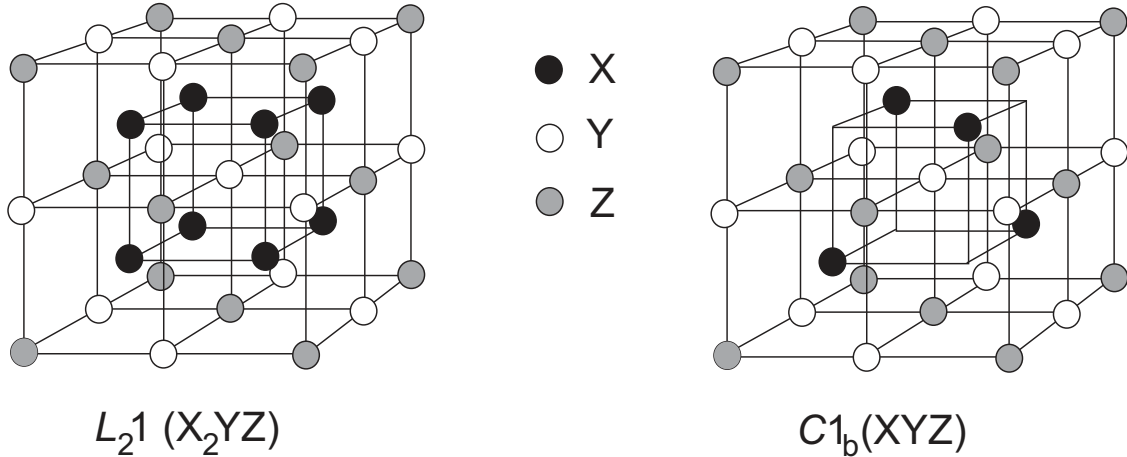
Figure 2.1.: Schematic representation of the $L2_1$ and the $C1_b$ structure.

For many Heusler compounds the ordered $L2_1$ structure is the low temperature equilibrium phase. In the majority of the Heusler alloys like the original Heusler phase Cu_2MnAl there exist several structural modifications with different degrees of site disorder of the atoms on the X, Y and Z position. At high temperatures the crystal structure is bcc with random occupation of the atoms on the lattice sites of a simple bcc lattice with half of the lattice parameter compared to the $L2_1$ structure. An intermediate structure with $B2$ symmetry occurs often for the Heusler compounds. It has the same lattice parameter as the $L2_1$ phase, but the Y and the Z atoms are distributed at random on the corresponding sublattices, whereas the two X sublattices remain intact.

2.2. Magnetic Properties

The magnetic phenomena of the Heusler alloys are very versatile and have been under continuous discussion all over the years. In the family of Heusler compounds there exists examples of itinerant and localized magnetism, antiferromagnetism, Pauli paramagnetism or heavy-fermionic behaviour.

The majority of the Heusler alloys with a magnetic element on the Y position or-

der ferromagnetically, but several antiferromagnetic compounds also exists, for instance Ni₂MnAl or Pd₂MnAl [26, 27]. The main contribution to the magnetic moments in the Heusler phases usually stems from the atoms at the Y position. If magnetic atoms also occupy the X positions, their moment is usually quite small or even vanishing. In the above mentioned Ni₂MnAl compound e.g. the Ni atoms are non-magnetic. Actually there exist a few Heusler compounds with rather large magnetic moments on both the X and the Y positions. In this case the ferromagnetic state is very stable and the ferromagnetic Curie temperature T_c becomes exceptionally high. The best examples are provided by the Heusler phases Co₂MnSi and Co₂FeSi with a Co moment of about 1 μB and Curie temperatures of 985 K [28] and 1100 K [29], respectively, the highest T_c values known for the Heusler alloys. The mechanism which stabilizes the ferromagnetism is a strong next-nearest neighbour ferromagnetic exchange interaction between the spins at the X and the Y position [7, 30]. If a non-magnetic element occupies the X position, the dominant exchange interaction between the Y spins is of weaker superexchange type due to hybridization, mediated by the electrons of the non-magnetic Z atoms. Depending on the valence of Z the interaction can have either sign [30].

Table 2.1.: Lattice constant, total spin moment and predicted spin magnetic moments of Co₂MnGe within the generalized gradient approximation (GGA) and experiment, taken from Ref. [24].

	a [nm]	μ_{tot} [μ_B]	μ_{Mn} [μ_B]	μ_{Co} [μ_B]	μ_{Ge} [μ_B]
experiment	0.574 [27]	5.11	-	-	-
theory	0.574	5.0	2.98	1.02	-0.03

The spin magnetic moments for Co₂MnGe are listed in Tab. 2.1. The Co atoms are ferromagnetically coupled to the Mn spin moments and they possess a spin moment of $\sim$ 1.0 μ_B. The Ge *sp* atom has a very small negative moment which is two orders of magnitude smaller than the Co moment. The orbital moments are almost completely quenched and their absolute values are negligible with respect to the spin magnetic moments [24, 31].

Heusler compounds such as Cu₂MnAl with a magnetic moment only on the Y position are considered as good examples of localized $3d$ metallic magnetism [30]. Since in the ideal $L2_1$ structure there are no Mn-Mn nearest neighbours, the Mn $3d$ wave functions overlap only weakly and the magnetic moments remain essentially localized at the Mn position. On the other hand, the compound Co₂TiSn with magnetic moments only on the X positions exhibits weak itinerant ferromagnetism with strongly delocalized mag-

netic moments [32]. As it is obvious from the crystallographic structure (Fig. 2.1), there are nearest neighbour X atoms making the overlap of the $3d$ wavefunctions and the delocalized character of the d electrons much larger than in the case of only the atoms at the Y position being magnetic. Replacing the Co atoms in Co_2TiSn by Ni, this delocalization effect proceeds further, making the compound Ni_2TiSn a Pauli paramagnet [33]. Even more interesting, the Heusler compounds Fe_2TiSn and Fe_2VAl also do not order magnetically, but are marginally magnetic. They belong to the rare class of transition metal compounds exhibiting heavy Fermion like properties in the low temperature specific heat and the electrical resistivity, which attracted much interest in the literature in recent years [34, 35, 36].

2.3. Electronic Properties: Half-Metallicity

The spectacular property of full spin polarization at the Fermi level E_F has first been detected in 1983 for the half-Heusler alloy NiMnSb by electron energy band calculations. Also PtMnSb and CoMnSb have been predicted to possess this property. NiMnSb, PtMnSb and CoMnSb have been dubbed half-metals [37], since only for one spin direction there is metallic conductivity, for the other spin direction the conductivity is of semiconducting type. In a ferromagnetic transition metal alloy this half-metallicity is a very rare property, since usually s or p bands with a small exchange splitting cross the Fermi energy and contribute states of both spin directions. For several years the half-Heusler alloys PtMnSb, NiMnSb and CoMnSb remained the only ferromagnetic alloys with half-metallic character, before starting from 1990 a second group of half-metallic Heusler alloys, Co_2MnSi, Co_2MnGe and $Co_2Mn(Sb_xSn_{1-x})$ has been found theoretically [23, 38, 39]. The calculated indirect band gap for the minority carriers is smaller in these materials than in the half-Heusler compounds [31], for Co_2MnSi and Co_2MnGe one derives $E_{gap} = 0.81$ eV and $E_{gap} = 0.54$ eV, respectively. The spin-projected density of states for Co_2MnGe is depicted in Fig. 2.2.

The origin of the gap in the minority spin band is rather subtle, but recently theoretical calculations allowed to reveal the basic mechanism for the formation of the gap. The $d-d$ hybridization between the transition atoms composing Heusler alloys is essential for the formation of the gap at E_F. In the case of half-Heusler compounds (e.g. NiMnSb) the gap is created by the hybridization and bonding-antibonding splitting between the Mn d and the Ni d states. In the case of full Heusler alloys (e.g. Co_2MnGe) the gap originates from the hybridization of the d states of the two Co atoms and the subsequent interaction of these hybrids with the Mn d states [40].
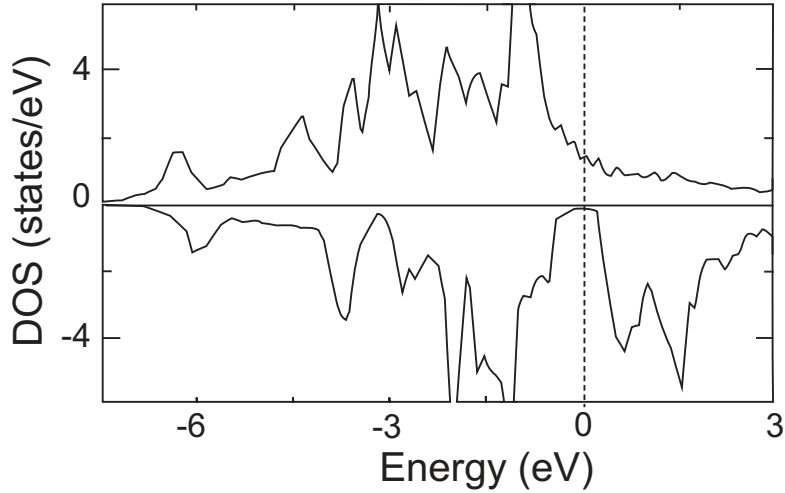
Figure 2.2.: Calculated spin-projected DOS for Co$_2$MnGe, taken from Ref. [24].

The experimental proof of half-metallicity in these Heusler alloys is a long and still ongoing controversial issue. The first attempts to prove the half-metallicity used electron transport measurement to test the existence of a gap in the spin down electron band [41, 42]. Since in the half-metal for temperatures small compared to the gap in the minority spin band there is only one spin direction at the Fermi level available, it is expected that electronic scattering processes involving spin flips and longitudinal spin wave excitations are inhibited. Thus one should expect an increasing electron mobility and a change of the power law describing the temperature dependence of the resistivity, when the thermal energy becomes smaller than the gap for the minority spin band. Actually for NiMnSb this type of behaviour for temperatures below 80 K has been detected. Additionally the Hall coefficient exhibits an anomalous temperature dependence in this temperature range, strongly suggesting a thermal excitation of charge carriers across a gap coexisting with metallic conductivity [41, 42]. More directly, positron annihilation experiments on bulk single crystals from the NiMnSb phase were found to be consistent with 100% spin polarization at the Fermi level [43], which could additionally be confirmed by infrared absorption experiments [44]. Finally, analyzing the current-voltage characteristic below the superconducting gap of a point contact between a Nb superconductor and a bulk PtMnSb sample, which is dominated by Andreev reflections at the ferromagnet/superconductor interface, the authors derived a spin polarization of 90% at the Fermi level [45].

For the Co$_2$Mn(Si,Ge,Sn) fully spin polarized group of Heusler compounds spin polarized neutron diffraction measurements on bulk samples have been employed to determine

the degree of spin polarization at the Fermi level [46]. This methods probe the spatial distribution of the magnetization, details of which depend sensitively on the spin polarization. The results suggest a finite density of states in the minority spin d band of manganese. Hence the spin polarization was found to be large, but not 100%. More recent superconducting/ferromagnetic point contact measurements on a Co_2MnSi single crystal gave a spin polarization of 55% [47]. Similarly, the degree of spin polarization determined from the analysis of spin resolved photoemission spectra was always found to be definitely below 100% [48, 49].

During the first years after the discovery of the half-metallic character in the Heusler compounds they were considered as exotic ferromagnets of mainly academic interest. This attitude has changed completely with the development of new ideas of data storage and processing designed to use both the charge and the spin degree of freedom of the conduction electrons, nowadays called spin electronics (spintronics) [50, 51, 52]. Adding the spin degree of freedom to conventional electronic devices has the advantages of non-volatility, increased processing speed and decreased electric power consumption [50, 53]. In the spintronic community there is a strong belief that in the future these new concepts have the perspective to complement or even substitute conventional Si technology. It was rapidly realized, how valuable it would be for spintronic devices to have a ferromagnet available with only one conduction electron spin direction at the Fermi level. With an electrode possessing 100% spin polarization the generation of a fully spin polarized current for spin injection into semiconductors would be very easy [54] and spin filtering and spin accumulation in metallic thin film systems would be most effective [55]. The giant magnetoresistance (GMR) [56] as well as the tunneling magnetoresistance (TMR) [57] of a device prepared of two half-metallic electrodes should be huge, since one spin direction is totally blocked to first order, if the two electrodes have an antiparallel magnetization direction.

The novel concepts of spintronics started an upsurge of interest in ferromagnetic half-metals in the literature. Besides the half and full Heusler alloys a large number of half-metallic materials has been found, among them are some oxides (e.g. CrO_2 and Fe_3O_4) [4], the manganites (e.g. $La_{0.7}Sr_{0.3}MnO_3$) [4], the transition metal chalcogenides (e.g. CrSe) and pnictides (e.g. CrAs) in the zinc-blende or wurtzite structures [58], the diluted magnetic semiconductors (e.g. GaAs or ZnO doped with magnetic transition metal ions) [5, 6] and the fully spin polarized Heusler alloys.

For technical applications the Heusler alloys seem to be very attractive for several reasons. Their crystal structure and lattice constant are closely related to the diamond and zinc-blende structure of most industrial relevant semiconductors, the lattice mismatch

is low, for instance for Co_2MnSi with GaAs it is less than 0.4% [59]. The preparation of Heusler thin films can be carried out by conventional metal film preparation methods, thus they are compatible with current semiconductor technology. A further advantage is their high ferromagnetic Curie temperature, even at room temperature the half-metallic Heusler alloys are close to ferromagnetic saturation. This is of particular importance, since the temperature dependence of the spin polarization scales with the corresponding magnetic moment of the material [60].

Recent intense theoretical investigations using electronic energy band structure calculations by theoretical groups increased the number of Heusler compounds with predicted half-metallic properties to more than 20, among them Co_2CrAl, Fe_2MnSi, Co_2CrAl, $Co_2Cr_{0.6}Fe_{0.4}Al$ and Co_2FeSi, to mention a few of the new compounds [7, 8, 9, 10, 11]. The experimental work in the literature mainly concentrated on the classical Heusler half-metallic phases NiMnSb and PtMnSb, the alloys Co_2MnSi and Co_2MnGe and the newly discovered compound $Co_2(CrFe)Al$ [9], leaving a vast field for further experimental investigations.

However, as already stated above the half-metallicity of the Heusler compounds is a subtle property which is easily lost in a real sample.

2.4. Heusler Half-metals in Devices

Presently the main motivation behind the experimental research on the fully spin polarized Heusler compounds in the literature is the promising application in spintronic devices. Hence it is obvious that thin films of the Heusler compounds are needed, bulk samples are not very useful. On the other hand, thin film preparation in general and especially the preparation of thin film heterostructures often imposes limits on the process parameters and this might severely interfere with the needs to have a high degree of spin polarization. For obtaining a large spin polarization a perfect crystal structure with a small number of grain boundaries is important. This can best be achieved by keeping the substrate at high temperatures during the thin film deposition. However, most Heusler phases grow in the Vollmer-Weber mode (three-dimensional islands) at high temperatures, thus when using high preparation temperatures there might be a strong roughening of the surfaces, which for spintronic devices is strictly prohibited. In addition, in thin film heterostructures combining different metallic, semiconducting or insulating layers with the Heusler compounds, high preparation temperatures are forbidden, since excessive interdiffusion at the interfaces must be avoided.

The half-metallic Heusler alloys are among the most promising materials to be inte-

grated as one magnetic electrode into technologically relevant magnetic tunnel junctions (MTJ). The effective amplitude of the magnetoresistance in a simple layered system, consisting of two ferromagnetic metals, separated by a thin insulating layer, which serves as tunnel barrier, can be expressed as:

$$\frac{\Delta R}{R} = \frac{R_A - R_P}{R_P}, \tag{2.1}$$

where R_A and R_P represent the resistance of the two ferromagnetic layers with their magnetizations aligned antiparallel or parallel to each other. Julliere's model [61] for the TMR of this MTJ predicts that the TMR amplitude is linked to the effective spin polarization P_i of each ferromagnetic layer by the relation:

$$TMR = \frac{R_A - R_P}{R_P} = \frac{2P_{layer1}P_{layer2}}{1 - P_{layer1}P_{layer2}}, \tag{2.2}$$

Thus, high TMR values can be achieved by employing high spin polarized ferromagnetic electrodes on both sides of the MTJ.

Thin films and TMR devices have first been investigated systematically using the half-Heusler compounds PtMnSb and NiMnSb [62, 63]. The performance was rather disappointing. The spin polarization of NiMnSb integrated in a MTJ was measured to be 25% at 4.2 K corresponding to a TMR amplitude of 19.5% [12]. The TMR value at room temperature (RT) was 9% only. Later, TMR devices based on Co_2MnSi were shown to have much better performance. For tunnel junctions of textured Co_2MnSi with an Al oxide tunneling barrier a maximum TMR effect of 108% at 20 K and 33% at RT has been achieved, corresponding to 72% and 41% of spin polarization, respectively [64, 65, 66]. Recently a further improvement to 159% (89% spin polarization) at 2 K and 70% at RT was obtained by a japanese group using high-quality epitaxially grown Co_2MnSi electrodes [13, 14]. This is actually the highest TMR value observed for junctions using an amorphous Al oxide tunnel barrier. MTJs using a Co_2MnGe electrode were recently developed for the first time. The microfabricated epitaxial tunnel junctions using MgO as tunneling barrier showed strongly temperature dependent characteristics with TMR ratios of 14% at RT and 70% at 7 K [67]. For the newly predicted half-metal $Co_2Cr_{0.6}Fe_{0.4}Al$ as magnetic electrode a TMR ratio of 74% at 55 K was found, using a MgO tunneling barrier [68, 69, 67]. The maximum TMR values obtained for an Al oxide barrier are 52% at RT and 83% at 5 K [70]. The spin polarization was found to be 81% [71]. The obtained TMR ratio of 83% at 2 K in the MTJ with $B2$ ordered Co_2MnAl is large among the MTJs with an amorphous Al oxide tunnel barrier and suggest that

$B2$ ordered Co_2MnAl still exhibits a high spin polarization [14]. Smaller values for the TMR ratio were obtained in junctions using a Co_2FeSi electrode, i.e. 41% at RT and 60% at 5 K [70].

There are only very few experiments concerning the GMR effect in antiferromagnetically coupled metallic multilayers or in spin valves consisting of Heusler compounds. A room temperature current-in-plane (CIP) GMR effect has been measured in a $[Co_2MnGe/Rh_2CuSn]_{10}$ multilayer and was found to be very small, exhibiting a value of only 0.26% [72]. For spin valve structures employing the same material combination the situation is even worse [73]. This is in good agreement with GMR measurements on $[Co_2MnGe/V]_N$ multilayers [74]. The GMR values are far below the values obtained in transition metal multilayer system, which can be as large as 150% at room temperature [75].

To date, efficient electrical spin injection into semiconductors has been demonstrated only from magnetic semiconductors [76, 77] and conventional ferromagnetic metals [78, 79]. Fully spin polarized Heusler alloys are in principle ideal candidates for epitaxial contacts. Furthermore they are an alternative solution to the conductivity mismatch [54]. Spin injection experiments from the epitaxially grown half-Heusler NiMnSb into a spin LED have shown injected spin polarizations up to 2.2% at 80 K [80]. This is rather disappointing, since even a MnSb reference injector works better. More encouraging results are obtained using the alloy Co_2MnGe as spin injector. At 2 K the injected spin polarization is calculated to be 27% [81].

2.5. Heusler Half-metals: Disorder and Interfaces

Although the TMR results just discussed show that Heusler based magnetic elements are quite promising, the experimentally determined spin polarization is always definitely smaller than 100%. This experience leads to the suspicion that at least for a few monolayers at the interfaces the full spin polarization is lost.

Interfaces of the Heusler compounds with other materials are a very delicate problem for spintronic devices. For spin injection into semiconductors or a tunneling magnetoresistance the spin polarization of the first few monolayers at the interfaces is of utmost importance. A large spin polarization in the bulk of a Heusler compound does not guarantee that it is a good spintronic material, unless it keeps its spin polarization down to the interfaces. Hence there are various problems that have to be overcome in order to reach full spin polarization in real devices.

Site disorder within the sublattices of the Heusler compounds disturbs the perfect $L2_1$

point symmetry and may therefore destroy the half-metallicity. An essential question is, which type of disorder is most detrimental for the spin polarization. Therefore the effects of several types of defects in the Heusler alloys Co_2MnSi and Co_2MnGe have been studied by theoretical model calculations [10]. According to the experiment, the most frequent defects are: 1) Mn antisites where a Co atom is replaced by Mn, 2) Co antisites where a Mn atom is replaced by Co, and 3) Co-Mn swaps where a Mn-Co nearest neighbour pair shows exchanged position compared to the ideal bulk. The calculated formation energies for these defects together with the total magnetic moment of the 32-atoms unit cell used for calculation is shown in Tab. 2.2. Due to their low formation energy Co and Mn antisites are likely to be formed with a concentration as high as 8% [11, 82]. Co-Mn swaps have lower defect-densities. Since Co_2MnSi and Co_2MnGe show a very similar behaviour with respect to the defects, the results for Co_2MnSi are valid as well for Co_2MnGe.

Table 2.2.: Formation energy and total magnetic moments for the different defects in Co_2MnSi and Co_2MnGe, taken from Ref. [24].

	Co_2MnSi		Co_2MnGe	
	ΔE [eV]	M_{tot} [μ_B]	ΔE [eV]	M_{tot} [μ_B]
Co antisite	0.80	38.01	0.84	38.37
Mn antisite	0.33	38.00	0.33	38.00
Co-Mn swap	1.13	36.00	1.17	36.00

Mn antisite defects are most likely to occur in $Co_2Mn(Si,Ge)$. In this case the total density of states (DOS) shows a shift of 0.04 eV towards higher binding energies in the minority spin channel, resulting in a small increase of the spin gap. For this type of antisite disorder the half-metallicity is kept. However, the Mn magnetic moment is now coupled antiferromagnetically to the surrounding Mn spins, leading to a reduction of the saturation. Fig. 2.3 depicts the region close to the defect as compared to the ideal case, including the magnetic moments. Since the point defect-induced changes are efficiently screened by the conduction electrons, only the nearest neighbour spins are affected.

Although Co antisites are theoretically expected to occur in concentrations typically two orders a magnitude smaller than for the case of the Mn antisite, experimentally these two defects are found to have the same density. The Mn atom sitting on the Co position leads to a sharp peak in the electron DOS located just in proximity to the Fermi level (see Fig. 2.4) and therefore destroys the half-metallicity. The calculated spin polarization for the case presented in Fig. 2.4 is as low as 6%. The defect-induced states at the Fermi level are spatially localized, as shown in the inset of Fig. 2.4. The

Figure 2.3.: Magnetic moments for (a) the ideal system and (b) the Mn antisite system in Co_2MnSi (Co_2MnGe) around the defect. Values are taken from Ref. [24].

analysis of magnetic moments (Fig. 2.5) shows that in the case of an Co antisite defect the magnetic moments remain virtually unchanged and couple ferromagnetically to the surrounding Co spins.

Figure 2.4.: Total DOS for defective (bold line) and ideal (dashed line) Co_2MnSi with Co antisite. The inset shows the minority DOS at E_F projected on the different neighbours (denoted as roman numbers) as one moves away from the Co antisite defect [24].
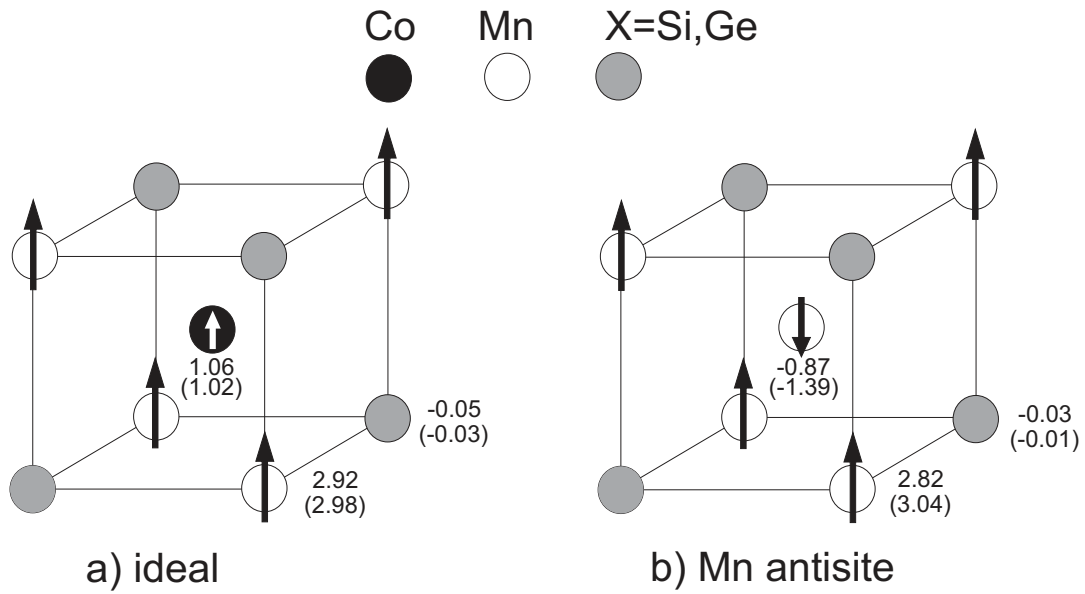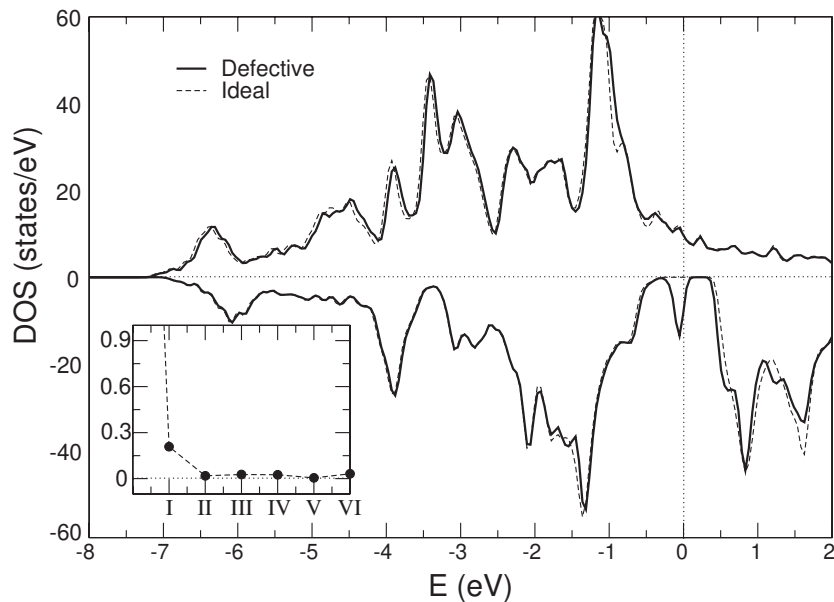
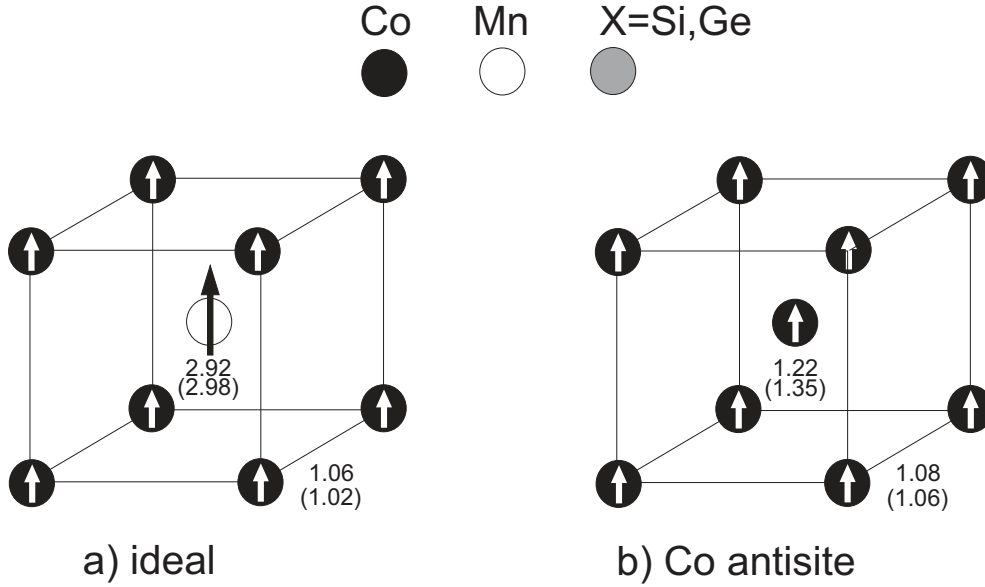Figure 2.5.: Magnetic moments for (a) the ideal system and (b) the Co antisite system in Co_2MnSi (Co_2MnGe) around the defect [24].

Co-Mn swaps can be viewed as the sum of two different Mn and Co atomic antisites. The calculated minority DOS is shifted to higher energies, along with a defect-induced peak located -0.2 eV below the Fermi level, the majority DOS remains essentially unaffected. Hence the half-metallic character is kept by the Co-Mn swaps. However, the total magnetic moment per unit cell is drastically reduced by about $4\mu_B$.

Comparable results were also discovered for the full Heusler compound $Co_2Cr_{1-x}Fe_xAl$ [83, 84]. While a partial exchange of Cr/Fe atoms with Al leaves the half-metallicity unaffected, an exchange of Co atoms with Cr, Fe or Al destroys the half-metallicity. The appearance of states in the minority spin gap accompanying site disorder was also found for the half-Heusler phases PtMnSb [85] and NiMnSb [86]. For the latter compound various kinds of disorder were considered and it was found that for 1% disorder the spin gap is reduced, but not destroyed, while 5% disorder results in a complete loss of the half-metallic properties [86].

This low degree of point disorder tolerable for the Heusler compounds presents a strong experimental challenge, since in thin films a larger amount of disorder than in the bulk material is expected due to lower preparation temperatures. The best choice to avoid disorder is to grow thin films epitaxially in the well ordered $L2_1$ structure, as has been realized for Co_2MnGe on GaAs [81, 82, 87] and MgO [67]. Another possibility to avoid point defects is to find Heusler alloys with particularly high energies for the defect formation.

A fundamental explanation for the loss of the full spin polarization in devices, which is favored by theoreticians, is a modification in the electronic energy band structure at the surfaces and interfaces. The half-metallicity in Heusler alloys is symmetry induced [88], and is thus very sensitive to any symmetry breaking at surfaces and interfaces. Ab-initio calculations revealed that even at stoichiometric surfaces the half-metallic character is generally lost [89]. For the half-Heusler alloys NiMnSb, CoMnSb and PtMnSb the spin polarization at the surfaces depends on the orientation and the termination, but is always less than 100% [89, 90, 91]. In the case of the full Heusler phases containing Mn the results are similar [89, 92], for instance at the MnGe terminated (110)-surface of Co_2MnGe the spin polarization is completely lost. However, there are Heusler alloys, which show high spin polarization even at the surface, as e.g. Co_2CrAl, with a CrAl terminated surface, which nearly maintains the half-metallicity.

For high-performance spintronic devices it is of special importance to restore the HMF behaviour at the interfaces with an isolator or semiconductor. Theoretical model calculations were first carried out for NiMnSb/semiconductor interfaces [90, 93], mainly showing the loss of half-metallicity at the interfaces, except in the case of NiMnSb/CdS. Further calculations revealed the presence of interface states at almost all Heusler/semiconductor contacts [94, 95]. Here, the half-metallicity is destroyed only for a few atomic layers close to the interface and completely restored far away from it.

Beside the fundamental problem of surface states the half-metallic materials suffer from a tendency of the surface to adopt a different composition than the bulk. As usual at alloy interfaces this surface segregation is driven by a difference in the free energy [96]. Segregation occurs in order to minimize the surface energy. Unfortunately, segregation too, has the tendency to destroy the half-metallic behaviour, as has been proven both experimentally and theoretically for the case of the half-Heusler compounds [91, 97].

The discussion above makes clear that for a device design not only the bulk, but necessarily the surface/interface properties have to be taken into account. A controlled surface and interface engineering is needed. However, the use of Heusler alloys in devices is still promising, if material combinations can be found, which preserve the half-metallicity even at the interface. Theoretical calculations have already demonstrated that this is possible, for instance in the case of the NiMnSb(111)/CdS(111) surface [90]. To sum up the introductory part, there are challenges, but the gate to Heusler based spintronic devices has been opened.

2. Heusler Alloys

3. Spin Glasses

Since in the $[Co_2MnGe/V]$ multilayers at low temperature a complicated spin glass type of phase transition is observed, as will be discussed in Chap. 7, the basic concepts of spin glass order will be shortly reviewed here.

Spin glasses are magnetic systems, in which the interactions between the magnetic moments compete with each other due to some frozen-in structural disorder. They can be defined as random mixed-interacting systems characterized by a random, yet cooperative, freezing of spins at a well defined (freezing) temperature T_f, below which a highly irreversible metastable frozen state occurs without the usual long-range ferro- or antiferromagnetic order [98]. Although the nature of this kind of order has been studied extensively and much efforts have been put into appropriate theoretical descriptions, the character of the freezing transition is still not solved completely. It is clear that spin glass freezing involves strong cooperative effects, but while there are hints for a true magnetic phase transition, no convincing evidence could be found.

The two important ingredients of spin glasses are randomness in either position of the spins or sign of their exchange interactions and frustration, i.e. a given spin cannot satisfy all the magnetic interactions in the system.

An archetypal and well studied example of a spin glass is the alloy $Cu_{1-x}Mn_x$ [99], where the concentration of Mn is a few atomic percent. The Mn ions are therefore present only in dilute quantities and their magnetic moments interact with each other via a RKKY interaction mediated by the conduction electrons in Cu. Site-randomness in CuMn leads to a distribution of distances between spins. Since the RKKY interaction oscillates in sign, i.e. can be either ferro- or antiferromagnetic as a function of the distance between the spins, the alloy exhibits intrinsic frustration and does not possess a magnetic ground state. At high temperatures the Mn moments fluctuate thermally, but with decreasing temperature magnetic short range order will built up. At T_f the moments freeze in a highly degenerate spin glass state.

Already in the 1930s experimental investigations on CuMn indicated some strange properties and around late 1960s there were some unusual effects observed on a series of magnetic alloys. The name 'spin glass' came up in 1970. At that time the sharp

3. Spin Glasses

cusps in the low-field susceptibility of spin glasses were discovered and correlated with a magnetic-ordering temperature [100]. Distinctions were made between spin glasses and so-called 'mictomagnets' (cluster glass), where the former category was reserved for dilute magnetic metallic alloys and cluster glass referred to alloys with higher concentration of magnetic atoms, when the magnetic behavior is dominated by the presence of large magnetic clusters (of order 20-20000 μ_B). It is now widely accepted that there is no fundamental distinction between these two classes, and hence all these systems are considered as spin glasses [101]. Returning to history, in the mid 1970s finally the theorists became interested and used some new concepts and models to explain the experimental facts. The spin glasses became very important and gave new impulses to many other fields, such as neural networks, biomolecules and the vortex-glass state in high-T_c superconductors [98, 102]. While the basic phenomena have been understood qualitatively, a full description by the theory was still lacking. Today the spin glass has become a fundamental and general form of magnetism and is still an active field of research [103, 104, 105, 106, 107, 108, 109, 110].

This chapter shortly introduces the physics of spin glasses via an experimental approach following the review of Mydosh [111]. An overview about the theoretical concepts can be found in Ref. [101]. Firstly, randomness as an important prerequisite of a spin glass will be discussed (Sec. 3.1). Equally essential is the presence of competing interactions, which lead to frustration of the spins. Hence the spin glass system exhibits a highly degenerate ground state and shows a cooperative freezing process (Sec. 3.2). Many spin glasses, including the [Co$_2$MnGe/V] system, exhibit superparamagnetic behaviour above T_f, thus superparamagnetism will be introduced in Sec. 3.3.

3.1. Randomness and Magnetic Interactions

In the constitution of a spin glass, there must be disorder, either site or bond randomness. Examples of metallic site-random spin glasses are provided by the archetypal spin glasses $Au_{1-x}Fe_x$ and $Cu_{1-x}Mn_x$ with $x \ll 1$. Here the substitution of small amounts of the magnetic ions into the non-magnetic matrix occurs completely randomly with no short-range ordering. This directly leads to a random distribution of distances between the magnetic ions. Insulating and conducting chemical compounds can also made random by diluting the sublattices, examples are the semiconductor $Eu_xSr_{1-x}S$ [112] and the metal $La_{1-x}Gd_xAl_2$. Random-site occupancy can be realized by taking an intermetallic compound and making it amorphous. This is achieved by a very rapid cooling from the melt, so that the crystalline lattice is destroyed. Once the randomness is established, it

remains forever fixed and is therefore named quenched-disorder.

Another possibility to produce a spin glass is bond-randomness, in which the nearest neighbour exchange interactions vary between ferromagnetic coupling J_+ and antiferromagnetic coupling J_-. The existence of such a random-bond system was experimentally discovered e.g. in $Rb_2Cu_{1-x}Cr_xF_4$.

As mentioned above, competing interactions are the second ingredient of a spin glass order, thus the typical interactions important for a spin glass are shortly introduced.

In metals the exchange interaction between distant magnetic ions can be mediated by the conduction electrons of a non-magnetic metallic matrix. A localized magnetic moment spin-polarizes the conduction electrons and this polarization couples to a neighbouring localized moment at a distance r. This indirect interaction is known as the famous Rudermann, Kittel, Kasuya, Yosida (RKKY) interaction [113]. Its Hamiltonian is $\mathcal{H} = J(r)\mathbf{S}_i\mathbf{S}_j$, where $S_{i,j}$ are the local spins and the coupling strength J describes a damped oscillation. At large distances one yields

$$J(r) = \frac{J_0 \cos(2k_F r)}{(2k_F r)^3}, \tag{3.1}$$

with the Fermi momentum k_F and the distance r between the magnetic moments. The $(1/r)^3$ fall-off is sufficiently long-ranged so that it can effectively reach many nearest neighbour sites. Combining the oscillating RKKY polarization with the site disorder discussed above, a random distribution of coupling strengths and directions can be generated.

In insulating materials the exchange mechanism operating is known as superexchange. It can be defined as an indirect exchange interaction between next-nearest neighbouring magnetic ions, which is mediated by a non-magnetic ligand placed in between (see Fig. 3.1). The ligand transfers an electron (usually in a p state) to the magnetic atom. A sort of covalent mixing of the p and d wave functions occurs. Due to the Pauli exclusion principle the two p electrons of the ligand must be opposite in direction and thus cause antiparallel pairing with the d electrons on the magnetic atoms.

An interaction always present in magnetic materials is the dipolar coupling. The corresponding Hamiltonian takes the form:

$$\mathcal{H}_{ij} = \frac{1}{r_{ij}^3}[\mu_i \cdot \mu_j - 3(\mu_i \cdot \hat{r}_{ij})(\mu_j \cdot \hat{r}_{ij})], \tag{3.2}$$

with the spin magnetic moments $\mu_{i,j}$ at a distance r_{ij}. In addition to the $(1/r_{ij})^3$ distance dependence there is also a built-in anisotropy which can favour ferro- or antiferromag-
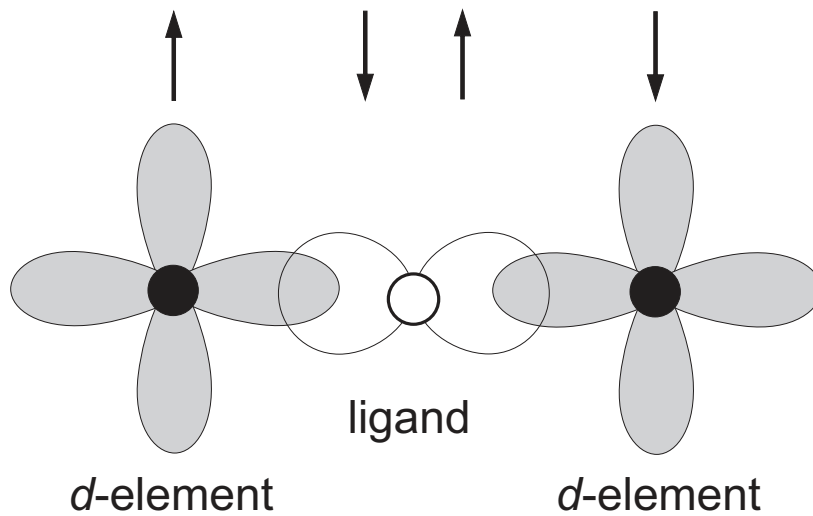
Figure 3.1.: Superexchange between two magnetic d ions and a p state (e.g. in MnO). The arrows show the spins of the electrons and how they are distributed over the atoms.

netic alignment. If the spins are oriented along $\mathbf{r}_{ij}$ they will couple ferromagnetically, if the spins are oriented perpendicular to $\mathbf{r}_{ij}$ then they couple antiferromagnetically. Thus the dipolar interaction in a two- or three-dimensional magnet introduces to some degree a competing interaction.

Competing interactions may lead to frustration of the spin orientation. As a simple example a square lattice of four Ising spins with four $\pm J$ bonds is depicted in Fig. 3.2. For the left-hand configuration all the exchange interactions can easily be satisfied. The system exhibits a two-fold-degenerate ordered state and is unfrustrated. The degeneracy is caused by the arbitrariness of the initial choice of the first spin. For the right-hand configuration there is frustration. Whichever choice is made, all the exchange interactions cannot be satisfied simultaneously. As a result the system possesses an 8-fold degenerate, metastable ground state. It should be noted that frustration is a direct consequence of the disorder and mixed interactions. While it is a necessary condition for a spin glass, it is not a sufficient one.

3.2. The Freezing Process

A naive picture of the evolution of a spin glass, when the temperature is reduced from far above the freezing temperature T_f to below, shall be presented here.

At high temperatures the behaviour of a spin glass system is dominated by thermal fluctuations, i.e. there will simply be a collection of paramagnetic spins, which are
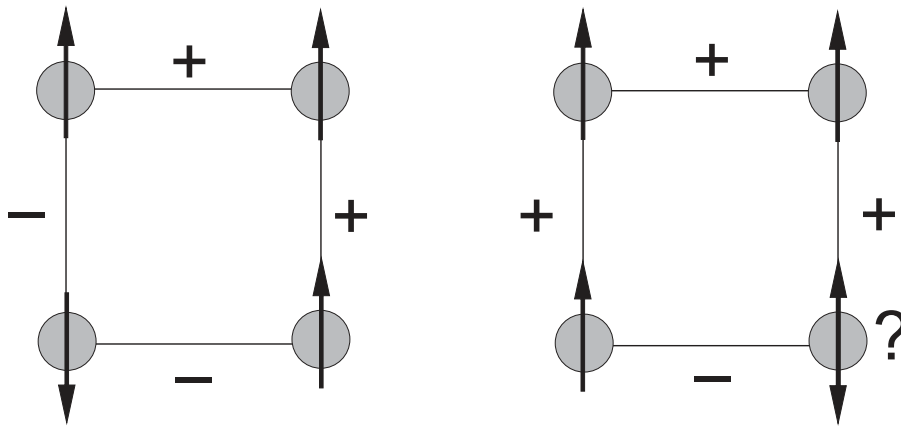
Figure 3.2.: Square lattice with mixed interactions. The left plaquette shows the unfrustrated and the right one the frustrated case. '+' denotes a ferromagnetic, '-' an antiferromagnetic interaction.

rotating independently. As the spin glass is cooled, the rotating spins slow down and build up magnetic short-range order, leading to small, randomly oriented clusters. The remaining spins, which are not coupled to clusters, are independent of each other, but help to transmit the interactions between the clusters, allowing for changes in the cluster size. As the temperature reaches T_f, the thermal disorder is gradually removed and the correlations between the clusters become more long-ranged. At T_f the system freezes in one of its multi-degenerate ground states. Since the free energy of the system exhibits many valleys separated by energy barriers (see Fig. 3.3), it may become trapped in one of the many metastable configurations.
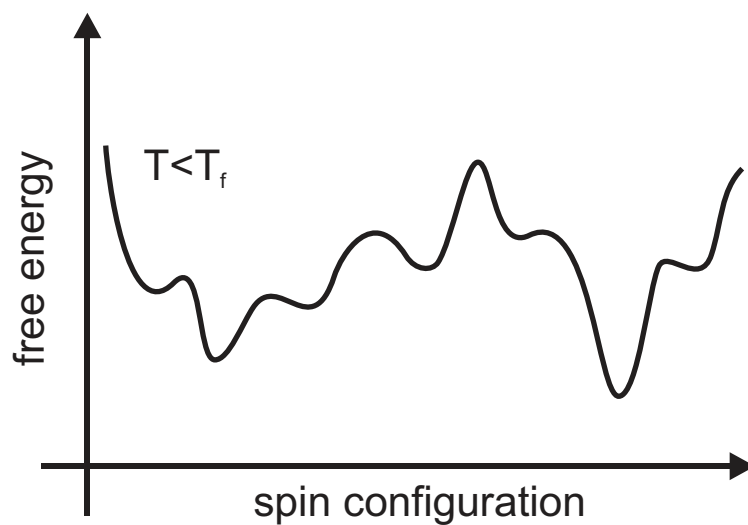

Figure 3.3.: Schematic picture of the free energy of a spin glass in a magnetic field in dependence of the spin configuration of its lattice atoms below T_f.

The exact nature of the spin glass freezing process is still not very clear. It is definitively different from a gradual blocking of spin clusters, the freezing process is a cooperative transition. On the other hand it is not clear up to now, if the spin glass exhibits a true phase transition or a glass type slowing down of the spin dynamics. The spin glass phase usually does not possess long-range magnetic order, there are no magnetic Bragg peaks found in scattering experiments due to a lack of translational invariance [114, 115].

Phenomenologically the spin ordering can be described via a spin-spin correlation function $\langle S_i S_j \rangle_t$, here for the simplified case of Ising spins. Since the sign of this correlations will be random $\langle S_i S_j \rangle_t = 0$ holds, but

$$\langle S_i S_j \rangle_t^2 \approx exp\left(\frac{-|\mathbf{R}_i - \mathbf{R}_j|}{\xi_{SG}}\right) \tag{3.3}$$

where $|\mathbf{R}_i - \mathbf{R}_j|$ is the distance between the spins and ξ_{SG} is the spin glass correlation length. One observes that ξ_{SG} grows as $T \rightarrow T_f$, showing that important collective effects are taking place [101].

3.3. Superparamagnetism

Superparamagnetism is a magnetic phenomenon observed in many spin glasses at higher temperatures.
A model superparamagnet is an ensemble of small, non-interacting, single-domain ferromagnetic particles, whose magnetization points in the direction of an easy axis. This can be due to magnetocrystalline or shape anisotropy. The energy of the particles can thus be written as $E = KV \sin^2 \theta - \mu H \cos \theta$, where K is the anisotropy constant, V is the volume of a particle with magnetic moment μ, and θ denotes the angle between the magnetization and the easy axis. The energy is minimized when $\theta = 0$ or π. The energy barrier $E_a = KV$ has to be overcome to flip the magnetization direction from $\theta = 0$ to π or the other way round. This can be managed with either field energy ($\mathbf{M} \cdot \mathbf{H}$) or thermal energy ($k_B T$). For small particles the activation energy KV is small compared to $k_B T$, and the magnetization can easily be flipped by thermal fluctuations. At high temperatures ($k_b T \gg KV$) the system will therefore show paramagnetic behaviour with fluctuating clusters, each owing a large magnetic moment (up to $10^5 \mu_B$). Therefore, the system is called superparamagnet. The magnetization of this superparamagnet at high

temperatures scales like [116]

$$M(H,T) = N_c\mu_c\mathcal{L}(\frac{\mu_c H}{k_b T}), \tag{3.4}$$

with the number of magnetic clusters N_c, the cluster magnetic moment μ_c and the Langevin function $\mathcal{L}(x)$. The relaxation time τ of the moment on a particle is given by thermal activation

$$\tau = \tau_0 exp\left(\frac{KV}{k_B T}\right), \tag{3.5}$$

where τ_0 is typically 10^{-9} s. Thus the fluctuations slow down with decreasing temperature. When the relaxation time τ is much longer than the measuring time t ($\tau > \alpha t$ with $\alpha = 100$), the system will appear magnetically ordered. This defines a blocking temperature T_B, given by $T_B = KV/k_B ln(\alpha t/\tau_0)$. The blocking temperature T_B is of order $KV/25k_B$, since t can be changed by a few orders of magnitude with only a relatively small change in T_B. The blocking temperature will not be the same for all particles, if they exhibit a distribution in V or K.

There is an important difference between the superparamagnetic blocking at T_B and a spin glass freezing process at T_f. The non-interacting particles are blocked gradually as given by their volume and anisotropy energy. In a spin glass freezing or cluster glass freezing process the interaction between the clusters leads to a phase transition like collective phenomenon at T_f.

3.4. Spin Glass Phenomena

In this section typical magnetization and susceptibility measurements on spin glasses will be introduced. A survey of the various other measuring techniques is given in Ref. [101].

Far above the freezing temperature the spin glass behaviour resembles that of a (super)paramagnet with a collection of freely rotating magnetic moments. For a paramagnet, the susceptibility χ is just $\chi = M/H$, since usually it is measured in the low-field limit of the magnetization's Brillouin function. Fig. 3.4 shows a systematic susceptibility study on many different concentrations of the spin glass alloy CuMn. The results are plotted as inverse susceptibility versus temperature. The susceptibility at high temperatures follows a Curie-Weiss law

$$\chi = \frac{C}{T - \Theta}, \tag{3.6}$$

C being the Curie constant and Θ the Curie paramagnetic temperature. The rapid increase of Θ with the concentration of Mn reflects the increasing ferromagnetic interac-
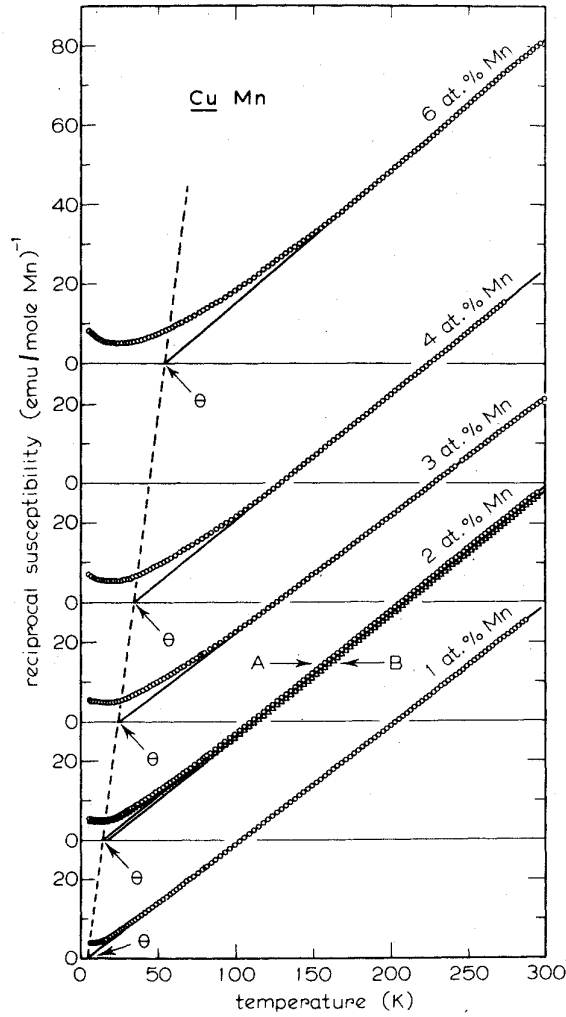
Figure 3.4.: Reciprocal susceptibility of $Cu_{1-x}Mn_x$ with different concentrations as a function of temperature. Figure taken from Ref. [117].

tion. Both in metallic and insulating spin glasses [99, 118] even at temperatures as high as about $5T_f$ the first deviations from the Curie-Weiss law have been observed. Thus on a local scale strong magnetic correlations develop far above the freezing temperature.

A fairly universal characteristic phenomenon in spin glasses was found in the early 1970s by Cannella and Mydosh [100], who discovered sharp cusps in the frequency-dependent susceptibility of AuFe and CuMn in low fields. Both canonical spin glasses were studied many years before, but only in high fields. While the random interactions in a spin glass cause a freezing of the spins in random directions, a magnetic field aligns them parallel to the field. Therefore, a strong magnetic field can destroy the spin glass state.

Fig. 3.5 shows the frequency-dependent (ac-)susceptibility χ_{ac} for CuMn (1 at%) as
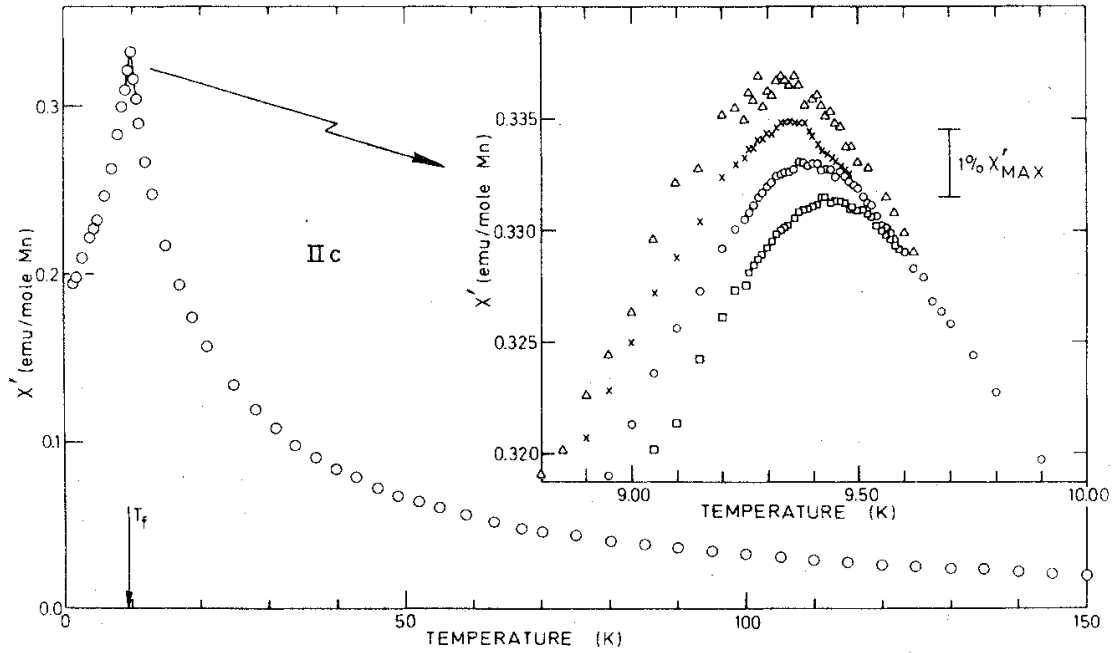
Figure 3.5.: Zero-field susceptibility χ' as a function of temperature for the alloy CuMn; from Ref. [119].

a function of temperature. The cusp clearly defines the freezing temperature T_f. However, on the fine scale of the inset there is a slight rounding of the cusp into a peak, contradictory to the hypothesis of a phase transition. With decreasing frequency of the ac measurements the peak is shifted downwards in temperature. For the frequency variation of 2.5 decades in Fig. 3.5, T_f is reduced by about 1%. This frequency shift is not expected or found in usual long-range ordered anti- or ferromagnetic materials up to the mega or giga Hertz range. This exemplifies that spin glasses exhibit a unique transition with unconventional dynamics.

Fig. 3.6 illustrates the two measurement procedures to cool a spin glass in a dc magnetization experiment. The first is to cool the sample in zero field to $T \ll T_f$ $(a \rightarrow b)$ and at this temperature apply the field. Instantaneously this will give rise to a jump in the magnetization $(b \rightarrow c)$ to a value comparable with that found from χ_{ac}. The temperature is then increased and the zero-field cooled (ZFC) warming curve $(c \rightarrow d \rightarrow e)$ is recorded. Secondly, the sample can be cooled with a measuring field applied, while recording the field-cooled (FC) magnetization $(e \rightarrow d \rightarrow f)$. At T_f the FC susceptibility becomes independent of the procedures and nearly independent of time. Furthermore, the process of field cooling followed by field warming is reversible; the temperature can be cycled back and forth, while the FC susceptibility traces the same path. On the other hand, the entire ZFC curve $(c \rightarrow d)$ exhibits a slow time evolution up to T_f. Thus
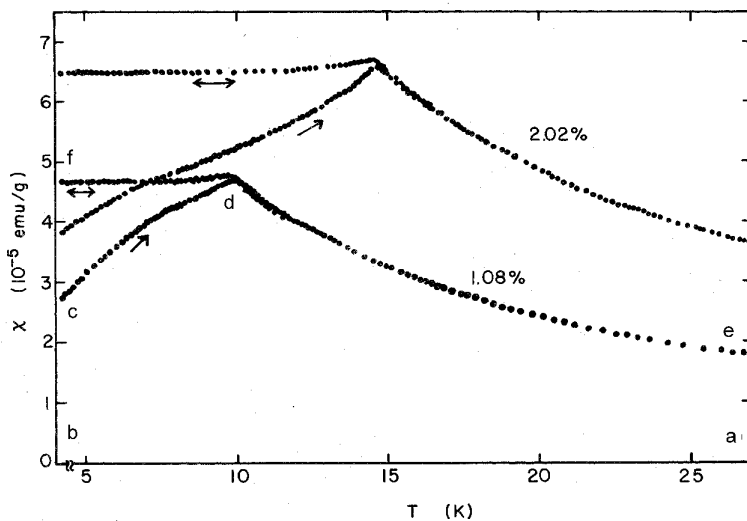
Figure 3.6.: Field cooled (e→f) and zero-field cooled (e→c) magnetizations for CuMn as a function of temperature; from Ref. [120].

the dc field, if applied below T_f, creates a metastable, irreversible state and the freezing temperature is defined by the onset of the irreversibilities. This can qualitatively be understood in the picture of the spin glass hypersurface in Fig. 3.3. The coarse-grained free energy is strongly temperature dependent near T_f. Above T_f all valleys are very shallow, but some of them become very deep as the temperature is lowered. Thus on cooling the system may be trapped in a side-minimum and many rearrangements of clusters of spins are necessary until the system can relax.

For $T < T_f$ the spin glass is in its frozen state without having a true long-range magnetic order. The initial magnetization $M_{zfc}(H)$ after zero-field cooling shows a characteristic S-shaped form, not observed above T_f [121]. However, $M_{zfc}(H)$ does not yield information on the thermal equilibrium behaviour of spin glasses, since it shows a time dependence [122]. On the other hand, the magnetization $M_{fc}(H)$ found in field cooling shows only weak time effects and is therefore suggested to be the true equilibrium magnetization of a spin glass [123].

Spin glasses exhibit pronounced irreversibility effects, when the field is changed at a fixed temperature. The hysteresis phenomena can resemble those in ferromagnets. However, there exists a wide variation in the shape of the hysteresis loops, which also depend on the magnetic history of the sample. For instance in dilute AuFe the loops are rather narrow and flat and antisymmetric around the origin (see Fig. 3.7(a)). In comparison CuMn with low concentration of Mn has been found to show a squared hysteresis loop with sharp steps (see Fig. 3.7(b)). Almost the entire remanence is reversed in a very short time and at a very sharp value of the field, indicating a macroscopically

coherent reversal of the magnetization. This phenomenon points towards a cooperative behavior among a large number of frozen spins. This is confirmed by theoretical model calculations revealing that for such a magnetization reversal ferromagnetic short-range order is predominant [124].
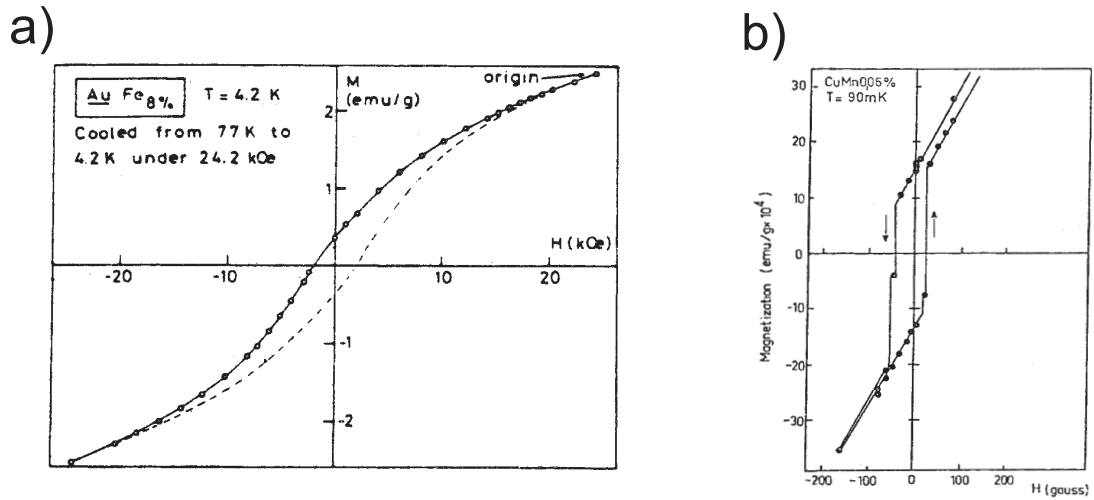

Figure 3.7.: Hysteresis behaviour of (a) AuFe and (b) CuMn at low temperatures given in the figure; taken from Ref. [125, 126].

Part II.

Scattering Methods

4. Neutron Scattering

The neutron was discovered 1932 by Chadwick [127]. It attained its name by the observation that it does not possess an electric charge and hence is neutral. Today it is known that the neutron is composed of one up and two down quarks with charge 2/3 and −1/3, respectively.

1936 Hahn, Meitner and Strassmann observed the first man-made nuclear fission and already in the same year also the first neutron scattering experiment was performed using neutrons from a radium beryllium source. In 1942 Fermi built the first nuclear reactor in Chicago and 1945 the first neutron diffractometer became operational. After crucial developments in neutron sources and scattering methods, in the 60's the first high flux reactor specially designed for beam hole experiments became critical in Brookhaven. 1972 the reactor at the Institute Laue Langevin in Grenoble went into operation, which is still the most powerful neutron source worldwide [128].

The reason for the success of neutron scattering in the scientific research is the fact that neutrons provide a series of properties making them a unique probe for the investigation of structure and dynamics of condensed matter and biomolecules:

- The mass of the neutrons leads to a de Broglie wavelength of thermal neutrons ($E \cong 25$ meV) being of the order of interatomic distances in solids and liquids and thus can yield information on the structure of the scattering system.

- The energy of thermal neutrons is of the same order as that of many excitations in condensed matter. So the measurement of the neutron energies in an inelastic scattering experiment provides information on the interatomic forces.

- Neutrons exhibit a magnetic moment and therefore interact with the unpaired electrons in magnetic atoms. This makes neutron scattering unique for the investigation of magnetic structures.

- Neutrons interact differently with different isotopes of the same atomic species, which can give rise to a strong contrast in neutron scattering experiments, while there is only little contrast in x-ray scattering.

- Since the neutron is an uncharged particle it is scattered by nuclear forces and can penetrate deeply into the target. In addition, the interaction is weak and can be treated within the first Born approximation.

This chapter is organized as follows: After providing a survey above fundamental properties of the neutrons, a short review of the scattering theory is given. Subsequently the theory and the experimental realization of neutron reflectivity and off-specular scattering are presented.

Fundamental Properties of the Neutron

Neutrons as nuclear constituents are stable, whereas free neutrons are radioactive particles with a mass of $m_n = 1.675 \cdot 10^{-27}$ kg [129]. As an effect of the weak interaction the neutron decays after a half-life of $\tau = 890$ s $\pm$ 60 s into a proton, an electron and an antineutrino, according to:

$$n \rightarrow p^+ + e^- + \tilde{\nu} \ (+0.77 \text{ MeV}). \tag{4.1}$$
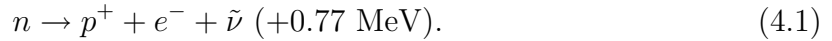
The energy of the neutron is given by its kinetic energy $E = \frac{1}{2}m_n v^2$. The velocity spectrum of neutrons emerging from a nuclear reactor and being thermalized by a moderator is close to Maxwellian with the temperature T of the moderator. This yields the energy for the most probable velocity $v_{max} = (\frac{2k_B T}{m_n})^{\frac{1}{2}}$ [130]:

$$E = k_B T. \tag{4.2}$$

The de Broglie wavelength of a neutron with velocity v is $\lambda = \frac{h}{m_n v}$ where h is the Planck constant. The wavevector $\mathbf{k}$ is defined to have the magnitude $k = \frac{2\pi}{\lambda}$, its direction being that of $\mathbf{v}$. The momentum of the neutron is $\mathbf{p} = \hbar\mathbf{k}$, yielding

$$E = k_B T = \frac{1}{2}m_n v^2 = \frac{h^2}{2m_n \lambda^2} = \frac{\hbar^2 k^2}{2m_n}. \tag{4.3}$$

Thermal neutrons with a temperature of $T = 290$ K possess an energy of approx. 25 meV. Hence they have a wavelength of 0.18 nm and a velocity of 2200 m/s.

The neutron carries a spin of $\frac{1}{2}$ which is accompanied by a magnetic dipolar moment

$$\mu_n = -1.913\mu_N \sigma, \tag{4.4}$$

where μ_N is the nuclear magneton and σ the Pauli spin operator for a particle with spin

quantum number 1/2. The negative value of the magnetic moment indicates that it is directed antiparallel to the spin direction.

The magnetic moment of the neutron interacts with both the electrons and the magnetic moment of the nuclei. Since the latter interaction is small, it will be neglected within the framework of this thesis.

4.1. Scattering Theory

This chapter provides the theoretical background for nuclear scattering processes on a quantum mechanical basis. It should elucidate the fundamental aspects only; detailed descriptions of the scattering problem can be found in textbooks on quantum mechanics [131, 132] or neutron scattering [133, 134].

For an idealized neutron scattering experiment a beam is assumed with a current density $\mathbf{j}_0(\mathbf{r})$ incident on the target. The scattering is assumed to be elastic, i.e. the energy of the scattered neutrons is equal to that of the incident particles. The scattering process is considered to be a sum of incoherent single processes and thus can be reduced to a two-body-problem. The scattering center shall exhibit an interaction range centered at the coordinate origin. Thus in the far field the incident neutron can be described as a plane wave $\Psi_0(\mathbf{r}) = e^{i\mathbf{kr}}$ with the wave vector $\mathbf{k}$ (see Fig. 4.1). The scattering object located at $r = 0$ interacts with the neutron at $\mathbf{r}$ via the potential $V(r)$ and can be considered as a perturbation of the incident beam wave function Ψ_0 leading to the creation of a scattered spherical wave $\Psi_s(\mathbf{r})$. As the interaction potential $V(r)$ is only short ranged the motion should be free of forces at $\mathbf{r} \rightarrow \infty$. Thus for the scattered wave it follows:

$$\Psi_s(\mathbf{r}) \stackrel{r \to \infty}{\rightarrow} f(\mathbf{Q}) \frac{e^{i\mathbf{k'r}}}{r}, \tag{4.5}$$

where $\mathbf{k'}$ denotes the wavevector of the scattered wave and Q is the so-called scattering vector, defined by

$$\mathbf{Q} = \mathbf{k} - \mathbf{k'}. \tag{4.6}$$

As the scattering events are elastic, i.e. $|\mathbf{k}| = |\mathbf{k'}|$, one gets

$$|\mathbf{Q}| = 2|\mathbf{k}| \sin(\Theta). \tag{4.7}$$

f($\mathbf{Q}$) is called scattering amplitude and is the central parameter in scattering processes as it contains all the information about the scattering potential.

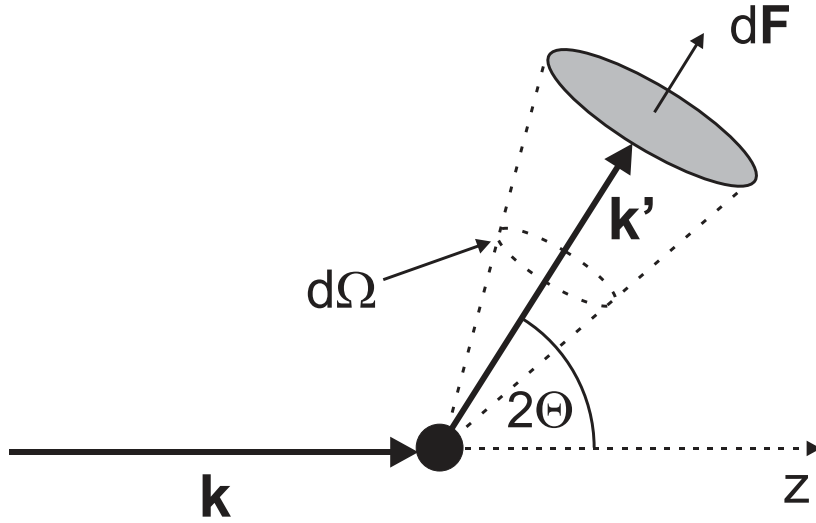The connection to the experiment is given by the differential scattering cross section,

Figure 4.1.: Scattering geometry for an incident plane wave scattered at a target.

$(d\sigma/d\Omega)$, which is defined as the ratio of flux of neutrons, scattered into the solid angle $d\Omega$, to the incoming flux (see Fig. 4.1),

$$\frac{d\sigma}{d\Omega} = \frac{\mathbf{j}_s \cdot d\mathbf{F}}{|\mathbf{j}_0| d\Omega}, \qquad (4.8)$$

where $dF = r^2 d\Omega$ denotes the area covered by the detector and j_s is the flux of the scattered wave.

Quantum mechanically the flux is given by

$$\mathbf{j} = \rho_a \frac{\hbar}{2mi} (\Psi^* \nabla \Psi - \Psi \nabla \Psi^*), \qquad (4.9)$$

where ρ_a is the particle density of the incident beam. For the incident plane wave Ψ_0 Eq. (4.9) leads to $\mathbf{j}_0 = \rho_a \frac{\hbar \mathbf{k}}{m}$. The flux of the scattered spherical wave for large r is given as $\mathbf{j}_s = \rho_a \frac{\hbar k}{m} \frac{|f(Q)|^2}{r^2} \mathbf{e}_r$. Inserting the incoming and scattered flux into Eq. (4.8) finally the cross section is obtained:

$$\frac{d\sigma}{d\Omega} = |f(\mathbf{Q})|^2. \qquad (4.10)$$

The scattering cross-section is completely determined by the scattering amplitude. $d\sigma$ has the dimension of an area and is given in barn (1 barn$=10^{-24} cm^2$). It should be emphasized that scattering gives information on the absolute value of the scattering amplitude only, information on the phases are lost. This is the so-called phase-problem.

The total cross section is found by integrating the differential cross-section over all

possible scattering angles:

$$\sigma = \int d\Omega \frac{d\sigma}{d\Omega}. \tag{4.11}$$

The cross-sections and therefore $|f(\mathbf{Q})|^2$ can be determined experimentally. The next task is now to create a connection between $|f(\mathbf{Q})|^2$ and the interaction potential $V(\mathbf{r})$.

4.1.1. Scattering and Born Approximation

For the calculation of the scattering amplitude $f(\mathbf{Q})$ the time-independent Schrödinger equation

$$(\Delta_r + k^2)\Psi(r) = v(\mathbf{r})\Psi(\mathbf{r}) \tag{4.12}$$

has to be solved, with the abbreviation

$$k^2 = \frac{2mE}{\hbar^2}; v(\mathbf{r}) = \frac{2m}{\hbar^2}V(\mathbf{r}). \tag{4.13}$$

Here k denotes the wave vector for propagation in empty space.

Now the linear partial differential equation will be transformed into an integral equation. This has the advantage that for such an integral equation a solution can be found by iteration.

$\Psi_0(\mathbf{r})$ is the solution of the homogenous differential equation:

$$(\Delta_r + k^2)\Psi_0(\mathbf{r}) = 0. \tag{4.14}$$

Then, however, every solution of the integral equation

$$\Psi(\mathbf{r}) = \Psi_0(\mathbf{r}) + \int d^3r' G(\mathbf{r} - \mathbf{r}')v(\mathbf{r}')\Psi(\mathbf{r}') \tag{4.15}$$

is simultaneously a solution of the Schrödinger equation (4.12), if the Greens-function $G(\mathbf{r} - \mathbf{r}')$ fulfills the equation

$$(\Delta_r + k^2)G(\mathbf{r} - \mathbf{r}') = \delta(\mathbf{r} - \mathbf{r}'). \tag{4.16}$$

$\Psi_0(\mathbf{r})$ and $G(\mathbf{r} - \mathbf{r}')$ have to be determined with respect to the boundary conditions. $\Psi_0(\mathbf{r})$ is a plane wave in empty space

$$\Psi_0(\mathbf{r}) = e^{i\mathbf{k}\mathbf{r}}. \tag{4.17}$$

In the far field limit the scattered wave behaves like an outgoing spherical wave. One

4. Neutron Scattering

can verify that

$$G(r - r') = -\frac{e^{ik|\mathbf{r}-\mathbf{r}'|}}{4\pi|\mathbf{r} - \mathbf{r}'|}, \quad (4.18)$$

fulfills this condition and is a solution of Eq. (4.16). The integral equation equivalent to the Schrödinger equation with boundary conditions can now be written as:

$$\Psi(\mathbf{r}) = e^{i\mathbf{k}\mathbf{r}} - \frac{m}{2\pi\hbar^2} \int d^3r' V(\mathbf{r}')\frac{e^{ik|\mathbf{r}-\mathbf{r}'|}}{|\mathbf{r} - \mathbf{r}'|}\Psi(\mathbf{r}'). \quad (4.19)$$

The interpretation is as follows: the incident wave $\Psi_0(\mathbf{r})$ is superimposed by spherical waves emitted from scattering at positions $\mathbf{r}'$. The intensity of these spherical waves is proportional to the interaction potential $V(\mathbf{r}')$ and the amplitude of the wave field at the position $\mathbf{r}'$. To obtain the total scattering amplitude, one has to integrate over the entire sample volume.

The equation (4.19) has still to be solved, which can be done now by iteration. For simplification the operator $\mathbf{G}$ is introduced, giving the integral over the Greens function in Eq. (4.19), which then can be expressed by:

$$\Psi = \Psi_0 + \mathbf{G}V\Psi. \quad (4.20)$$

In the first order Born approximation, which is usually called kinematical scattering theory, the wave function Ψ on the right-hand side is substituted by Ψ_0:

$$\Psi^{(1)} = \Psi_0 + \mathbf{G}V\Psi_0. \quad (4.21)$$

This approximation is only valid, if the scattering is weak, since it neglects multiple scattering processes. For neutron scattering this approximation often holds well. To analyze neutron reflectivity data however, one has to go beyond the kinematical theory (see Chap.4.3).

In the asymptotical limit the interaction range R_0 of the potential $V(\mathbf{r})$ is much smaller than the distance scattering center - detector, so that $r \gg R_0$ and $r' \ll r$ (see Fig. 4.2). Hence the scattered wave is given by:

$$\Psi^{(1)}(\mathbf{R}) = e^{i\mathbf{k}\mathbf{R}} - \frac{e^{ikR}}{R}\frac{m}{2\pi\hbar^2} \int d^3r' V(\mathbf{r}')e^{-i\mathbf{Q}\mathbf{r}'}, \quad (4.22)$$

and the scattering amplitude can be written as:

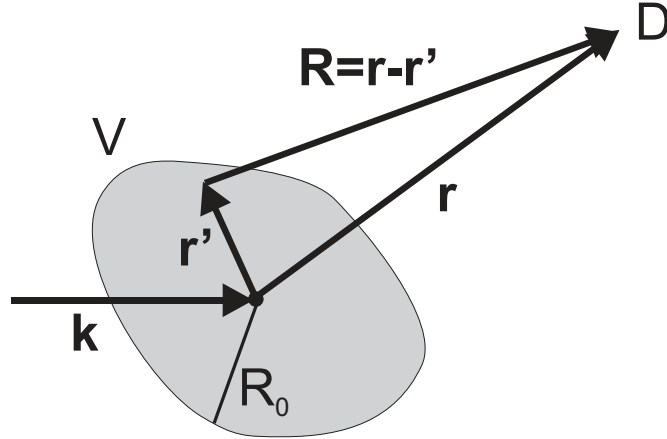$$f^{(1)}(\mathbf{Q}) = -\frac{m}{2\pi\hbar^2} \int d^3r' V(\mathbf{r}')e^{-i\mathbf{Q}\mathbf{r}'}. \quad (4.23)$$

Figure 4.2.: Scattering geometry for the calculation of the far field limit at the detector D. The interaction range of the local potential V is R_0. The wavevector of the incoming wave is **k**.

In first order approximation this shows that the scattering amplitude is proportional to the Fourier transform $V(Q)$ of the scattering potential.

If the special case of a spherically symmetric potential $(V(\mathbf{r}') = V(r'))$ is assumed, the scattering amplitude becomes a function of $|\mathbf{Q}|$. In the case of thermal neutron scattering on the nuclear potential, the interaction range is so short compared to the wavelength that it can be considered as δ-function. This potential is called Fermi's pseudo potential:

$$V(\mathbf{r}) = \frac{2\pi\hbar^2}{m} b\delta(\mathbf{r}), \tag{4.24}$$

where b denotes the nuclear scattering length, which is a phenomenological parameter. Using Eq. (4.23) one obtains the scattering amplitude for Fermi's pseudo potential

$$f^{(1)}(Q) = -b. \tag{4.25}$$

Apparently $f^{(1)}$ is isotropic and independent of the scattering vector.

4.1.2. Magnetic Scattering

Only the nuclear scattering has been considered so far. Since the neutrons have a magnetic moment, they can interact with the magnetic field of unpaired electrons via the magnetic dipole-dipole interaction. If **B** is the magnetic field generated by the spin of an electron, the magnetic interaction is given by

$$V_m = -\mu_{\mathbf{n}}\mathbf{B}, \tag{4.26}$$

with the magnetic moment of the neutron

$$\mu_{\mathbf{n}} = -\gamma_n \mu_N \sigma, \tag{4.27}$$

where σ denotes the spin operator, μ_N the nuclear magneton and $\gamma_n = -1.913$ the gyromagnetic factor of the neutron. One can derive the magnetic neutron scattering cross-section using the Born approximation. However, for ions with spin- and orbital angular momentum it takes a complicated form [130, 135]. A simple expression for the magnetic scattering length p can be given in the so-called dipole approximation, where it is assumed that spin and orbital angular momentum of the atom couple to the total angular momentum J ($L - S$-coupling) and that the momentum transfer is rather small [136]:

$$p = \frac{r_e}{2} \gamma_n g J f_m = (2.7 \cdot 10^{-5}) g J f_m(\mathbf{Q}), \tag{4.28}$$

with the Lande' splitting factor g. f_m denotes the magnetic form factor, which is the Fourier transform of the density of unpaired electrons. It accounts for the fact that the scattering occurs from a cloud of electrons, having a size comparable to the wave length of thermal neutrons. The magnetic form factor decreases with increasing momentum transfer, at small Q, however, it approaches 1. Another speciality of magnetic scattering as compared to nuclear scattering is the occurrence of a directional term in the formal description of the magnetic scattering cross section: the neutrons are only sensitive to the component of the magnetization perpendicular to the scattering vector.

The values of the magnetic and nuclear scattering length turn out to be of the same order of magnitude, thus the magnetic and nuclear structure of matter can be obtained with about the same accuracy.

4.2. Scattering and Refraction

The interaction of neutrons with matter has so far been discussed on the atomic level. However, since neutrons can be described as waves, one should also expect some kind of refraction phenomena at interfaces between different media, each having its own refractive index n. Such refractive phenomena are well known from visible light. When a light beam is passed through a lens it is deflected. The refractive index depends on the frequency ω of light and for visible wavelengths it has a value in the range between 1.2 and 2. Neutrons are reflected in a similar way, but the difference from unity of n is very

small in this case, of the order 10^{-5}. In general the refractive index can be expressed as

$$n = 1 - \delta + i\beta, \tag{4.29}$$

where δ is of order 10^{-5}. The imaginary part β accounts for the absorption in the material and is usually much smaller than δ. In the case of neutrons δ can be positive or negative. The refractive index and the scattering properties are related in a fundamental way [137]. The results will be given here without derivation.

In terms of the atomic density and atomic scattering length the decrement δ of the real part of the refractive index $n_r = 1 - \delta$ is:

$$\delta = \frac{2\pi}{k^2}\rho_a b, \tag{4.30}$$

where ρ_a is the atomic number density. If the target contains point scatterers with different scattering lengths b_j and different density ρ_j, the factor $\rho_a b$ has to be substituted by the average scattering length density $\rho_{av} = \sum_j b_j \rho_j$.

In addition to scattering, absorption processes also take place in the medium. The beam is attenuated in the material on a characteristic length scale $1/e$, which is denoted by μ^{-1}, where μ is the linear absorption coefficient. It is defined in terms of attenuation of the intensity, not in terms of attenuation of the wave amplitude; after traversing a distance z in the material the intensity is attenuated by a factor $e^{-\mu z}$, but the amplitude only by a factor $e^{-\mu z/2}$. The wave propagating in the medium is

$$e^{inkz} = e^{in_r kz} \cdot e^{-\beta kz} = e^{i(1-\delta)} \cdot e^{-\beta kz}. \tag{4.31}$$

From this equation it can be inferred that

$$\beta = \frac{\mu}{2k}. \tag{4.32}$$

4.3. Specular Neutron Reflectivity

In this section the fundamental principles of neutron reflectivity from non-ferromagnetic samples will be introduced, both within the framework of scattering and refraction. Since neutrons and x-rays are refracted in a similar way, the results derived here can directly be applied for specular x-ray scattering. One important advantage of neutron scattering compared to x-ray scattering is the magnetic interaction of neutrons with ferromagnetic samples. The reflectivity of polarized neutrons from thin ferromagnetic

4. Neutron Scattering

films will be discussed and some typical curves observed in the scattering experiments will be presented.

Reflectivity studies represent scattering processes at grazing incidence, where the momentum transfer to the sample is small. In the small Q regime, however, multiple scattering cannot be ignored and the Born approximation discussed above is too crude. One has to go beyond the kinematical limit.
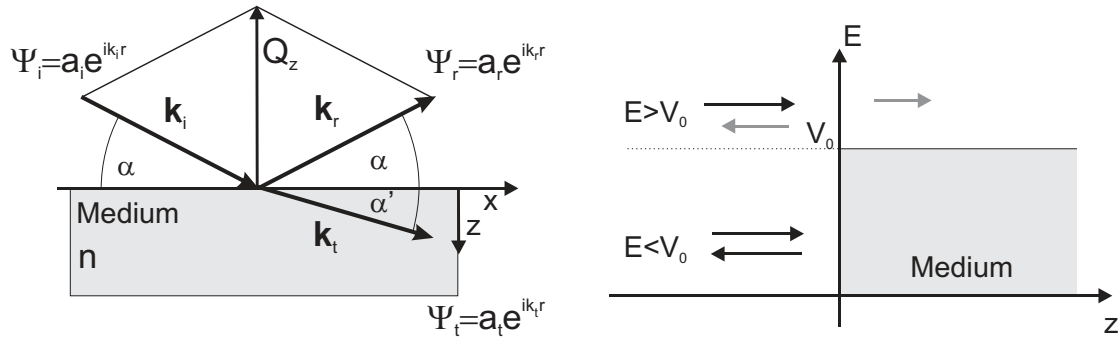

Figure 4.3.: Refractive and scattering description of the neutron reflectivity. For details see text.

It is assumed that a neutron beam impinges at a glancing angle α onto a flat and extended surface separating vacuum (air) and medium (see Fig. 4.3). The scattering problem becomes invariant under translation in the (x,y)-plane defined by the surface and the scattering vector $Q_z = 2k_{i,r}\sin(\alpha)$ points along the z-direction. The neutron beam can be considered to interact with a constant potential simply related to the scattering length density:

$$V(\mathbf{r}) = \begin{cases} \frac{2\pi\hbar^2}{m_n}\rho_{av} & : \quad z > 0 \\ 0 & : \quad z < 0 \end{cases} \tag{4.33}$$

where $\rho_{av} = \sum_j b_j\rho_j$. Thus neutron reflectivity is sensitive to the scattering length density along the z-direction of the sample only; it contains no information about the microscopic structure of the scatterer.

The scattering problem is expressed by the Schrödinger equation

$$\left[-\frac{\hbar^2}{2m_n}\Delta + V(\mathbf{r})\right]\Psi(\mathbf{r}) = E\Psi(\mathbf{r}), \tag{4.34}$$

where $\Psi(\mathbf{r})$ denotes the wave function of the neutron. With the assumptions made above only the normal component of the incoming wave vector k_i is altered by the potential

step. Thus it is the normal component of the kinetic energy

$$E_z = \frac{\hbar^2 Q_z^2}{8m_n},$$ (4.35)

which determines, whether the neutron is totally reflected from the barrier. Total reflection occurs for $E \leq V$. If $E = V$ one obtains the critical scattering vector for total reflection:

$$Q_{z,c} = \sqrt{16\pi\rho_{av}}.$$ (4.36)

Total reflection can only occur, if the scattering length density is positive.

In analogy to the refraction of light one can apply the basic principle of optics by introducing the refractive index n as defined in Sec. 4.2. This has the advantage that the results derived are simultaneously valid for neutron as well as for x-ray scattering. Furthermore, simulations of reflectivity data from multilayer systems can easily be carried out within the classical framework.

Snell's law and Fresnel equations

The reflection and refraction of a plane wave at a planar interface shall be considered, where the index of refraction changes abruptly from 1 to n (see Fig. 4.3). The incident wavevector is $\mathbf{k}_i$, and the amplitude is a_i. Analogously the reflected and transmitted wavevectors are $\mathbf{k}_r$ and $\mathbf{k}_t$ respectively, and the amplitudes are a_r and a_t. The amplitudes are related by the requirement that the wave and the derivative must be continuous at the interface $z = 0$

$$a_i + a_r = a_t.$$ (4.37)

and

$$a_i \mathbf{k}_i + a_r \mathbf{k}_r = a_t \mathbf{k}_t.$$ (4.38)

The wavenumber in vacuum is denoted by $\mathrm{k} = |\mathbf{k}_i| = |\mathbf{k}_r|$ and in the medium it is $n\mathrm{k} = |\mathbf{k}_t|$. From Eq. (4.37) together with the x-component of Eq.(4.38) one readily derives Snell's law:

$$\cos\alpha = n\cos\alpha'.$$ (4.39)

The critical angle $\alpha = \alpha_c$ for total external reflection is obtained by setting $\alpha' = 0°$ and expanding the cosines (in the regime of small angles), yielding $\alpha_c = \sqrt{2\delta}$. Thus Snell's law can be written as

$$\alpha^2 = \alpha'^2 + \alpha_c^2 - 2i\beta.$$ (4.40)

4. Neutron Scattering

The projection of Eq. (4.38) perpendicular to the interface leads to the Fresnel equations, expressing the reflected and transmitted amplitude ratios:

$$r \equiv \frac{a_r}{a_i} = \frac{\alpha - \alpha'}{\alpha + \alpha'} \ ; \ t \equiv \frac{a_t}{a_i} = \frac{2\alpha}{\alpha + \alpha'}. \qquad (4.41)$$

Here r denotes the amplitude reflectivity and t the transmittivity, respectively. The corresponding intensity reflectivity R (transmittivity T) is the absolute square of $r(t)$.

Since α' is a complex number (see Eq. (4.40)) the transmitted wave falls off with increasing depth into the material as

$$a_t e^{i(k\alpha')z} = a_t e^{ikRe(\alpha')z} e^{-kIm(\alpha')z}. \qquad (4.42)$$

The $1/e$ penetration depth Λ of the intensity is therefore given by

$$\Lambda = \frac{1}{2kIm(\alpha')}. \qquad (4.43)$$

α' can be derived from Eq. (4.40) for a given incident angle α as a function of β. If the absorption is strong, even above the edge of total reflection the penetration depth is small. In contrast, one observes a jump of the penetration depth at the edge of total reflection for the case of small absorption.

In connection with diffraction and reflection phenomena, it is often more convenient to use the wavevector transfers instead of the angular variables. With $Q \equiv 2k\sin\alpha \simeq 2k\alpha$ and $Q_c \equiv 2k\sin\alpha_c \simeq 2k\alpha_c$ one can define the dimensionless variables

$$q \equiv \frac{Q}{Q_c} \simeq \left(\frac{2k}{Q_c}\right)\alpha \ ; \ q' \equiv \frac{Q'}{Q_c} \simeq \left(\frac{2k}{Q_c}\right)\alpha'. \qquad (4.44)$$

This allows to rewrite Eq. (4.40), yielding

$$q^2 = q'^2 + 1 - 2ib_\mu, \qquad (4.45)$$

where the parameter b_μ is related to the absorption coefficient μ (see Sec.4.2) through $b_\mu = \frac{2k}{Q_c^2}\mu$.

For the calculation of the reflectivity, transmittivity and penetration depth, one needs the values for the absorption length μ^{-1} and the scattering length density. The complex number q' can then be derived from Eq. (4.45) and one finally obtains:

$$r(q) = \frac{q - q'}{q + q'} \ ; \ t(q) = \frac{2q}{q + q'} \ ; \ \Lambda(q) = \frac{1}{Q_c Im(q')}. \qquad (4.46)$$

Far away from the region of total reflection, i.e. $q \gg 1$, the solution to Eq. (4.45) yields $Re(q') \simeq q$, recalling that $b_\mu \ll 1$. Rewriting the amplitude reflectivity $r(q)$ as $r(q) = (q^2 - q'^2)/(q + q')^2$ one obtains $r(q) \simeq (2q)^{-2}$ in the considered limit, i.e. the intensity of the reflectivity precipitously falls off as $R(q) \simeq (2q)^{-4}$.

Multilayer Systems

So far only the reflectivity from a single interface has been considered. As the scattering from multilayer structures has attracted particular interest in recent years and plays an important role in this thesis, the calculation of the reflectivity will be extended to the case of a stratified medium. One important method for this purpose was developed by Parratt [138]. This so-called Parratt formalism describes the reflectivity of a system with N layers, sitting on the top of an infinitely thick substrate (see Fig. 4.4).
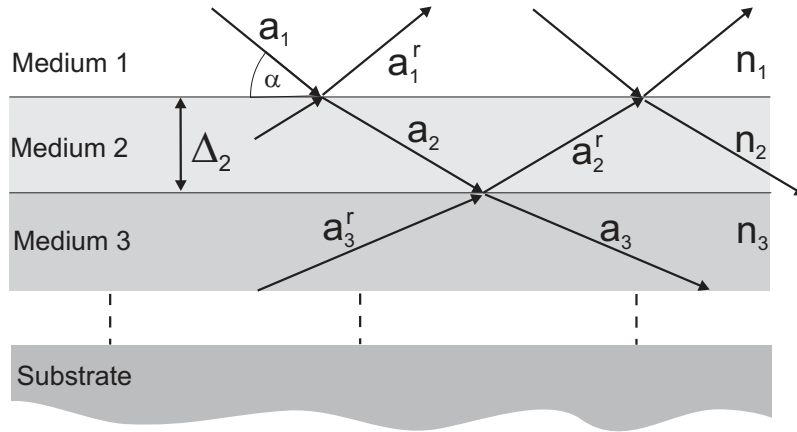

Figure 4.4.: Sketch of reflection and refraction for stratified homogeneous media. The amplitude of the reflected and refracted wave in the j-th layer is denoted by a_j^r and a_{j+1}, respectively .

Each layer in the stack has a refractive index $n_j = 1 - \delta_j + i\beta_j$ and the thickness Δ_j. The z-component of the wavevector in the j-th layer, $k_{z,j}$ is determined from the total wavevector $k_j = n_j k$ and the x-component, $k_{x,j}$, which is conserved through all layers, so $k_{x,j} = k_x$. The value of $k_{z,j}$ is then given by the relation

$$k_{z,j}^2 = (n_j k)^2 - k_x^2 = (1 - \delta_j + i\beta_j)^2 k^2 - k_x^2 \simeq k_z^2 - 2\delta_j k^2 + i2\beta_j k^2. \qquad (4.47)$$

With $Q_j = 2k_j \sin \alpha_j = 2k_{z,j}$, the wavevector transfer in the j-th layer is

$$Q_j = \sqrt{Q^2 - 8k^2\delta_j + i8k^2\beta_j}. \qquad (4.48)$$

The reflectivity at each interface obeys Fresnel's law. This allows to recursively calculate the total reflectivity amplitude at the interface between the vacuum and the first layer. The first step is to determine the reflectivity from the interface between the bottom of the N-th layer and the substrate. Assuming that the thickness of the substrate is infinitely thick, there are no multiple reflections to consider and Eq. (4.46) yields

$$r'_{N,\infty} = \frac{Q_N - Q_\infty}{Q_N + Q_\infty}. \tag{4.49}$$

The prime is used to denote a reflectivity amplitude that does not include multiple scattering effects. For the calculation of the reflectivity from the top of the N'th layer, multiple scattering and refraction have to be allowed. Considering the continuity at the interface and including a phase factor $p_N^2 = e^{i\Delta_N Q_N}$ for the addition of multiple scattered waves, the reflectivity of the N-th layer can be evaluated as

$$r_{N-1,N} = \frac{r'_{N-1,N} + r'_{N,\infty}p_N^2}{1 + r'_{N-1,N}r'_{N,\infty}p_N^2}. \tag{4.50}$$

The process can be continued recursively until the total reflectivity amplitude is obtained.

Roughness and Interdiffusion

Up to now, systems with sharp, flat interfaces are assumed for the calculation of the reflectivity of multilayers. In the limit of the kinematical approach, where Q is much larger than Q_c, this leads to the Fresnel reflectivity (see above). In real systems the interface may be rough with peaks and troughs over a large range of length scales with a fractal-like structure (height fluctuations). Or the boundary may be graded with one material diffused into the other (see Fig. 4.5).

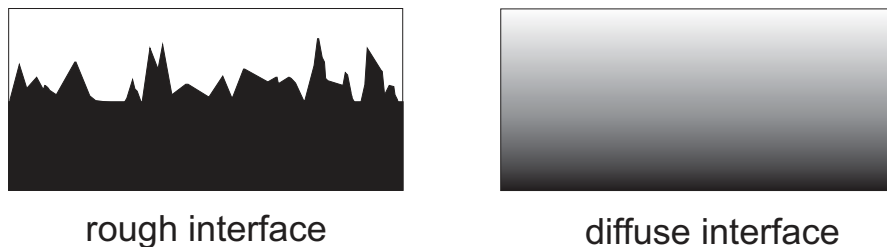

rough interface   diffuse interface

Figure 4.5.: Roughness and interdiffusion at the interface can result in identical specular reflectivities.

In both the rough and the graded cases, the laterally averaged density profile of the

interface can be described by an error function [137]

$$f(z) = erf\left(\frac{z}{\sqrt{2}\sigma}\right),$$ (4.51)

where σ is a measure of the width of the graded region or the rms (root mean square) roughness, respectively. Therefore, specular reflectivity cannot distinguish between rough and graded interfaces. The reflectivity is reduced by a factor very much like the Debye-Waller factor [139]

$$R(Q) = R_F(Q)e^{-Q^2\sigma^2}.$$ (4.52)

In the case of the graded interface the lost intensity goes into the transmitted beam as there are no potential gradients in any other direction than normal to the surface. In the case of the rough interface the intensity is scattered in the off-specular region. This can yield information about in-plane coherence lengths (see Sec. 4.4).

In Fig. 4.6 simulated neutron reflectivities for a series of systems are shown together with a schematic illustration in the left column. The curves were calculated using reasonable instrumental parameters of the reflectometer ADAM, which was used for most of the neutron measurements within this thesis (see Sec. 4.5). Fig. 4.6(a) shows the reflectivity curve of a semi-infinite Al_2O_3 crystal. The critical wavevector Q_c, up to which total reflection occurs, is clearly visible. As the crystal has a perfect smooth interface, the scattered intensity drops as Q^4 above Q_c (Fresnel reflectivity). If the boundary is rough, the drop in the reflected intensity is larger.

In the case of a thin metallic film grown on the substrate (Fig. 4.6(b)) interference fringes superimposed on the Fresnel reflectivity will occur. These arise from the interferences of waves reflected from the interfaces vacuum-film and film-substrate, respectively.

In Fig. 4.6(c) the reflectivity curve of a metallic superlattice, consisting of layers of the two metals A and B, with n repetitions of the double layer period Λ is drawn. The periodic internal structure gives rise to so-called superlattice peaks at positions of integer multiples of $Q_{SL} = 2\pi/\Lambda$ in addition to the total thickness oscillations of the thin film system.

4.3.1. Polarized Neutron Reflectivity

In the previous chapter the structural characterization of samples has been discussed. Since the neutrons exhibit a spin, they can also interact with the magnetic induction **B** in the sample plane as described in Sec. 4.1.2. As the wavevector transfer is small in
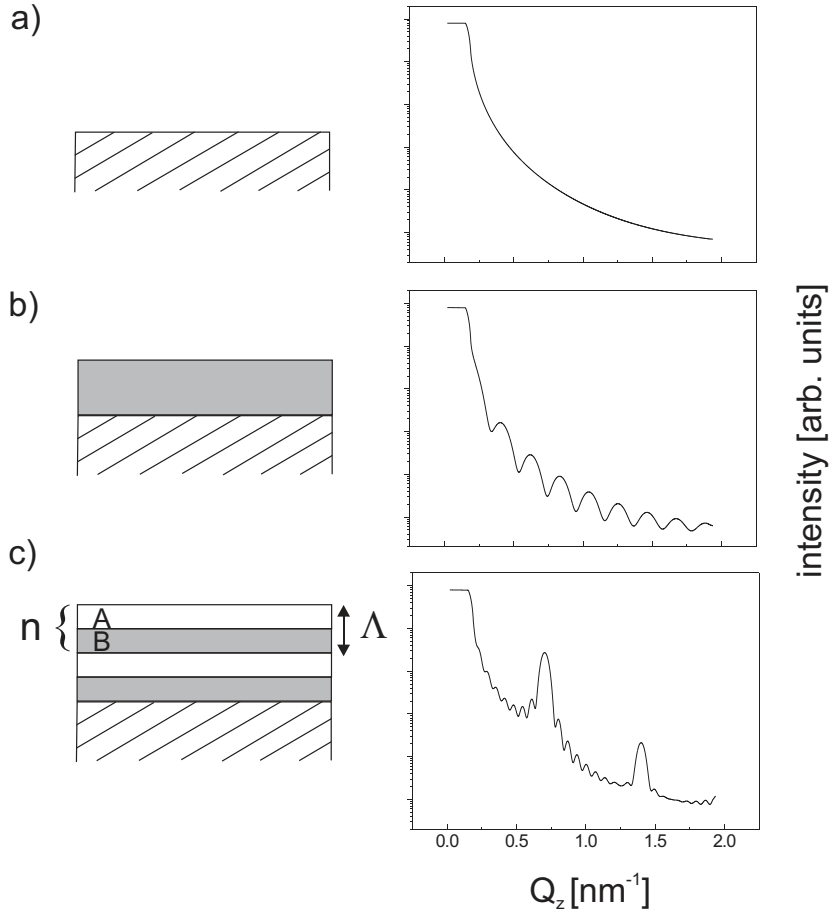
Figure 4.6.: Simulated neutron reflectivity curves for an infinitely thick crystal (substrate) (a), a thin non-magnetic film (b) and a superlattice (c), together with a schematic illustration in the left column.

reflectivity, the nuclear and magnetic density profile normal to the surface will be probed, no information on the local atomic order can be derived. If the neutron polarization, i.e. the neutron magnetic moment with respect to the scattering plane, is fixed and the polarization state of the scattered neutrons is analyzed before the detector, the NR is called polarized neutron reflectivity (PNR). In the experiment four reflectivity curves are measured, denoted as $R^{++}, R^{--}, R^{+-}, R^{-+}$. Here the first index '+' or '-' refers to the incident neutron spin state, and the second index to the neutron spin state after reflection from the sample. Typically, a neutron is called an 'up' neutron when its moment is parallel to an applied magnetic field, defining the neutron quantization axis, and 'down', if its moment is antiparallel. The reflectivities R^{++} and R^{--} are those without a change in the spin state and are called non-spin-flip (NSF) channels, whereas R^{+-} and R^{-+} are spin-flip (SF) channels. The scattering geometry for PNR studies used throughout this thesis is depicted in Fig. 4.7. The y-axis is the quantization axis
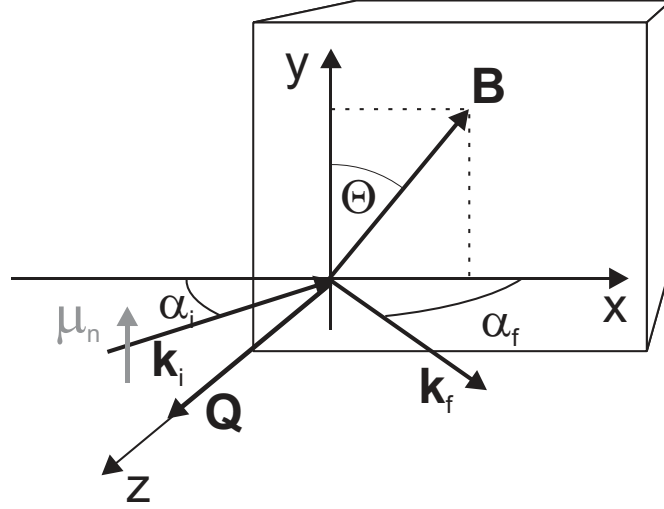
Figure 4.7.: Scattering geometry for PNR studies. The y-axis is the quantization axis for the neutrons and the non-spin-flip axis and the x-direction is the spin-flip axis. For specular reflectivity studies the scattering vector Q is parallel to the z-axis.

for the neutron magnetic moment μ_N, which is interacting with the in-plane magnetic induction **B** in the sample. For specular reflectivity $\alpha_i = \alpha_f$ holds and the scattering vector $\mathbf{Q}_z$ is parallel to the z-axis and perpendicular to the surface.

In the dynamical theory the scattering of polarized neutrons can be calculated in an exact way, starting from basic equations. By fitting the measured polarized neutron reflectivities, the depth dependent magnetization profile can be derived beside structural information like film thickness and interfacial roughness.

The interaction potential of the magnetic moment of a neutron with a magnetic induction **B** in the sample is $V_m = -\mu_{\mathbf{N}}\mathbf{B}$ (see Sec. 4.1.2). Thus the total scattering potential seen by the neutrons can be written as an operator V:

$$\mathbf{V} = \begin{pmatrix} V_{++} & V_{+-} \\ V_{-+} & V_{--} \end{pmatrix} = \frac{2\pi\hbar^2}{m}\rho_a \begin{pmatrix} b & 0 \\ 0 & b \end{pmatrix} - \mu_{\mathbf{n}} \begin{pmatrix} B_z & B_x - iB_y \\ B_x + iB_y & -B_z \end{pmatrix}. \quad (4.53)$$

In analogy to the nuclear scattering length density $\rho_a b$ it is useful to define the magnetic scattering length density $\rho_a p$ which is related to the magnetic induction via

$$\mathbf{B} = \frac{2\pi\hbar^2}{|\mu_n|m_n}\rho_a\mathbf{p}, \quad (4.54)$$

with $\mathbf{p} = p\hat{e}$, where p is given by Eq. (4.28) and $\hat{e}$ is parallel to the mean magnetic induction in the sample. Using this relation, the interaction potential can be expressed

4. Neutron Scattering

as:

$$\mathbf{V} = \frac{2\pi\hbar^2}{m}\rho_a\left[\begin{pmatrix} b & 0 \\ 0 & b \end{pmatrix} + \begin{pmatrix} p\cos\Theta & p\sin\Theta \\ p\sin\Theta & -p\cos\Theta \end{pmatrix}\right]. \tag{4.55}$$

With this effective potential the Schrödinger equation has to be solved, considering the two possible eigen-states of the neutron. The particle behaviour in this case is formally described by the two-component vector of states, i.e. $\Psi(z) = (\Psi_+(z), \Psi_-(z))$, $\Psi_+(z)$ for neutrons polarized parallel to the y-direction, and $\Psi_-(z)$ for neutrons polarized antiparallel to the y-direction. The scattering of polarized neutrons is then described by a pair of coupled, second order differential equations:

$$\frac{\partial^2}{\partial z^2}\Psi_+(z) + \left(\frac{Q^2}{4} - \frac{2m}{\hbar^2}V_{++}(z)\right)\Psi_+(z) - \frac{2m}{\hbar^2}V_{+-}(z)\Psi_-(z) = 0, \tag{4.56}$$

$$\frac{\partial^2}{\partial z^2}\Psi_-(z) + \left(\frac{Q^2}{4} - \frac{2m}{\hbar^2}V_{--}(z)\right)\Psi_-(z) - \frac{2m}{\hbar^2}V_{-+}(z)\Psi_+(z) = 0. \tag{4.57}$$

Some conclusions can directly be drawn without solving the Schrödinger equation. When the off-diagonal elements of the scattering potential $V_{i,j}$ with $i \neq j$ are zero, Eqs. (4.56) and (4.57) are decoupled and only NSF scattering occurs. In this case the vector of the magnetic induction of the sample **B** has to be oriented along the y-axis. Alternatively, if the magnetization is aligned parallel to the x-axis, $V_{i,j}$ with $i = j$ are zero and the V_{+-}, V_{-+} potentials flip the neutron spin from up to down and vice versa. Thus quantitative analysis of all four scattering channels in an PNR experiment allows for the determination of the magnitude and orientation of the magnetic induction in the sample.

For the analysis of the measured reflectivities some important points should be noted here. The diagonal elements of the scattering potential V_{++} and V_{--} contain nuclear as well as magnetic contributions, whereas V_{+-} and V_{-+} are solely of magnetic origin. As the 'up' and 'down' neutrons experience different scattering potentials when interacting with a ferromagnetic sample, the critical vector for the nuclear scattering Q_c has to be modified. For the case of NSF scattering Q_c is given by [140]

$$\mathbf{Q}_c^{\pm} = \sqrt{16\pi\rho_a(b\pm p)}\hat{z}. \tag{4.58}$$

Here $\pm$ refers to the up and down spin polarization, and $\hat{z}$ is a unit vector pointing in the direction of the scattering vector normal to the surface.

For an angle Θ of the magnetization vector with respect to the y-axis, the difference

$$R^{++} - R^{--} = 2p\cos\Theta \propto 2B_y \qquad (4.59)$$

is proportional to the y-component of the magnetization vector, whereas the spin-flip reflectivities are degenerate, and

$$R^{+-} + R^{-+} = 2p\sin^2\Theta \propto B_x^2 \qquad (4.60)$$

is proportional to the square of the x-component of the magnetic induction.

The solution of Eqs. (4.56) and (4.57) shall not be given here, but several algorithm to simulate PNR data have been provided in the literature [141, 142, 143], among them the supermatrix (SM) method and the matrix-recursion (MR) formalism [144, 145, 146, 147, 148]. The latter one is based on a generalized Parratt formalism. A potential well structure composed of slabs of constant potential is assumed. Then all transmitted and reflected amplitudes are calculated via recursion. Interface roughness can numerically be realized by a slicing method [149], where the interface region is divided into different layers with sharp boundary and constant potential.

PNR scans from some artificial multilayers shall now be exemplary discussed to show some typical features in the reflectivity curves. Fig. 4.8(a) shows a simulation of a specular polarized neutron scan for NSF and SF channels of the multilayer $[Co_2MnGe(5nm)/V(4nm)]_{10}$. A schematic illustration depicts the magnetic order in the sample. The Co_2MnGe layers are ferromagnetically saturated, with the magnetization vectors of each layer being parallel to the applied field, providing the neutron guiding field. The chemical periodicity Λ_{chem} gives rise to Bragg peaks at multiples of $Q_z = 2\pi/\Lambda_{chem}$. As the sample exhibits a net magnetization, the intensities R^{++} and R^{--} are split, the difference being proportional to M. Since there is no component of the magnetization perpendicular to the neutron polarization axis, no spin-flip scattering occurs. If the magnetization vectors of the ferromagnetic layers are aligned parallel and antiparallel to the polarization axis, forming an antiferromagnetically coupled multilayer (see Fig. 4.8(b)), there are additional Bragg peaks in the reflectivity at half integer values of $2\pi/\Lambda_{chem}$ due to a doubling of the magnetic period over the chemical period ($\Lambda_{mag} = 2\Lambda_{chem}$). If the antiferromagnetic alignment is perfect, the sample has no net magnetization and thus the splitting of the NSF channels vanishes. Fig. 4.8(c) shows a perfect antiferromagnetic coupled multilayer with the magnetization vectors forming an angle $\Theta = 45°$ with respect to the polarization axis. The difference to the previous case is the intensity in the SF channel due to a component of the magnetization being per-
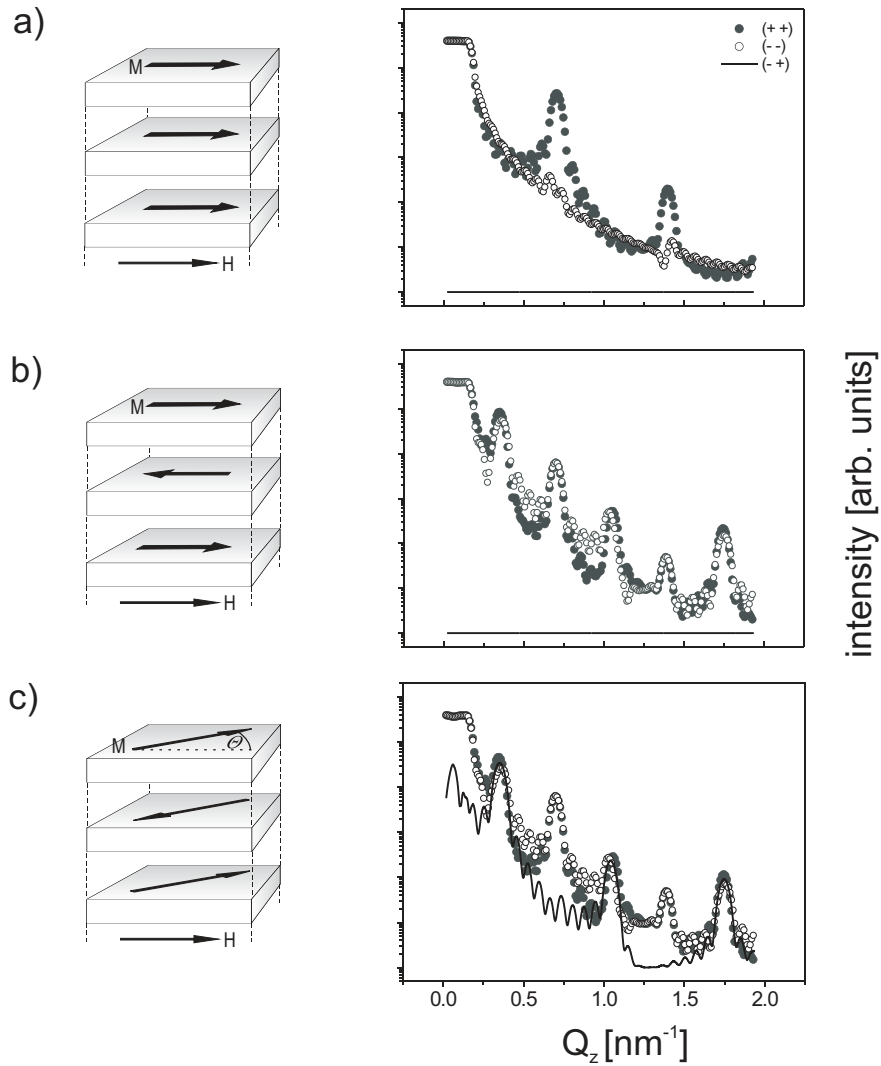
a)

b)

c)

Figure 4.8.: Simulated neutron polarized reflectivity curves for a [Co₂MnGe(5nm)/V(4nm)]₁₀ multilayer in ferromagnetic saturation (a), with perfect antiferromagnetically coupled Co₂MnGe layers collinear to the neutron guiding field (b) and with the magnetization of the antiferromagnetic coupled layers forming an angle Θ with respect to the guiding field (c).

pendicular to the polarization axis. Since the SF intensity is of purely magnetic origin, it only shows antiferromagnetical *half-order* Bragg peaks, but no chemical Bragg peaks.

4.4. Off-specular Scattering

Specular PNR has proven to be a powerful tool for the investigation of the chemical and magnetic depth density profiles of magnetic heterostructures, but it does not provide any direct information about lateral length scales of the films, completely ignoring their crystalline structure and possible large scale inhomogeneities. Thus it is for instance not possible to distinguish between interdiffusion and roughness. Information on the in-plane structure of the sample is only contained in scans with an in-plane component of the scattering vector $\mathbf{Q}$. Hence the morphology of a layered system can be unveiled by studying the diffuse (off-specular) scattering . Off-specular neutron scattering can yield information about the lateral dimensions of magnetic domains in the film and their out-of-plane correlation length. Since the coherence length of the neutron beam is finite, the information yielded is statistical, i.e. no microscopic pictures can be drawn.

For the theoretical calculation of diffuse scattering at grazing incidence one has to go beyond the Born approximation (BA), since total external and multiple internal reflections have to be taken into account. In this case the distorted-wave Born approximation (DWBA) has to be used for a quantitative description of experiments. Nevertheless, the BA, where the scattering is assumed to be weak and multiple scattering is neglected, shall be presented here, since this formalism has the (didactic) advantage to provide an easy approach to the physics behind the off-specular scattering.
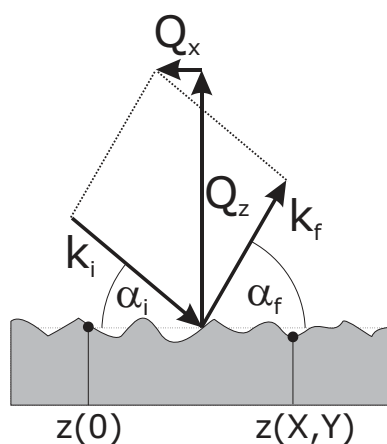
4.4.1. Born Approximation

Figure 4.9.: Scattering from a rough surface.

Fig. 4.9 shows the scattering of an neutron beam from a single rough surface. A beam of intensity I_0 is incident at a angle α_i, and scattered at an exit angle α_f. In the

4. Neutron Scattering

Born approximation the reflected amplitude is calculated by summing all of the beams scattered from volume elements d^3r within the illuminated sample volume V, taking into account the appropriate phase factors. The scattering amplitude is then given by

$$r_V = -\rho_a b \int_V d^3r e^{i\mathbf{Qr}}. \tag{4.61}$$

For simplicity reasons, magnetic scattering is not considered. The volume integral can be transformed to a surface integral using Gauss' theorem. For the evaluation of the scattering cross-section (absolute square of the scattering amplitude) it is assumed that the difference in heights of the sample surface, $[h(x, y) - h(x', y')]$, is a Gaussian random variable, whose distribution depends on the relative difference in position $(x - x', y - y')$ only. The ensemble average of height differences is described by the function $g(x, y)$, with

$$g(x, y) = \langle [h(0, 0) - h(x, y)]^2 \rangle. \tag{4.62}$$

This yields the scattering cross-section [150]

$$\frac{d\sigma}{d\Omega} = \left(\frac{\rho_a b}{Q_z}\right)^2 L_x L_y \int_S dx dy e^{-Q_z^2 g(x,y)} e^{i(Q_x x + Q_y y)}, \tag{4.63}$$

where $A = L_x L_y$ is the illuminated area. The characteristics and thus the ensemble average of height differences from surfaces can be very different, depending on the model assumed. Here, the case of a correlated, isotropic rough surface with a cut-off length shall be discusses in more detail.

Since the correlations are isotropic, $g(x, y)$ depends only on $r = \sqrt{x^2 + y^2}$. The height fluctuations shall remain finite as $r \to \infty$, which is best explored by writing

$$g(r) = 2\sigma^2 - 2C(r) \tag{4.64}$$

$$= 2\sigma^2 - 2\sigma^2 e^{-(r/\xi)^{2h}}, \tag{4.65}$$

where the height-height correlation function $C(r) = < z(0)z(r) >$ has been introduced. The average height distribution is given by the rms roughness σ, ξ is the lateral correlation length and serves as an effective cut-off length for the roughness. The exponent h is the so-called hurst parameter and determines the texture of the roughness. Small values of h produce extremely jagged surfaces, while values approaching 1 lead to smooth hills and valleys. The resulting cross-section can be separated into a specular and off-specular

term, yielding

$$\left(\frac{d\sigma}{d\Omega}\right)_{\text{diffuse}} = \frac{L_x L_y}{Q_z^2} \rho^2 e^{-Q_z^2 \sigma^2} \int_A dx dy \left(e^{Q_z^2 C(r)} - 1\right) e^{-i(Q_x x + Q_y y)}, \qquad (4.66)$$

for the diffuse term only.

For multilayer systems, Eq. (4.66) has to be generalized by introducing height-height correlation functions

$$C_{ij}(R) = \frac{\sigma_i \sigma_j}{2} \left(\exp\left(-(R/\xi_i)^{2h_i}\right) + \exp\left(-(R/\xi_j)^{2h_j}\right)\right) e^{-|z_i - z_j|/\xi_\perp}, \qquad (4.67)$$

for each pair of interfaces. The cross-section is then evaluated by summing the contributions of each interface over all interfaces i and j [151, 152]

$$\left(\frac{d\sigma}{d\Omega}\right)_{\text{diffuse}} = \frac{L_x L_y}{Q_z^2} \sum_{ij} \Delta\rho_i^2 \Delta\rho_j^{*2} e^{-Q_z^2(\sigma_i^2 + \sigma_j^2)/2} e^{iQ_z(z_i - z_j)} S_{ij}(\mathbf{Q}). \qquad (4.68)$$

Here $S_{ij}(\mathbf{Q})$ represents the integral in Eq. (4.66) with the height-height correlation length C replaced by C_{ij}, $\Delta\rho_i$ is the difference in the scattering length density ρ on the two sides of the i-th interface. The vertical correlation of the roughness is expressed by the perpendicular correlation length $\xi_\perp$. For the case of perfect vertical correlation, when $\xi_\perp$ is larger than the total thickness of the multilayer, the diffuse intensity will be peaked at the Bragg conditions visible as Bragg-sheets as shown in Fig. 4.10(a). If the interface roughness is completely uncorrelated ($\xi_\perp = 0$) the total diffuse intensity is an incoherent sum of the intensities diffusely scattered from each layer and will be spread out uniformly in Q_z (see Fig. 4.10(b)) [153, 154].

4.4.2. Distorted-Wave Born Approximation

At glancing incidence the kinematical approach is no longer valid and the distorted-wave Born approximation has to be applied. DWBA [155] represents a typical example of the perturbation theory approach which generally implies to use an exact solution of the simplified reference Hamiltonian as a starting point for the iteration over the difference between this Hamiltonian and that to be solved. In most of the cases only the first iteration is accounted for. In the form of DWBA suggested by Sinha et al. [150] for x-ray off-specular scattering, the zero approximation assumes an exact solution of the Schrödinger equation for the reflection potential, while the residual potential is treated
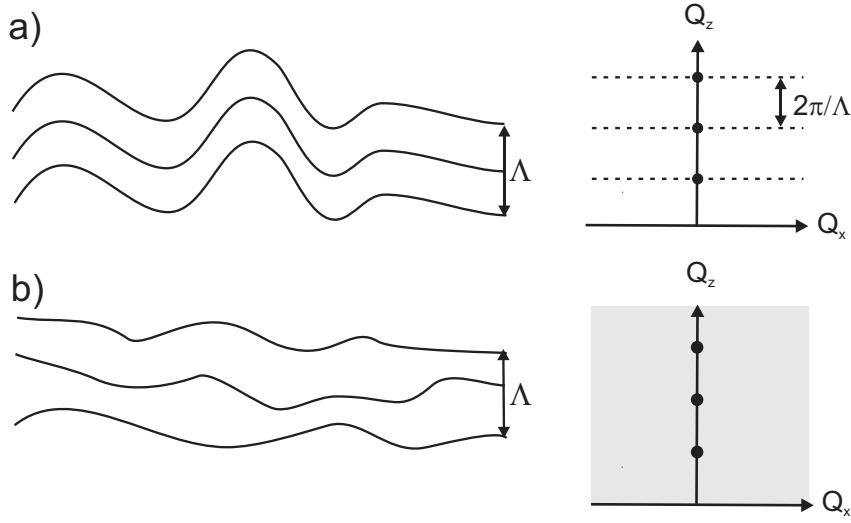
Figure 4.10.: Schematic view of perfectly correlated (a) and uncorrelated (b) interfacial roughness from layer to layer and corresponding reciprocal-space representation.

as a perturbation. The differential cross-section for scattering by a rough surface yields:

$$\left(\frac{d\sigma}{d\Omega}\right)_{\text{diffuse}} = \frac{L_x L_y}{16\pi^2}\left|k_0^2(1-n^2)\right|^2 |T(\alpha_i)|^2 |T(\alpha_f)|^2 S(\mathbf{Q}_t), \qquad (4.69)$$

where k_0 is the magnitude of the wave vector in free space, $T(\alpha_{i,f})$ are the transmission coefficients of the surface for angles $\alpha_{i,f}$ and

$$S(\mathbf{Q}_t) = \frac{1}{Q_z^t Q_z^{t*}} e^{\sigma^2(Q_z^{t2}+Q_z^{t*2})/2} \int_S dX dY \left(e^{Q_z^t Q_z^{t*}C(X,Y)} - 1\right) e^{-i(Q_x X + Q_y Y)}. \qquad (4.70)$$

$\mathbf{Q}_t$ is the wave vector transfer inside the reflected medium and $C(x,y)$ the height-height correlation function introduced above. The DWBA formalism can be generalized for the case of x-ray scattering from multilayers [151, 153].

The polarization dependence of diffusely scattered neutrons has not yet been considered. This has been realized by Toperverg using a matrix representation of the DWBA [148]. This algorithm allows to analyze off-specular scattering from layered systems with any complex arrangements of inter-layer magnetization, as well as exhibiting an in-plane magnetic structure. Due to the complexity of the resulting expressions they will not be stated here.

4.5. Experimental Setup

The spin polarized neutron reflectivity measurements have mainly been performed with the reflectometer ADAM [156] at the Institut Laue-Langevin (ILL) in Grenoble, France. The ADAM machine is a fixed wavelength angle dispersive reflectometer operating at a neutron wavelength of $\lambda = 0.441$ nm with a wavelength resolution of 0.5%. Fig. 4.11 shows a schematic picture of the machine. The 'white' neutron beam provided by ILL's horizontal cold source is monochromated by a focussing graphite monochromator, which is aligned to select the maximum of the Maxwellian distribution of the neutron intensity. A Beryllium filter suppresses the higher order wavelengths. After passing collimation slits the neutron beam impinges on the sample, mounted on a one-axis, two-circle diffractometer with a horizontal scattering plane. The slits enable a very high resolution within the scattering plane, while in the vertical direction the beam is optimized for maximum intensity. The scattered neutrons are detected by either a pencil detector or a position-sensitive detector (PSD). The latter one has the advantage that it covers not only the specular reflection, but also collects off-specular intensity at the same time.

For spin polarized neutron measurements on magnetic systems the incoming beam can be polarized and an analysis of the spin state of the scattering process is possible. Therefore, the incident monochromatic and unpolarized beam is polarized by a supermirror operating in transmission, with a typical efficiency of 97% (see Fig. 4.12).
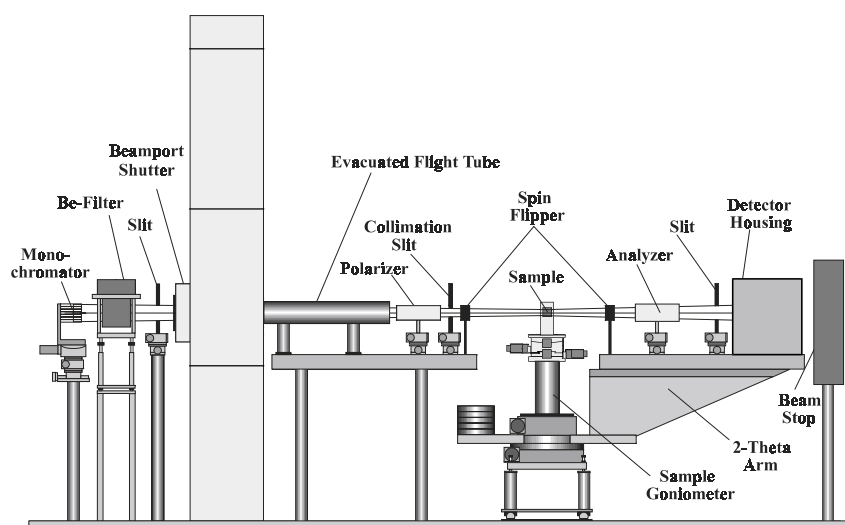

Figure 4.11.: Cutaway view of the ADAM reflectometer at the Institut Laue-Langevin in Grenoble, France.

The polarizing capability of the magnetic supermirror stems from the fact that the two possible neutron states exhibit different critical angles for total reflection. Hence, one polarized beam is refracted and the other one with opposite polarization is reflected. To change the polarization, a spin flipper is placed in front of the sample. In an analog fashion a second spin flipper and a second supermirror mounted on the detector side allow for spin analysis of the scattered beam. Thus all four cross sections can be measured. Furthermore, various sample environments can be realized on the ADAM instrument. For the measurements within this thesis a conventional electro-magnet, providing fields up to 0.8 T, has been used. A closed-cycle refrigerator (DISPLEX) allows to access temperatures between 10 K and 600 K.
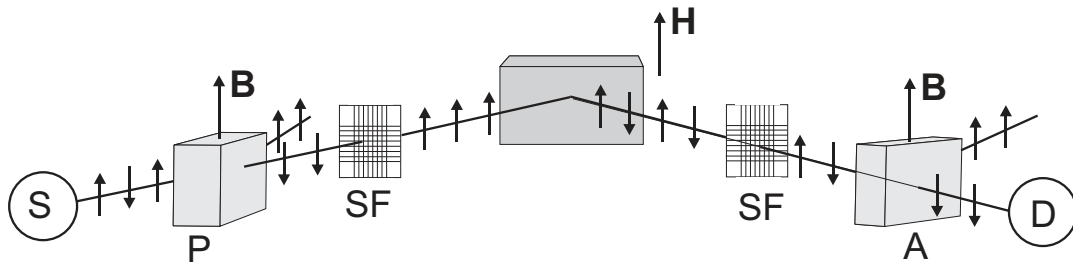

Figure 4.12.: Schematic outline of the ADAM reflectometer with polarization analysis. The incident beam from the source S is polarized by the first supermirror P. The polarization can be changed by spin-flippers SP before and after the sample. The second supermirror A analyzes the polarization state before the neutrons are counted by the detector D. The setup shows the $(+, -)$ configuration with the first spin-flipper on and the second off.

5. X-ray Resonant Magnetic Scattering

X-ray scattering is a capable tool for the determination of the depth dependent chemical (structural) profile of thin films and artificial multilayers, but does not directly yield information on the magnetic structure. This gap is closed by x-ray resonant magnetic scattering (XRMS). XRMS is a combination of x-ray scattering and the x-ray magnetic circular dichroism (XMCD), which is a magneto-optical (MO) effect and therefore dependent on the magnetic order in the sample.

Magneto-optical effects are a well known phenomenon for wavelengths in the optical part of the spectrum, since Faraday 1845 observed the rotation of the polarization vector during transmission of linearly polarized light through a magnetic material [157]. About 40 years later a completely analogous phenomenon, the magneto-optical Kerr effect (MOKE), was found by Kerr for light, which was reflected by a magnetized sample [158]. Further MO effects were found, which differ partly only with regard to the geometry of the experimental setups. There are three general geometries used to measure the Kerr effect, which are displayed in Fig. 5.1. In the polar (P-MOKE) geometry, the
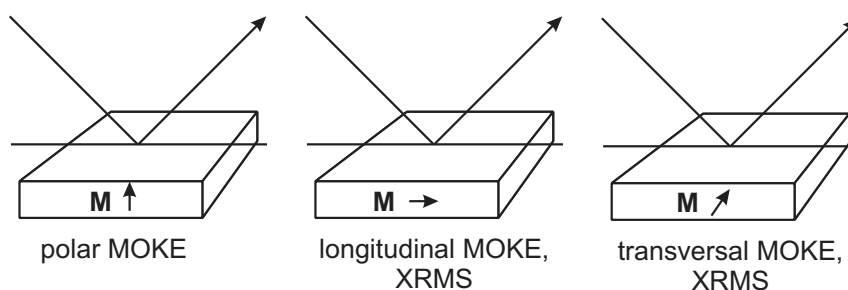

Figure 5.1.: Geometry of the three magneto-optical Kerr effects.

magnetization is perpendicular to the reflecting surface. In the longitudinal (L-MOKE) configuration the magnetization is parallel to the scattering plane and sample surface. The Kerr effect generates a polarization rotation of the reflected beam with respect to the scattering plane [159]. By contrast, in the transverse Kerr effect (T-MOKE), where
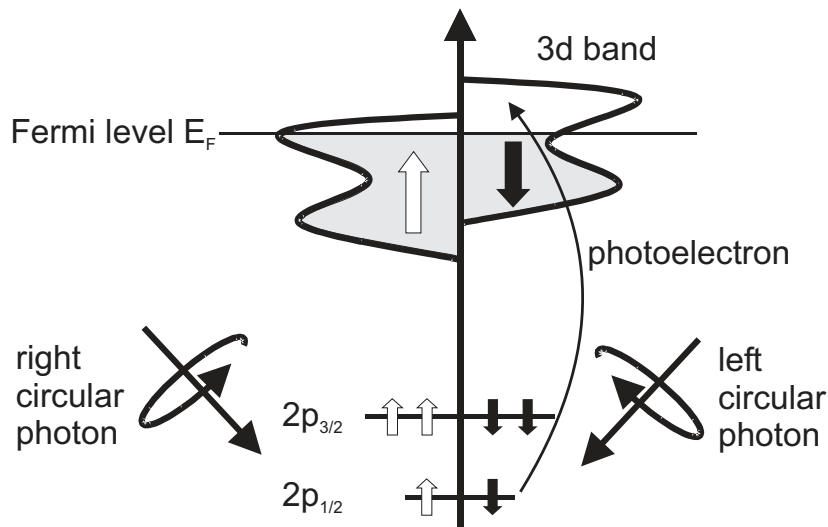
Figure 5.2.: Picture of the spin-dependent absorption process.

the magnetization is oriented perpendicular to the scattering plane and parallel to the surface, the change of the amplitude of the reflected light is measured [160, 161].

Already in the beginning of the last century the first attempts were started proving effects also in the x-ray range of the light. Indeed, suitable experiments became only possible by the availability of intensive x-ray radiation of well defined polarization as it can be produced by a synchrotron. The most popular MO effect in the x-ray range was predicted 1975 by Erskine and Stern [162]. They showed that the absorption cross section of circularly polarized light at the $M_{2,3}$ absorption edges of ferromagnetic Ni for the magnetization direction parallel or antiparallel to the light propagation should be different. This so-called x-ray magnetic circular dichroism (XMCD) was later observed experimentally by Schütz et al. [163] at the iron K edge.

The microscopic origin of the XMCD effect is based on electronic transitions from spin-orbit split initial states to exchange-split final states. While neutrons sense the magnetic field distribution inside a sample, XMCD probes the local atomic moments via resonant absorption. By tuning the photon energy close to a specific absorption edge, it is possible to study the magnetism of different elements separately.

Resonant absorption of circularly polarized light occurs for any of the dipole transitions, for instance in the case of $3d$ transition metals from $2p$ core states to $3d$ valence states. Due to $\mathbf{L} \cdot \mathbf{S}$ coupling, the initial p state is split in $p_{1/2}$ and $p_{3/2}$, as depicted in Fig. 5.2. Considering only dipole transitions, x-ray excitation leads to two absorption lines corresponding to transitions from $2p_{1/2}$ to $3d_{3/2}$ (L_2) and from $2p_{3/2}$ to $3d_{5/2}$ (L_3). In the case of ferromagnetic transition metals, the $3d$ band is exchange split, giving rise to a different electron density of states at the Fermi level for majority as compared to

minority electrons. Due to the exchange splitting of initial states, the transitions L_2 and L_3 exhibit different absorption coefficients for right and left circular polarized light. For non-magnetic materials the absorption coefficients are identical. Beside the element-sensitivity XMCD has at least two more attractive features. A quantitative analysis of the absorption lines via sum rules [164, 165] provides information on the spin and orbital magnetization separately, while most other methods (bulk magnetization, neutron scattering, etc.) are sensitive to the total magnetization only. Lastly, XMCD is very sensitive which allows it to be used to determine extremely small magnetic moments, even magnetic moments of $0.001\mu_B$ per atom can be detected [166].

XRMS is the scattering counterpart of XMCD [167, 168], combining the advantages of XMCD and conventional x-ray scattering. It has been demonstrated for the first time by Gibbs et al. [19] and Hannon et al. [20] in 1988. Today XRMS has become a standard tool for the study of magnetization in multilayers, magnetization reversal processes in individual layers and magnetic roughness.

This chapter provides a short introduction into the basic theory of magneto-optical effects in a quantum mechanical treatment. The main focus here lies on the XRMS effect. After a brief discussion of the polarization dependence of the scattering factor, the relation between scattering and absorption phenomena is presented. Subsequently magnetic reflectivity and magnetic diffuse scattering are described.

5.1. Quantum Mechanical Description

In this section a short introduction is given to the subject of the quantum mechanical description of resonant x-ray scattering. As seen for the case of neutron scattering, the scattering process can be described by cross-sections. For their derivation the quantity of interest is the transition rate probability W between the initial and final states of the excited atomic electrons, when they interact with light. The Hamiltonian of an atomic electron in a quantized electromagnetic field [169] can be split into contributions of the undisturbed electron system, free radiation field and interaction Hamiltonian, $\mathcal{H} = \mathcal{H}_0 + \mathcal{H}_{\mathrm{rad}} + \mathcal{H}_{\mathrm{int}}$, where

$$\begin{aligned} \mathcal{H}_{\mathrm{int}} &= -\frac{e}{mc}\mathbf{A}\cdot\mathbf{p} + \frac{e^2}{2mc^2}\mathbf{A}^2 \\ &\equiv \mathcal{H}_1 + \mathcal{H}_2. \end{aligned} \tag{5.1}$$

The Hamiltonian $\mathcal{H}_{int}$ completely determines the scattering processes of light by electrons. Here the spin of the electron is neglected in the description, as the spin dependent
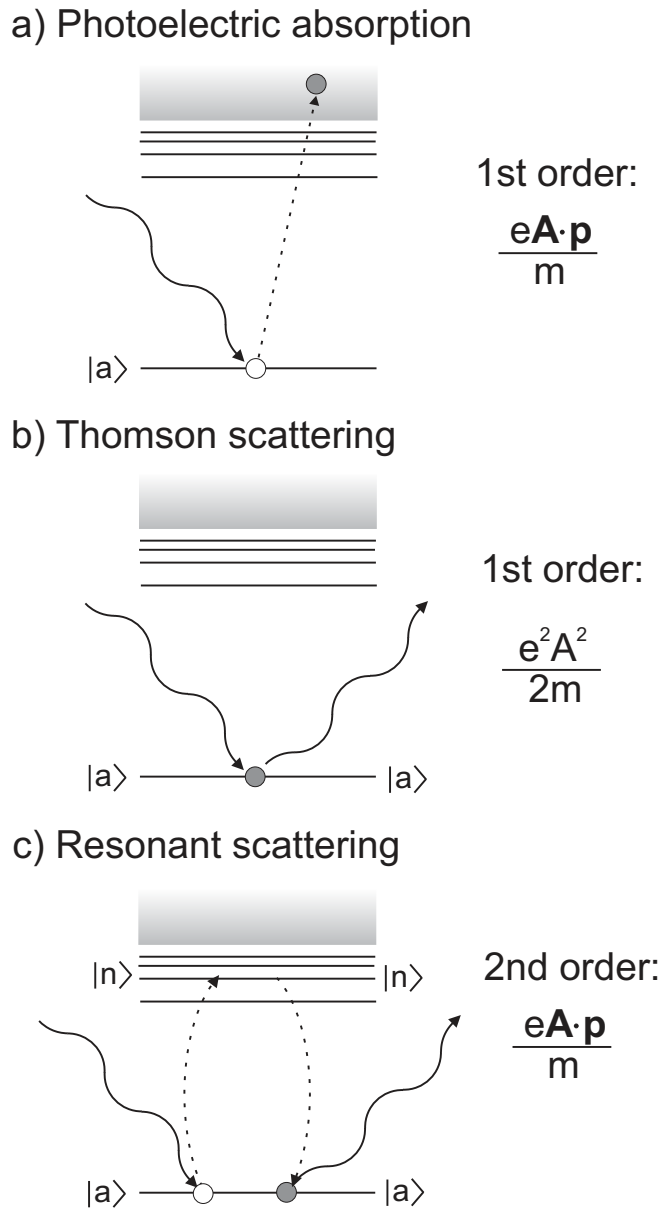
a) Photoelectric absorption

1st order:

$$\frac{e\mathbf{A}\cdot\mathbf{p}}{m}$$

$|a\rangle$

b) Thomson scattering

1st order:

$$\frac{e^2A^2}{2m}$$

$|a\rangle$ $|a\rangle$

c) Resonant scattering

$|n\rangle$ $|n\rangle$

2nd order:

$$\frac{e\mathbf{A}\cdot\mathbf{p}}{m}$$

$|a\rangle$ $|a\rangle$

Figure 5.3.: Quantum mechanical description of the interaction of a photon with an atomic electron. Photoelectric absorption (a) and Thomson scattering (b) can be explained by applying first order perturbation theory. Resonant scattering (c) is a second order process and occurs via an intermediate state. Fig. taken from Ref. [166].

terms in the interaction Hamiltonian only contribute to non-resonant magnetic scattering, which is beyond the scope of this thesis. The vector potential $\mathbf{A}$ of the photon field is linear in photon creation and annihilation operators. $\mathcal{H}_1$ again is linear in $\mathbf{A}$, and it follows that it can either create or destroy a photon, but not both. In first order, this term gives rise to photoelectric absorption, depicted in Fig. 5.3(a). $\mathcal{H}_2$ is quadratic in

A and can first destroy and then create a photon, while leaving the electron in the same state. This term therefore describes elastic Thomson scattering (Fig. 5.3(b)). Resonant scattering processes stem from second order perturbation theory of $\mathcal{H}_1$ (Fig. 5.3(c)). In the following sections absorption and resonant scattering are discussed in more detail.

5.1.1. Absorption

The absorption cross section σ_a is defined as the transition rate probability divided by the incident flux $\Phi_0 = c/V$

$$\sigma_a = \frac{w_{i \to f}}{\Phi_0}. \tag{5.2}$$

Since the photoelectric absorption is described by the Hamiltonian $\mathcal{H}_1$, the transition rate probability $w_{i \to f}$ to first order perturbation theory can be derived as:

$$w_{i \to f} = \frac{2\pi}{\hbar} \int dE_f \, |\langle f|\mathcal{H}_1|i\rangle|^2 \, \rho(E_f) \delta(E_f - E_i - \hbar\omega), \tag{5.3}$$

where $\rho(E_f)$ is the density of final states. The initial and final states are given by

$$|i\rangle = |i\rangle_{\text{el}} |\mathbf{k}_i, \sigma\rangle_{\text{ph}}, \quad |f\rangle = |f\rangle_{\text{el}} |0\rangle_{\text{ph}}. \tag{5.4}$$

The two different polarization states are denoted by $\sigma = 1, 2$ and $\mathbf{k}$ is the wavevector of the photon.

If only dipole transitions are considered, which is sufficient for the $2p \to 3d$ excitations of $3d$ transition metals, the absorption cross section results in

$$\sigma_a = \frac{4\pi^2 e^2}{\hbar c} \hbar\omega \, |\langle f|\epsilon \cdot \mathbf{r}|i\rangle|^2 \, \rho(E_f = E_i + \hbar\omega), \tag{5.5}$$

where ϵ is the polarization vector of the electromagnetic wave.

As can be seen from Eq. 5.5 the absorption cross-section is proportional to the density of final states ρ, which in a magnetic material is different for the two electron spin states. An evaluation of the transition matrix elements of $(\epsilon \cdot \mathbf{r})$ reveals that the probability to excite a spin-up or spin-down electron at the $L_{2,3}$ edge, respectively, is dependent on the polarization state of the incoming light. Right circularly polarized photons excite mainly spin-up core electrons at the L_3 edge and spin-down electrons at the L_2 edge. For left circularly polarized light the situation is vice versa. The spin-orbit splitting is a prerequisite for the spin polarization of the core electrons, since the sum of the electrons excited at the L_2 and L_3 edges shows no spin polarization for a given helicity.

Thus, XMCD can be explained in a two-step model: First, the excited electrons become

spin polarized depending on the photon helicity due to the spin-orbit splitting. Second, the unoccupied final states serve as a spin detector (see Fig. 5.2).

5.1.2. Resonant Scattering

Phenomenologically the x-ray scattering amplitude of an atom can be written in the form

$$f(\mathbf{Q}, \omega) = f^0(\mathbf{Q}) + f'(\omega) + i f''(\omega), \tag{5.6}$$

where $f^0(\mathbf{Q})$ is the atomic form factor, i.e. the Fourier transform of the charge distribution and f', f'' are the real and imaginary parts of the dispersion corrections. They are energy dependent and take their extremal values at the absorption edges. Since the dispersion corrections are usually dominated by electrons in the K or L shell, where the electrons are spatially confined, the $\mathbf{Q}$ dependence can be neglected. The Thomson term f^0, on the other hand, depends on the scattering vector. However, at the $2p$ edges of $3d$ metals the scattering vector is small compared to the atomic radius, which leads to the approximation $f^0(\mathbf{Q} = 0) = Z$, where Z is the atomic charge number.

To obtain resonant scattering terms it is necessary to calculate the cross-section in second order perturbation theory. The differential cross section is related to the scattering amplitude by the definition (see Sec. 4.1)

$$\frac{d\sigma}{d\Omega} = |f(\mathbf{Q}, \omega)|^2 . \tag{5.7}$$

Applying perturbation theory yields

$$f(\mathbf{Q}, \omega) = \frac{V\omega}{2\pi\hbar c^2} \left(\langle f|\mathcal{H}_2|i\rangle + \sum_n \frac{\langle f|\mathcal{H}_1|n\rangle\langle n|\mathcal{H}_1|i\rangle}{E_i - E_n + \hbar\omega} \right), \tag{5.8}$$

where the sum is over all possible states with energy E_n. The first term in Eq. 5.8 describes the non-resonant Thomson scattering from all electrons in the atom, whereas the second term is responsible for the resonant scattering. The matrix element in the numerator can be interpreted in the following way: the incident photon is first destroyed, and the electron makes a transition to an intermediate state $|n>$. In an elastic scattering event the electron then creates a photon and falls back to the ground state $|a>$ (see Fig. 5.3(c)). When the energy of the incident photon is equal to the difference in energy between the intermediate and ground states, $\hbar\omega = E_n - E_i$, resonant behavior occurs.

If only dipole transitions are considered (for multipole transitions see [20]), the total

elastic x-ray scattering factor can be written as:

$$f = \underbrace{(\epsilon_f^* \cdot \epsilon_i)(-r_e Z + F^{(0)})}_{f_1} + \underbrace{i(\epsilon_f^* \times \epsilon_i) \cdot \mathbf{m} F^{(1)}}_{f_2} + \underbrace{(\epsilon_f^* \cdot \mathbf{m})(\epsilon_i \cdot \mathbf{m}) F^{(2)}}_{f_3}, \qquad (5.9)$$

with

$$F^{(0)} = \frac{3\lambda}{8\pi} \left[F_{-1}^1 + F_1^1 \right], \qquad (5.10)$$

$$F^{(1)} = \frac{3\lambda}{8\pi} \left[F_{-1}^1 - F_1^1 \right], \qquad (5.11)$$

$$F^{(2)} = \frac{3\lambda}{8\pi} \left[2F_0^1 - F_{-1}^1 - F_1^1 \right]. \qquad (5.12)$$

The unit vector $\mathbf{m}$ is pointing along the direction of the local magnetic moment, which defines the quantization axis of the system. The functions $F^{0,1,2}$ are strongly energy dependent resonant strengths for the dipole transitions. The first term in Eq. 5.9 refers to non-resonant and resonant charge scattering. The second term is first order in the magnetization and yields a circular dichroic signal, whereas the third term is second order in the magnetization causing linear dichroism.

Polarization Dependence

In this section the resonant scattering amplitude f for different polarization states of the incoming light will be briefly discussed. First, linear polarized light is considered. Usefully, the polarization is chosen either parallel (ϵ_π) or perpendicular (ϵ_σ) to the scattering plane (see Fig. 5.4). The first term in Eq. 5.9 is similar to Thomson scattering
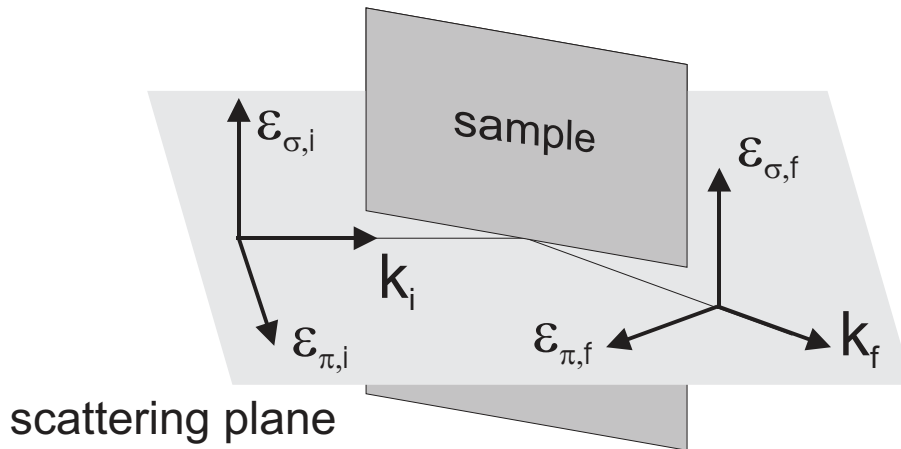

Figure 5.4.: Definition of the polarization vectors.

and conserves the initial photon polarization. While for $\sigma \to \sigma$ scattering f_1 is constant, $\pi \to \pi$ scattering is dependent on the scattering angles. The second term f_2 is sensitive to ferromagnetism and allows for a change of the polarization state. The intensity of $\sigma \to \pi$ and $\pi \to \sigma$ scattering is quadratic in $\mathbf{m}$, noting that the differential cross-section is proportional to the absolute square of the scattering amplitude. Since $\sigma \to \sigma$ scattering is forbidden, only the charge-magnetic interference term of the $\pi \to \pi$ scattering contains a contribution linear in $\mathbf{m}$. This geometry corresponds to the T-MOKE and is sensitive to in-plane magnetization perpendicular to the scattering plane. The third term f_3 is neglected here, since its contribution to XRMS is generally supposed to be small [170].

The XRMS experiments performed within the framework of this thesis used the L-MOKE geometry, where the magnetization lies along the sample surface within the scattering plane. To probe this magnetization, circular polarized light is needed. The polarization vectors can be written as a linear combination of ϵ_π and ϵ_σ

$$\epsilon_\pm = \mp \frac{1}{\sqrt{2}} \left(\epsilon_\sigma \pm i \epsilon_\pi \right), \tag{5.13}$$

where the positive sign indicates right circular polarization. The polarization state of the circular polarized light is not changed by scattering. Similar to the T-MOKE geometry, the charge-magnetic term causes the dominant magnetic contribution to the scattering.

In general the relations between incoming polarization and magnetization direction are not definite. For vector magnetometry measurements comparable to PNR measurements an analysis of the outgoing light would be necessary, which is technically demanding.

5.2. Scattering and Refraction

Similar to the case of neutron scattering, the refractive index is related to the scattering factor through [171]

$$1 - n(\omega) = \frac{r_e \lambda^2}{2\pi} \sum_i \rho_i f_i(\omega, Q = 0), \tag{5.14}$$

where ρ_i is the number density of species i in the sample and $f_i(\omega, Q = 0)$ is the corresponding scattering amplitude in the forward direction $\mathbf{k}_i = \mathbf{k}_f$. It can be shown that the classical optical approach and the quantum mechanical description are equivalent with respect to the dipolar transitions [170]. However, for the simulation of specular reflectivity from ferromagnetic multilayer systems an algorithm based on magneto-optics is more convenient, since it allows for the application of a standard dynamical approach. The required refractive index of a material can completely be inferred by an absorption

experiment.

According to the optical theorem, the imaginary part β of the complex refractive index is directly proportional to the absorption coefficient μ,

$$\beta_\pm = \mu_\pm/(2k), \tag{5.15}$$

where k is the photon wavevector and the index refers to positive ($+$) or negative ($-$) circular polarization. The refractive index is commonly split into real and imaginary part according to

$$n_\pm = 1 - \delta_\pm + i\beta_\pm = 1 - (\delta \pm \Delta\delta/2) + i(\beta \pm \Delta\beta/2), \tag{5.16}$$

where δ and β are the dispersive and absorptive contributions, respectively, and $\Delta\delta$ and $\Delta\beta$ are the corresponding magnetic contributions to the refractive index. If the energy dependence of β is known, the modified Kramers-Kronig relations

$$\delta_+(E) + \delta_-(E) = -\frac{2}{\pi}\mathcal{P}\int_0^\infty E' \frac{\beta_+(E') + \beta_-(E')}{E'^2 - E^2} dE', \tag{5.17}$$

$$\delta_+(E) - \delta_-(E) = -\frac{2E}{\pi}\mathcal{P}\int_0^\infty \frac{\beta_+(E') - \beta_-(E')}{E'^2 - E^2} dE', \tag{5.18}$$

can yield the dispersive contribution δ to the refractive index. $\mathcal{P}$ denotes the principal value [166].

One important implication of the Kramers-Kronig relations should be noted: The optical theorem rewritten as

$$\sigma_a = \frac{4\pi r_e}{k} f''(\mathbf{Q} = 0) \tag{5.19}$$

states that the absorption cross-section σ_a is proportional to the imaginary part of the atomic scattering length f'' in the forward direction. Since the scattering length is related to the refractive index, its real part f' can be derived by applying the Kramers-Kronig relations, if f'' is known. Hence the resonant magnetic scattering can be viewed as being caused by magnetization dependent absorption or the other way round [167].

5.3. Specular Reflectivity

X-ray resonant magnetic scattering (XRMS) allows for the determination of element-specific chemical and magnetic depth profiles of layered structures [172, 173, 174]. These profiles can be obtained by a quantitative analysis of specular reflectivity measurements,
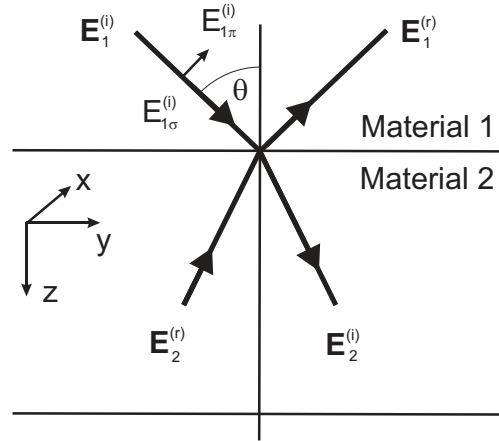
Figure 5.5.: Refraction by a single boundary of two media. E_π and E_ρ are the electric-field components parallel and perpendicular to the plane of incidence. Figure taken from Ref. [178].

usually performed by numerical simulation. The calculation of the reflectivity needs a dynamical approach, since total and multiple reflection effects cannot be neglected. Lee et al. have given a theoretical formulation of x-ray resonant magnetic scattering [175, 176] from rough surfaces and interfaces within the distorted-wave Born approximation. A matrix based formalism for magneto-optics with arbitrary magnetization direction has been developed by Zak et al. [177, 178, 179]. It offers the possibility to calculate the specular reflectivity without any restrictions to the geometry, i.e. the magnetization direction, angle of incidence and polarization. The basic ideas to derive the expressions for calculating magneto-optic coefficients for a general configuration of the magnetization in a multilayer system shall briefly be presented here, following the paper by Zak et al. However, one restriction is made for simplicity: since the multilayers studied within this thesis exhibit an in-plane magnetization only, the direction of the magnetization is confined to lie parallel to the surface.

First, two media separated by a single boundary, i.e. the xy-plane (see Fig. 5.5) are assumed. The incoming and reflected electromagnetic wave is described in a basis of polarization states perpendicular (E_σ) and parallel (E_π) to the plane of incidence. These fields can be collected in a four-component vector

$$\mathbf{P} = \begin{pmatrix} E_\sigma^{(i)} \\ E_\pi^{(i)} \\ E_\sigma^{(r)} \\ E_\pi^{(r)} \end{pmatrix}, \tag{5.20}$$

where i and r denote the incident and reflected wave, respectively. According to Maxwell's equations, the tangential components of the electric and magnetic field are conserved, when a electromagnetic wave travels from medium 1 into medium 2. Thus it is useful to change the basis

$$\mathbf{F} = \begin{pmatrix} E_x \\ E_y \\ H_x \\ H_y \end{pmatrix}. \tag{5.21}$$

Now a so-called medium boundary matrix can be defined by the expression

$$\mathbf{F} = A\mathbf{P}. \tag{5.22}$$

Having the matrix A, it becomes simple to write down the boundary matching conditions for a two-media problem:

$$A_1\mathbf{P}_1 = A_2\mathbf{P}_2. \tag{5.23}$$

This is a set of four linear equations with the unknowns $E_{1\sigma}^{(r)}, E_{1\pi}^{(r)}, E_{2\sigma}^{(i)}, E_{2\pi}^{(i)}$ $(E_{2\sigma}^{(r)} = E_{2\pi}^{(r)} = 0)$ (see Fig. 5.5). The medium boundary matrix therefore solves the problem for a single boundary.

For the calculation of A, the connection between the vectors $\mathbf{F}$ and $\mathbf{P}$ has to be found.

The in-plane direction of the magnetization $\mathbf{M}$ is specified by means of the polar angle γ:

$$M_x = M\cos\gamma, \tag{5.24}$$

$$M_y = M\sin\gamma. \tag{5.25}$$

With these definitions the dielectric tensor ϵ yields

$$\epsilon(\omega) = N^2 \begin{pmatrix} 1 & 0 & -i\sin\gamma Q \\ 0 & 1 & i\cos\gamma Q \\ i\sin\gamma Q & -i\cos\gamma Q & 1 \end{pmatrix}. \tag{5.26}$$

Here the charge and magnetic contribution to the complex refractive index are given by $N = 1 - \delta + i\beta$ and $Q = -\Delta\delta + i\Delta\beta$, respectively. Q is the so-called Voigt parameter. Using Snell's law and Maxwell's material equation $\mathbf{D} = \epsilon\mathbf{E}$ the relations between the components of the electric field vector $\mathbf{E}$ in the magnetic medium can be derived and finally the medium boundary matrix A can be calculated.

In a multilayer system there is more than one boundary, thus one also needs to know

the wave propagation inside the medium. This is given by the medium propagation matrix $\bar{D}$, which describes the phase shift and absorption during propagation in the layer. The boundary matching conditions for the multilayer system can now be expressed in the form

$$\mathbf{P}_i = M\mathbf{P}_f, \tag{5.27}$$

with

$$M = A_i^{-1} \prod_{m=1}^{l} (A_m \bar{D}_m A_m^{-1}) A_f. \tag{5.28}$$

The light starts out in the initial medium i, goes through the multilayer system and ends up in the substrate or final medium f. With the knowledge of the refractive index, Voigt parameter, magnetization direction and angle of incidence, the matrix M can be calculated and as a result the reflected and transmitted intensities are determined.

Grabis [180] has written a computer code based on this Zak formalism, which was used for the quantitative analysis of the XRMS data within this thesis. Structural and magnetic roughness have been taken into account in terms of graded electron density and magnetization profiles using a slicing method.

5.4. X-ray Resonant Magnetic Diffuse Scattering

Similar to the case of non-magnetic off-specular scattering, it is possible to study the off-specular magnetic scattering and derive information about the correlation of the magnetic roughness [176, 181, 182, 183].

The experiments within the framework of this thesis have been performed in L-MOKE geometry, where the intensity difference of left and right circular polarized light is measured. Since the scattered intensity in L-MOKE geometry using circularly polarized light is proportional to the charge-magnetic interference term (as discussed in Sec. 5.1.2) this difference contains both charge and magnetic contributions [184], which cannot be separated.

The diffuse intensity difference in the L-MOKE geometry using circular polarization shall be discussed here within the kinematical limit, i.e. in Born approximation [181, 183]. This is sufficient, since in the soft x-ray range, the scattering angles are large compared to the critical angle. The derivation is completely analogous to the case of off-specular neutron scattering (Sec. 4.4). The point of departure is a single magnetic surface. The differential cross-section is yielded by inserting the resonant scattering amplitude f (Eq. (5.9)) into Eq. (4.66). The charge and magnetic volume are considered separately, each having its own roughness. The cross-section can be divided into a pure

charge term, a pure magnetic term and a charge-magnetic interference term, which is the only term being sensitive to a reversal of the helicity. The further derivation goes along the approach in Sec. 4.4 and finally one gets the generalized result for the difference in diffuse intensity of left and right circularly polarized light by a magnetic multilayer:

$$\Delta\left(\frac{d\sigma}{d\Omega}\right)_{\text{diffuse}} = P_c \frac{L_x L_y}{Q_z^2} \left[\mathbf{k}_f \cdot \mathbf{m} + \cos(\alpha + \beta)\mathbf{k}_i \cdot \mathbf{m}\right] \times \quad (5.29)$$

$$\sum_{i,j}^{N} \left[\Delta\rho_{ij}^{em} e^{iQ_z(z_i - z_j)} e^{-Q_z^2(\sigma_{e,i}^2 + \sigma_{m,j}^2)/2} S_{ij}^{em}(\mathbf{Q}) + \Delta\rho_{ij}^{em*} e^{iQ_z(z_i - z_j)} e^{-Q_z^2(\sigma_{e,j}^2 + \sigma_{m,i}^2)/2} S_{ji}^{em}(\mathbf{Q})\right], \quad (5.30)$$

with

$$S_{ij}^{em}(\mathbf{Q}) = \int_S dX\,dY \left(e^{Q_z^2 C_{ij}^{em}(X,Y)} - 1\right) e^{i(Q_x X + Q_y Y)}, \quad (5.31)$$

where $C_{ij}^{em}(X,Y)$ is the height-height correlation function of the structural interface i and the magnetic interface j. This function is identical to Eq. (4.67), but ξ and h depend on charge-magnetic correlations. The heights of the structural and magnetic surfaces above the xy plane are given by the functions $z_e(x,y)$ and $z_m(x,y)$. The function

$$\Delta\rho_{ij}^{em} = \Delta\left\{N_e(-Zr_0) + N_r \frac{3\lambda}{8\pi}\left[F_{-1}^1 + F_1^1\right]^*\right\}_i \Delta\left\{N_r \frac{3\lambda}{8\pi}\left[F_{-1}^1 - F_1^1\right]\right\}_j, \quad (5.32)$$

displays the difference in the charge scattering amplitude across the i-th interface times the difference in the magnetic scattering across the j-th interface. The factor in front of the sum in Eq. (5.29) contains the amount of circular polarization P_c and the geometrical dependence of the angle of incidence and reflection. Due to the product $\mathbf{k}_{i,f} \cdot \mathbf{m}$ the magnetic sensitivity is confined to magnetic moments in the scattering plane. Out-of-plane magnetic moments contribute only for large scattering angles.

The magnetic contribution to the off-specular scattering can be caused by different mechanism. One can distinguish between a magnetic interface roughness correlated to the structural roughness and magnetic roughness caused by magnetic domains in the ferromagnetic layer. This point is further discussed in Chap. 7.

5.5. Experimental Setup

The soft XRMS experiments were performed using the diffractometer ALICE [185] at the undulator beamlines UE56/1-PGM and UE56/2-PGM2 at BESSY II. Due to strong air absorption of x-rays in the energy range considered (600-900 eV), XRMS experi-
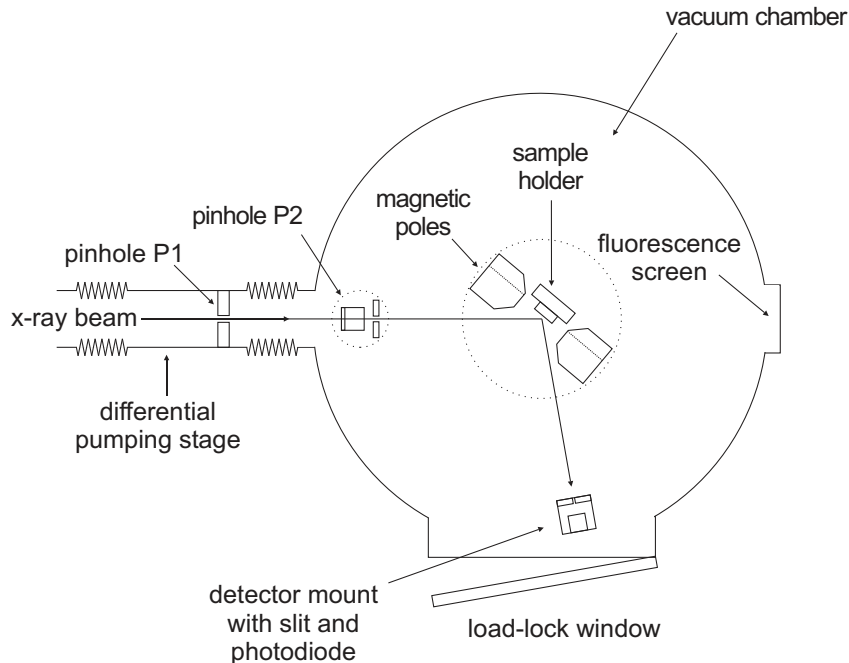
Figure 5.6.: Schematic topview of the diffractometer.

ments have to be carried out in vacuum. Therefore, a two-circle goniometer working in horizontal scattering geometry has been installed in a vacuum chamber (see Fig. 5.6). At synchrotron sources a vacuum of typically $< 5 \times 10^{-9}$ mbar is required to ensure a ultrahigh vacuum environment of the beamline optics and the storage ring. To fulfill this condition, a differential pumping stage, consisting of a pinhole P1 and a turbomolecular pump, is installed between the chamber and the beamline. After the beam of light has passed a collimating entrance slit of 300 μm it impinges on the sample. The scattered beam is detected by a photodiode, creating a photocurrent, which is measured with an electrometer. The size of the slit in front of the detector is likewise set to 300 μm, resulting in an instrument resolution of 0.14°. For the measurements circularly polarized light produced by undulators was used with an energy resolution of approximately $\Delta E/E = 1 \cdot 10^{-4}$. A magnetic field can be applied in the scattering plane along the sample surface either parallel or antiparallel to the photon helicity, which corresponds to the longitudinal magneto-optical Kerr effect (L-MOKE) geometry. The maximum field which can be reached is ± 0.27 T. The magnetic contribution to the scattered intensity was always measured by switching the magnetic field at fixed photon helicity, which is equivalent to the switch of the helicity at fixed magnetic field. A He closed-cycle cryostat allows to reach a sample temperature in the range of 30-500 K.

Part III.

Results and Discussion

6. Single Co$_2$MnGe Thin Films

In order to find out the optimal parameters for high-quality structural growth and to control the magnetic properties of Heusler based superlattices, extensive preliminary studies on Co$_2$MnGe single films are necessary. Here we present a study of the structural and magnetic properties of single Co$_2$MnGe layers using x-ray scattering experiments and magnetometry measurements. XMCD is used to probe the element specific magnetic moments. Furthermore this method allows to determine the spin and orbital moment of Co and Mn separately.

6.1. Sample Preparation

All films of the present study were grown by rf-sputtering with a dual source HV sputtering equipment on single crystalline Al$_2$O$_3$ (11-20) surfaces (sapphire a-plane). The base pressure of the system was 5×10^{-8} mbar after cooling of the liquid nitrogen cold trap. We used pure Ar at a pressure of 5×10^{-3} mbar as sputter gas, the target was prepared from a stoichiometric alloy of the Heusler phase. The sputtering rates during the thin film preparation were 0.04 nm/s for the Co$_2$MnGe phase, the V seed layers were deposited at a sputtering rate of 0.03 nm/s. The sapphire substrates were cleaned chemically and ultrasonically after cutting. Immediately before the deposition they were additionally etched by an ion beam for 300 s in order to remove any residual surface contaminations.

There are two conditions to achieve good structural and magnetic quality of the Heusler layers. First, the substrate temperature must be high, in our optimized procedure the substrate temperature was 500°C. Second, seed layers of a simple metal with a good lattice matching to the Heusler compounds are important to induce epitaxial or textured growth with a flat surface. Growing the films directly on sapphire results in polycrystalline films and surface roughening. We have tested different possible seed layers such as Cr, Nb, Ag and Au. Here we concentrate on V which gave good structural results [186, 187] and has been used as interlayer for the multilayers discussed in the next chapter. The surfaces of the Heusler compounds oxidize rapidly and must be covered
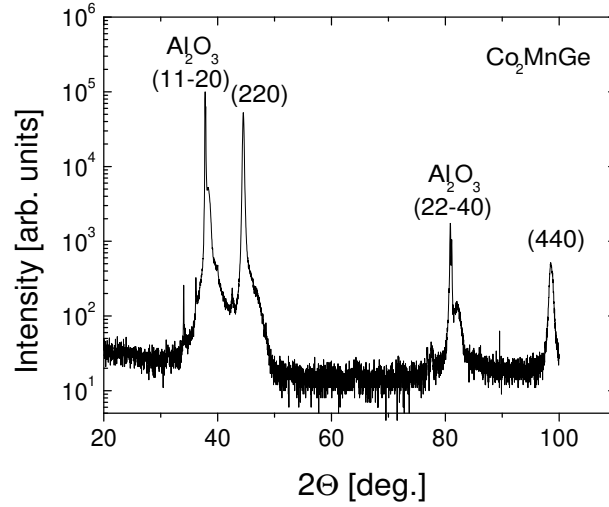
Figure 6.1.: Out-of-plane Bragg scan of a V(3nm)/Co$_2$MnGe(100nm) film measured with Cu K_α radiation.

by a protection layer before being exposed to air. If nothing else is stated, we use an amorphous Al$_2$O$_3$ film of 2 nm thickness as a cap layer.

6.2. Structural Properties

phase	lattice parameter [nm]		sat. magnetization $[\frac{emu}{g}]$		sat. moment $[\mu_B]$
	bulk	film	bulk	film	film
Co$_2$MnGe	0.5743	0.575	111	114	5.02

Table 6.1.: Lattice parameters, saturation magnetization and saturation magnetic moments (per formula unit) of the pure, thick Heusler films in comparison to the bulk values. The bulk values have been taken from Ref. [22].

The structural quality of the films was characterized by hard x-ray scattering using a Cu K_α rotating-anode x-ray tube. Figure 6.1 shows an out-of-plane x-ray Bragg scan of a 100 nm thick Co$_2$MnGe film with a 5 nm V seed layer. Only the (220)- and the (440)-Bragg peaks of the Heusler phase are observed, proving perfect (110)-texture out-of-plane. Rocking scans at grazing incidence revealed that the films are polycrystalline in-plane. Table 6.1 summarizes the relevant structural data derived from the x-ray scans. The lattice parameters virtually coincide with those of the bulk phase, the half width of the rocking curve (width in 2Θ at half maximum) characterizing the mosaicity
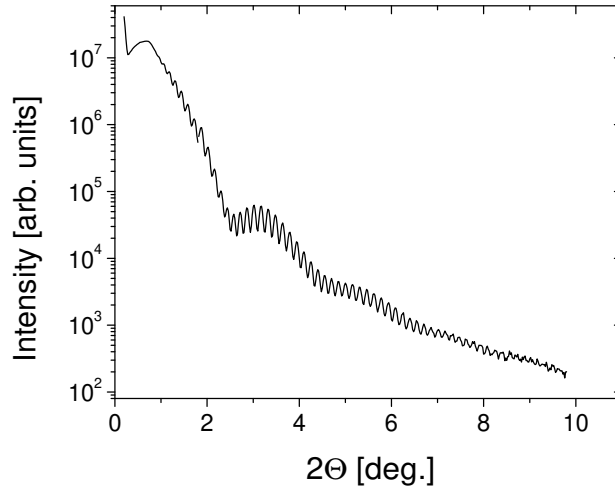
Figure 6.2.: X-ray reflectivity scan of the sample V(4nm)/Co$_2$MnGe(60nm), measured with a standard Cu K_α rotating-anode x-ray tube.

of the crystallite is 0.8° for the Co$_2$MnGe phase. The half width of the Bragg peaks corresponds to the experimental resolution of the spectrometer. An example of an x-ray reflectivity scan for a Co$_2$MnGe film is shown in Fig. 6.2. Total thickness oscillations are observed up to $2\Theta = 10°$, pointing out a very flat surface morphology. A simulation of the curve with the Parratt formalism gives a typical rms roughness for the film surface of about 0.3 nm. This is corroborated by atomic force microscopic (AFM) pictures of the surface which reveal a very smooth surface morphology. We also have grown films at lower preparation temperatures down to a substrate temperature $T_{sub} = 100°$C. The structure of films prepared below $T_s = 500°$C is still perfect (110)-texture, however with a rocking width slightly increasing with decreasing preparation temperature.

Since for the multilayers discussed in the next chapter the typical layer thickness of the Heusler layers is of the order of 3 nm only and T_s is limited to 300°C in order to avoid strong interdiffusion at the interfaces, the structural and magnetic properties of single very thin Heusler layers prepared under the same conditions have been studied. Fig. 6.3 shows an out-of-plane Bragg scan of a trilayer V(5nm)/Co$_2$MnGe(4nm)/V(5nm). One observes a very broad (220)-Bragg peak with a half width of $\Delta 2\Theta = 2°$ at $2\Theta = 43°$ from the Co$_2$MnGe phase. Using the Scherrer formula [188] for the Bragg reflection of small particles, which correlates the coherence length L_c of the particles with the half width of the Bragg peaks

$$L_c = 0.89\lambda/[\Delta(2\Theta) \cdot \cos(\Theta)], \tag{6.1}$$
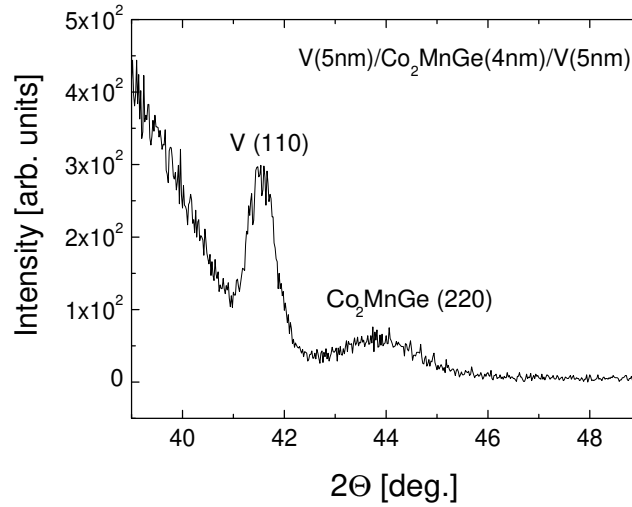
Figure 6.3.: Out-of-plane Bragg scan of a V(5nm)/Co₂MnGe(4nm)/V(5nm) trilayer.

we derive $L_c = 3$ nm. This is an indication that the mean size of the crystalline grains in the film is slightly smaller than the film thickness.

6.3. Magnetic Properties

The dc magnetization of our films was studied by a commercial superconducting quantum interference device (SQUID) based magnetometer (Quantum Design MPMS system). Examples of magnetic hysteresis loops of the Co₂MnGe films are presented in Fig. 6.4. The films possess a growth induced weak, uniaxial anisotropy with an anisotropy field H_K of about 50 Oe. For the measurements in Fig. 6.4 the external field axis was directed parallel to the magnetic easy axis, thus the hysteresis loops are rectangular. The coercive field for the Co₂MnGe phase is $H_c = 20$ Oe at room temperature. The saturation magnetization at 5 K is in good agreement with the values measured in bulk samples within the experimental error bars (see Tab. 6.1). The saturation magnetic moment per formula unit calculated from the saturation magnetization is 5.02 μ_B for Co₂MnGe. These values agree with those derived from the theoretical band structure calculations for perfect $L2_1$ type of order [7], indicating that the films have a high degree of metallurgical order. Thus to this end things look positive, thick films of the Heusler phase Co₂MnGe can be grown at high temperatures with a quality similar to bulk samples.

However, when decreasing the substrate temperature while keeping the thickness of
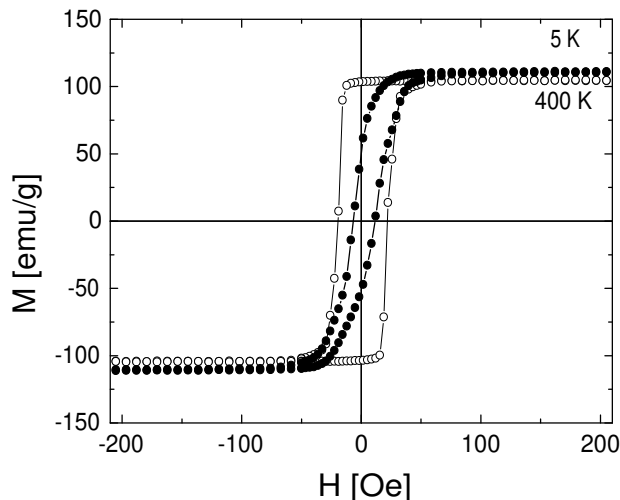
Figure 6.4.: Hysteresis loops of the Co₂MnGe film from Fig. 6.1 measured at 5 K and 400 K.

the Co₂MnGe layer and all other parameters constant, we observed a continuous decrease of the saturation magnetization down to about 70% at $T_s = 100°C$ (see Fig. 6.5). This decrease of the magnetization is accompanied by an increase of the lattice parameter of about 1%. It seems plausible to attribute the decrease of the saturation magnetization to an increasing number of antisite defects in the $L2_1$ structure. This effect is well known in Cu₂MnAl, where the disordered $B2$ phase, which can be prepared by quenching from high temperatures, has a very low saturation magnetization [189]. For films with a small thickness of the Heusler phase of the order of a few nm the situation gets even worse. In this case a preparation at 500°C is prohibited, since then interdiffusion at the seed layer/Heusler interface is too strong. A practical limit for the substrate temperature for avoiding excessive diffusion is 300°C. As a first example of a very thin film Fig. 6.6 depicts the hysteresis loop measured at 5 K of a 4 nm thick Co₂MnGe film grown directly on sapphire a-plane at $T_s = 300°C$. The x-ray structural analysis showed no resolvable Bragg peak, thus the crystalline structure seems to be polycrystalline with very small grains. The film has a very low saturation magnetization of only about 10% of the bulk value, showing that the ferromagnetic properties are completely different from those of the Co₂MnGe phase in the $L2_1$ structure. Growing the same film thickness for Co₂MnGe on a V seedlayer, a (220)-Bragg peak can be observed (see Fig. 6.3) and about 50% of the ferromagnetic saturation magnetization of the Co₂MnGe phase is recovered (Fig. 6.7(a)). The magnetization is isotropic in the film plane with a magnetic remanence of only about 30% of the saturation magnetization.
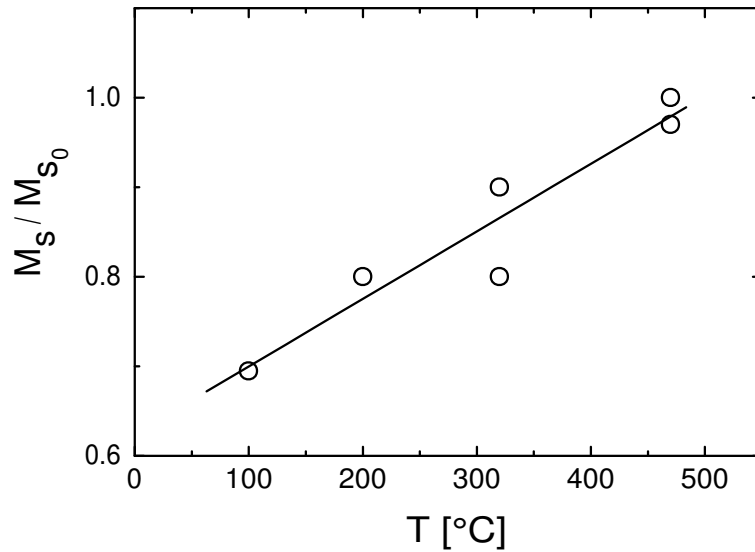
Figure 6.5.: Saturation magnetization of a Co$_2$MnGe(100nm) film versus the substrate temperature during preparation.

Interestingly, for the field direction perpendicular to the film plane (Fig. 6.7(b)) the hysteresis curves are very similar to those observed in a parallel field, thus the strong anisotropy of the demagnetising field characterizing a homogeneous magnetic thin film is absent. This clearly shows that the magnetization of the film in Fig. 6.7 is not homogeneous, but breaks up into weakly coupled small magnetic particles pointing in
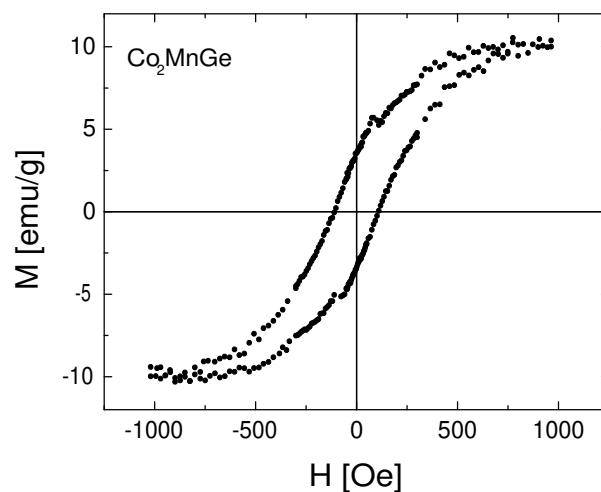
Figure 6.6.: Hysteresis loop of a 4 nm thick Co$_2$MnGe film grown directly on sapphire a-plane at a substrate temperature of 300°C measured at 5 K.
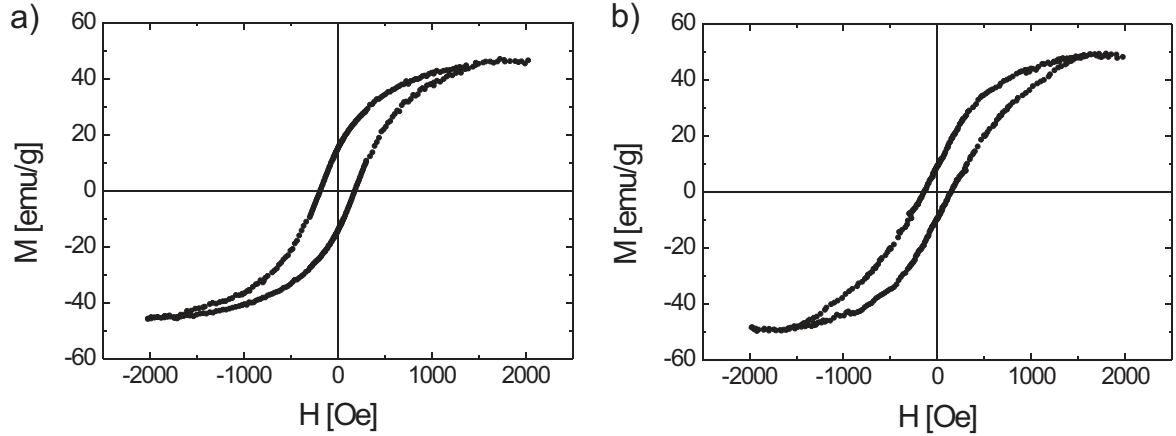
Figure 6.7.: Hysteresis loops of the sample V(3nm)/Co$_2$MnGe(4nm)/V(3nm) measured at 5 K with the field applied parallel to the sample plane (a) and perpendicular to the sample plane (b).

their own magnetically easy direction given by the geometrical shape and the crystal magnetic anisotropy. Further measurements revealed that for a 4 nm thick Co$_2$MnGe film grown on Au as seed layer the small particle character of the hysteresis loops also exists, but the magnetic anisotropy of a homogenous thin film is partly recovered. In this case the ferromagnetic saturation magnetization is also strongly reduced compared to the bulk value of Co$_2$MnGe. The different magnetic behaviour of Co$_2$MnGe grown on V and Au is probably caused by much smaller crystalline grains in the case of a V seed layer, where the single grains seem to be nearly decoupled magnetically.

6.4. XMCD

In order to elucidate the microscopic origin of the moment reduction in the Co$_2$MnGe Heusler alloy when prepared at low substrate temperatures (see Fig. 6.5) x-ray magnetic circular dichroism (XMCD) is a very suitable experimental method as it allows an element specific study of the magnetism [190]. We therefore prepared a Co$_2$MnGe film specially designed for an XMCD study with 16 nm thickness grown on a V seed layer and with a 2 nm Au cap layer. This is essential for the analysis below, since XMCD measured in total electron yield (TEY) mode probes a surface layer of a few nanometer total thickness only and thus is rather surface sensitive. All layers of the sample were prepared at $T_s = 300°$C. The saturation magnetization of the film, as measured by SQUID magnetometry, is found to be slightly smaller than the value given in Fig. 6.5, it corresponds to a magnetic moment per formula unit of 2.3 μ_B at room temperature and 2.98 μ_B at 4 K. Hard x-ray reflectivity measurements reveal smooth surfaces and

interfaces of the film, a fit with the Parratt formalism gives the roughness parameters $\sigma = 0.18$ nm and 0.33 nm for the Au and Co_2MnGe layer, respectively.

The XMCD measurements were performed at the bending magnet beamline PM3 at BESSY II (Berlin Germany) using the ALICE diffractometer [185]. The measurements were taken by the total electron yield (TEY) method, i.e. by measuring the sample drain current. During the experiment the helicity of the photons was fixed whereas the magnetization of the sample was switched by a magnetic field of ± 0.1 T thus giving the electron yield with the magnetization parallel (Y_+) and antiparallel (Y_-) to the photon helicity. At an angle of incidence of $40°$ saturation effects are small and the TEY is proportional to the absorption coefficient to a good approximation, $Y_\pm \sim \hbar\omega\mu_\pm$. The Y_+ and Y_- scans measured at the $L_{2,3}$ edges of Mn and Co are normalized to the flux of the incoming photon beam. The XMCD spectrum (Y_+-Y_-) at the $L_{2,3}$ edges of Mn and Co measured at room temperature is plotted in Fig. 6.8.

XMCD spectra contain quantitative information on the spin and orbital magnetic moments which can be extracted via the sum rule analysis [164, 165]. There are several sources of systematic errors in this analysis which might affect the derivation of the absolute values for the magnetic moment questionable. This is first the number of holes in the d band, which is inaccessible experimentally, but can precisely be derived by electronic band structure calculations [191]. Second, the magnetic dipolar interactions are not considered in the model, which in our case seems justified because of the cubic
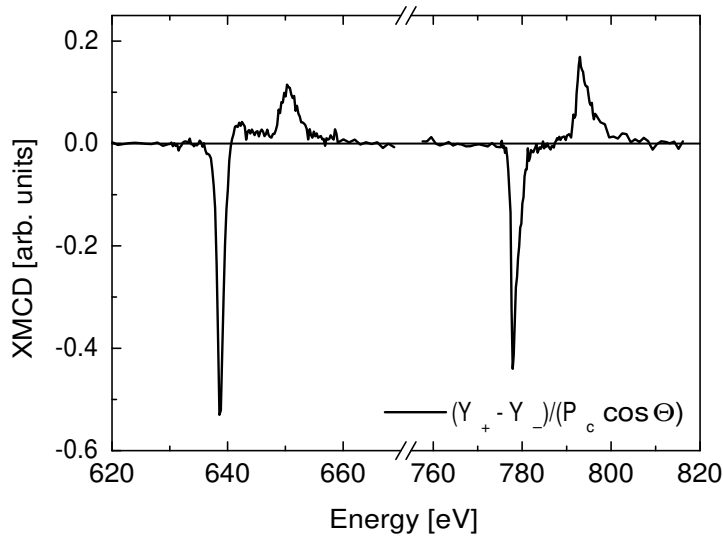

Figure 6.8.: XMCD spectra of a 11 nm thick Co_2MnGe film at the Mn $L_{3,2}$ and at the Co $L_{3,2}$ edge.

symmetry of the Co_2MnGe phase. Third, for the Mn atom there might be a mixing of the L_3 and the L_2 levels by the relatively strong $2p-3d$ Coulomb interactions. The correction factor x taking this effect into consideration has been calculated ranging from $x = 1$ for negligible jj-mixing to $x = 1.5$ for strong jj-mixing [192]. Keeping these reservations in mind, the sum rule analysis yields for the case of the Co atom $m_{spin} = 0.55 \ \mu_B$ for the spin magnetic moment and $m_{orb} = 0.028 \ \mu_B$ for the orbital magnetic moment. For the case of the Mn atom the analysis yields $m_{spin} = 0.98 \ \mu_B$ (1.47 μ_B) and $m_{orb} = 0.056 \ \mu_B$, where for the first value it is assumed that $x = 1.0$ holds, for the value given in brackets $x = 1.5$ is assumed. Summing up all values for the atomic magnetic moments and extrapolating to 4 K we get a saturation magnetic moment of $m = 0.75 \ \mu_B$ for Co and $m = 1.36 \ \mu_B$ (1.97 μ_B) for Mn [193]. The experimental moment for Co is reduced by 20% with respect to the theoretical value from band structure calculations, $m_{Co} = 1.02 \ \mu_B$. For the Mn atom the theoretical calculations give $m = 2.98 \ \mu_B$ i.e. a much higher value than the experiment, irrespective of the exact value of the correction factor x. The magnetization data gave a saturation magnetic moment of 3.6 μ_B per Co_2MnGe formula unit, the XMCD results yield 2.83 μ_B (3.46 μ_B), i.e. within the uncertainty range of the XMCD result the agreement is satisfactory.

As mentioned in Sec. 2.4, the theoretical model calculations [10, 86] show that antisite disorder in the $L2_1$ structure essentially leaves the value of a Co moment unaffected when sitting on a Mn position. We attribute the smaller magnetic moment to the existence of non-ferromagnetic interlayers close to the Au cap layer. Assuming that the rms roughness of 0.33 nm can be identified with the interface thickness and taking into consideration the stronger weight of the surface atoms in the total electron yield method, the observed Co moment reduction seems plausible. The stronger loss of the Mn atomic magnetic moments is probably caused by site disorder in the bulk of the film, i.e. Mn moments sitting on a regular Co position. This strongly reduces the Mn moment, since the Mn atom has its spin antiparallel to the other Co and Mn spins. Thus the plausible hypothesis formulated above that a lower preparation temperatures causes site disorder in the $L2_1$ structure and concomitantly a lowering of the saturation magnetization finds strong support from the XMCD results and the theoretical model calculations. The high degree of site disorder is qualitatively consistent with magnetotransport data revealing small electronic mean free path of the order of 2 nm at 4 K and a strong isotropic spin disorder magnetoresistance [74, 194].

Summarizing this chapter, we have shown that with optimized preparation conditions high-quality thick films of the Co_2MnGe phase can be grown. But if experimental constraints are imposed when preparing devices such as limits for the substrate temperature,

non applicability of seed layers or if in devices very thin Heusler layers are needed, problems arise. Site disorder in the interior of the films, mixing and disorder at interfaces have the tendency to lower the ferromagnetic magnetization. The magnetic behaviour of very small Co_2MnGe grains as e.g. the nearly complete loss of ferromagnetism for Co_2MnGe deposited on bare sapphire or the typical small particle magnetic behaviour in very thin Co_2MnGe grown on V suggest that the grain boundaries are only weakly ferromagnetic or even non-ferromagnetic.

7. [Co$_2$MnGe/V]$_N$ Multilayers

This chapter provides a detailed analysis of the structural and magnetic properties of a series of [Co$_2$MnGe/V]$_N$ multilayers with a thickness of the V layers t_V between 1.5 nm and 10 nm and a fixed thickness of the Heusler layer $t_{Co_2MnGe} = 3$ nm. Conventional x-ray scattering is used to probe the chemical depth profile, while for the derivation of element-sensitive magnetic moment depth profiles energy dependent XRMS measurements are carried out. Neutron reflectivity studies provide a capable tool to search for an antiferromagnetic coupling within the multilayers. The magnetic domain structure of the sample is studied by PNR and off-specular scattering, whereas SQUID measurements are used to determine the total magnetization.

7.1. Sample Preparation

Multilayers of the Heusler phase Co$_2$MnGe with V as interlayer have been prepared by the same dual source rf-sputtering equipment described in Sec. 6. For the multilayer preparation the substrate holder is swept between the two targets of the dual source discharge. After finishing the periods of the multilayer, starting with V as a seed layer, the films were protected by an Al$_2$O$_3$ cap layer. The substrate temperature was held fixed at $T_S = 300$°C for all multilayers, the deposition rates of the materials were the same as given in Chap. 6 for the single layers. Although the structural quality of the Heusler layers improve at higher substrate temperatures, $T_S = 300$°C turned out to be the upper limit, since strong interdiffusion at the interfaces must be avoided [17]. Using the natural gradient of the sputtering rate, the simultaneous preparation of up to 10 samples with the thickness of either the magnetic layer or the non-magnetic layer altered is possible. The thickness can be varied by a factor of three and we exploit this feature for the preparation of a series of multilayers for the investigation of the thickness dependence of the magnetic interlayer coupling. We prepared a series of multilayers with a constant nominal thickness of the Co$_2$MnGe layers $t_{Co_2MnGe} = 3.0$ nm and variable V interlayer thicknesses $t_V = 1.5, 2.0, 2.5, 3.0, 4.0, 5.0$ and 10.0 nm. The number of bilayers was 20 for $t_V = 1.5, 4.0$ and 10.0 nm and 50 for the other multilayers. In Tab. 7.1 the

growth parameters of the samples are listed. One should note that for $t_V = 3$ nm we have prepared two samples with slightly different preparation conditions. The samples are referred to as #1 and #2 in the figures below.

nominal thickness			experimental thickness		rms roughness		coherence length out-of-plane
t_V	t_{Co_2MnGe}	N	t_V	t_{Co_2MnGe}	σ_V	σ_{Co_2MnGe}	L_v
[nm]	[nm]	[nm]	[nm]	[nm]	[nm]	[nm]	[nm]
1.5	3	20	1.45	2.9	0.4	0.4	15.3
2	3	50	2.35	3.0	0.5	0.65	14.0
2.5	3	50	3.0	3.0	0.75	0.55	13.0
3	3 (#1)	50	3.4	3.4	0.65	0.85	13.0
3	3 (#2)	50	2.8	2.9	0.85	0.9	15.3
4	3	20	3.8	3.0	0.9	0.75	14.0
5	3	50	5.0	2.9	0.95	0.7	15.5

Table 7.1.: Overview of the structural parameters for the $[Co_2MnGe(t_{Co_2MnGe})/V(t_V)]_N$ multilayers with the nominal thickness (1st row), the number of periods N (2nd row), the experimental thickness (3rd row), the total rms roughness parameters (4th row) and the out-of-plane coherence length derived from the x-ray scattering data (see main text).

7.2. Structural Properties

7.2.1. Hard X-ray Scattering

The chemical structure of the multilayers was characterized by x-ray scattering at the beamline W1 at the HASYLAB (Hamburg, Germany) using a diffractometer with a standard two circle setup. The photon energy was chosen to be $h\nu = 8048$ eV, corresponding to Cu $K\alpha$ radiation ($\lambda = 0.154$ nm) or $h\nu = 7000$ eV ($\lambda = 0.177$ nm), which yields a slightly better contrast of the scattering lengths.

We have studied specular and diffuse (off-specular) scattering in the small angle regime combining longitudinal Q_z, offset Q_z and transverse Q_x scan geometries (see Fig. 7.1) [195]. The specular intensity was collected using standard Θ-2Θ scans along Q_z (with z as growth direction). A structurally well defined multilayer periodicity gives rise to Bragg peaks at $Q_z = 2\pi n/\Lambda$, where Λ is the bilayer thickness and n is an integer. Interdiffusion at the interfaces leads to diffuse intensity, which is not localized along the Q_z direction, but spreads out in the reciprocal space. To map out diffuse scattering,
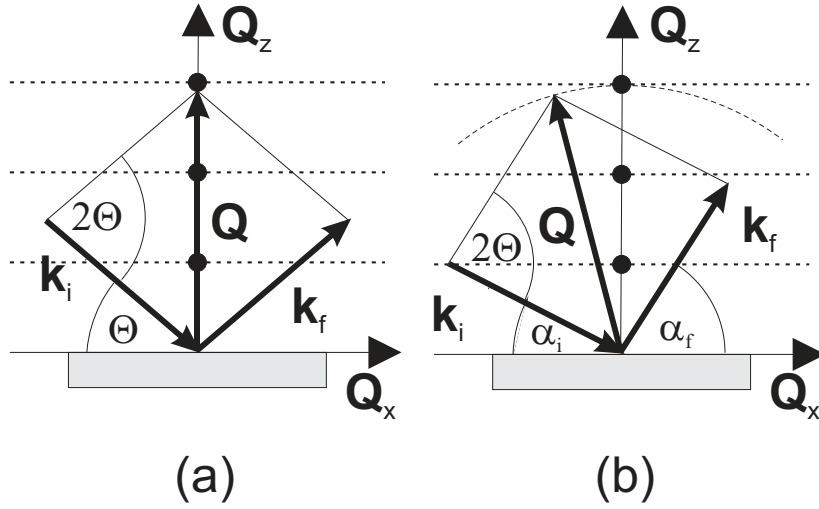
Figure 7.1.: X-ray and neutron scattering geometry in reciprocal space for (a) a specular reflectivity ($\Theta - 2\Theta$ scan, $Q_x = 0$) and (b) diffuse scattering (Q_x scan, Q_z constant). Bragg peaks in the specular reflectivity and diffuse Bragg sheets are schematically shown as dots and dotted lines, respectively.

offset Q_z and Q_x scans were taken. The offset Q_z scan corresponds to the longitudinal Q_z scan, but with the sample rotated by $\Delta\Theta$ from the specular direction, such that only diffuse intensity is collected (see Fig. 7.1). If the interface roughness of the multilayers is correlated along the growth direction, the features of the specular scan will be replicated. Transverse Q_x scans at the Q_z position of the multilayer Bragg peak give information on the *in-plane* correlation length and correlated roughness [154, 196]. If the probed Q_x regime is large enough, it is possible to distinguish between short-range disorder resulting from roughness and long-range disorder e.g. from terracing. Experimentally these scans are often realized by rocking scans, i.e. fixing the scattering angle 2Θ and varying α_i and α_f so that $\alpha_i + \alpha_f = constant$. If Q_x/Q_z is small, these scans approximate Q_x scans in reciprocal space. With the help of appropriate software it is also possible to perform proper Q_x scans, which we preferred for our measurements.

In order to obtain information on the in- and out-of-plane crystalline structure, high angle out-of-plane Bragg scans and grazing incidence in-plane Bragg scans using Cu $K\alpha$ radiation were carried out.

Small Angle Reflectivity

In Fig. 7.2 we show three representative small angle x-ray reflectivity scans of the samples $[Co_2MnGe(3nm)/V(1.5nm)]_{20}$ (a), $[Co_2MnGe(3nm)/V(2nm)]_{50}$ (b) and $[Co_2MnGe(3nm)/V(3nm)]_{50}$ (c) together with a simulation. The thickness of the

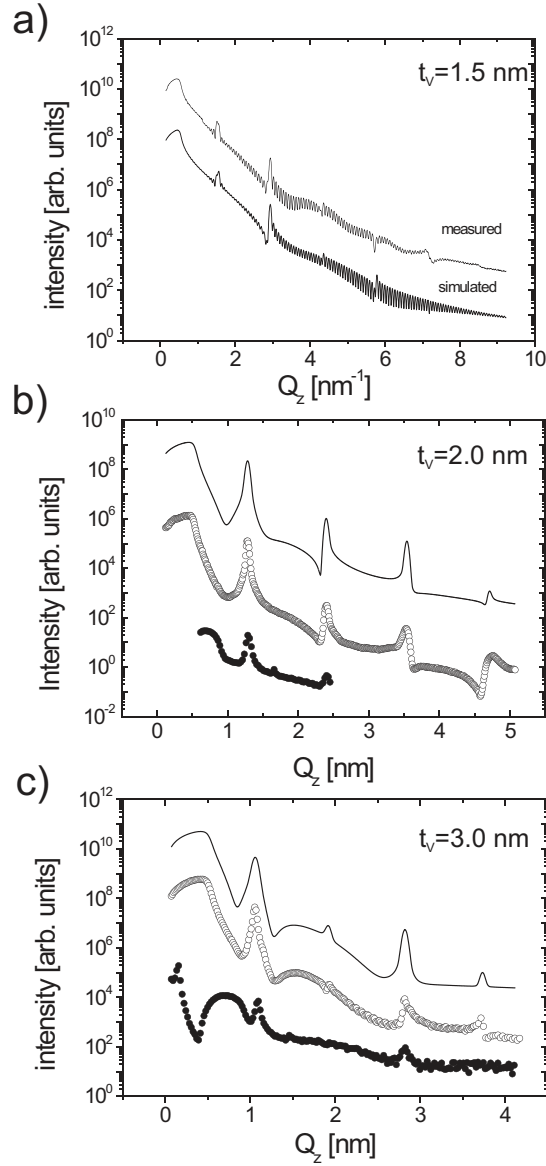Figure 7.2.: X-ray reflectivity scan of a series of $[Co_2MnGe(3nm)/V(t_V)]_N$ multilayers with a V layer thickness t_V as given in the figure. The open symbols denote the measured intensity, the simulation is shown by the full line, which is offset by a constant factor from the experimental data ((b),(c)). The filled circles show the corresponding off-specular scan (Θ-0.3°).

Co₂MnGe layers (t_{Co_2MnGe}) and that of the V layers (t_V) given in the brackets refer to the nominal thickness, as calculated from the sputtering rate. The index of the square brackets denotes the number of bilayers. The data were taken at $h\nu = 8048$ eV for the multilayers with $t_V = 1.5$, 3 nm and $h\nu = 7000$ eV for the sample with $t_V = 2$ nm, which gives a slightly better scattering contrast between both sublayers. Above the critical angle for total reflection Θ_c, the superstructure gives rise to Bragg peaks su-

perimposed on the Fresnel reflectivity. For the $[Co_2MnGe(3nm)/V(1.5nm)]_{20}$ multilayer (Fig. 7.2(a)) we observe superlattice reflections up to 4th order, revealing good interface quality and low fluctuations of the layer thickness. Due to the rather small difference in the electron density of V and Co_2MnGe and the low number of bilayer repetitions, the superlattice peaks are not very intense. But total layer thickness oscillations separated by $\Delta Q_z = 2\pi/D$, where D is the total layer thickness, reveal smooth surfaces and interfaces, which is confirmed by the simulations. The simulation using the Parratt formalism [138] (see Fig. 7.2) reproduces the thickness of the layers as well as their total rms roughness. (We refer to the roughness as *total*, because it contains correlated and uncorrelated parts, as well as contributions from interdiffusion at the interfaces, which cannot be distinguished by Q_z scans). In good agreement with the nominal thickness we get $t_V = 1.45$ nm and $t_{Co_2MnGe} = 2.9$ nm. The interface roughness is $\sigma_V = 0.4$ nm and $\sigma_{Co_2MnGe} = 0.4$ nm. These values are generated by the Parratt formalism from the spatial profile of the scattering length density; the interfacial roughness is included by varying the density with an error function. For the $[Co_2MnGe/V]$ multilayers we find that the scattering length densities in the V layers as well as in the Co_2MnGe layers deviate slightly from their bulk value.

For the samples $[Co_2MnGe(3nm)/V(2nm)]_{50}$ (Fig. 7.2(b)) and $[Co_2MnGe(3nm)/V(3nm)]_{50}$ (Fig. 7.2(c)) sharp superlattice peaks up to fourth order are visible, indicating smooth interfaces. Total thickness oscillations cannot be seen, since their period is smaller than the instrumental resolution. There is one specific characteristic for the $[Co_2MnGe(3nm)/V(3nm)]_{50}$ multilayer: both the Co_2MnGe and the V layer have the same thickness. This is the reason, why the second and the $4th$ superlattice peak are nearly suppressed in the reflectivity. Beside the reflectivity scans corresponding off-specular Q_z scans are shown. The off-specular data mainly replicate the specular one, indicating a significant correlated roughness along the growth direction. However, since the intensity in the off-specular scans is low, uncorrelated roughness seems to be quite high.

The values for the layer thickness and the total rms roughness as derived from the simulations are summarized in Tab. 7.1 for all multilayers studied. A comparison shows that the thicker the V layer in the multilayer, the higher the corresponding rms roughness σ_V of the V layer. Thus the interfaces are not smoothed by thicker V layers, on the contrary the interface quality is getting worse with increasing V thickness.

Diffuse Scattering

Additional information on the in-plane structure of the interfaces and their correlations can be obtained by analyzing the diffuse scattering. One important parameter wh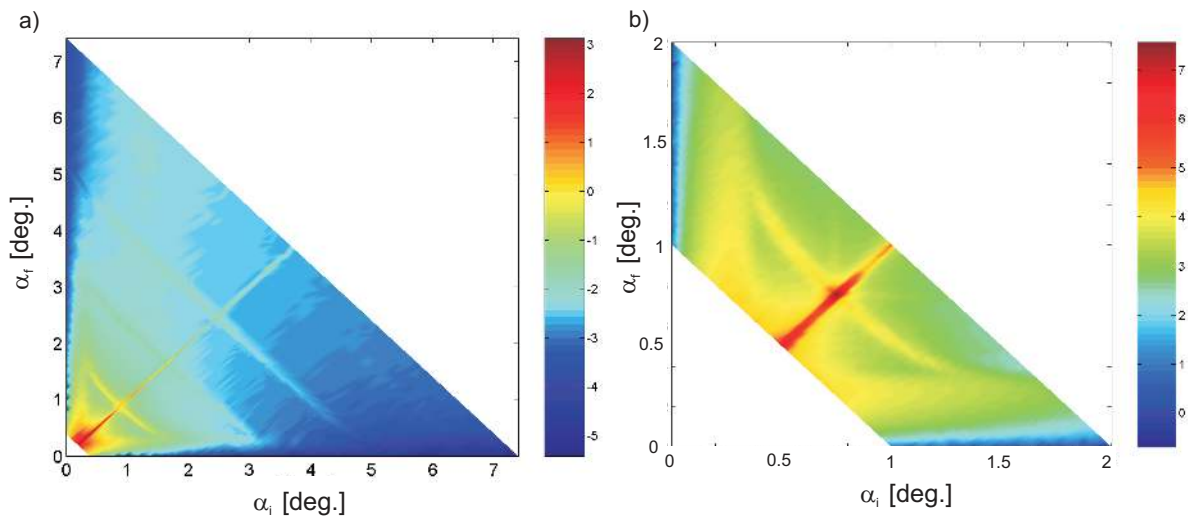ich can be derived is the in-plane correlation length ξ [154, 196]. In Fig. 7.3 we show 2D maps of the x-ray intensity scattered from the $[\text{Co}_2\text{MnGe}(3\text{nm})/\text{V}(2\text{nm})]_{50}$ (a) and the $[\text{Co}_2\text{MnGe}(3\text{nm})/\text{V}(3\text{nm})]_{50}$ (b) multilayer with the logarithm of the reflectivity contours plotted as a function of x-ray incident (α_i) and exit angles (α_f).

Figure 7.3.: Two-dimensional (2D) maps of the x-ray intensity scattered from the $[\text{Co}_2\text{MnGe}(3\text{nm})/\text{V}(2\text{nm})]_{50}$ (a) and $[\text{Co}_2\text{MnGe}(3\text{nm})/\text{V}(3\text{nm})]_{50}$ (b) multilayer as a function of the angle of incidence α_i and scattering α_f, respectively. The logarithmic intensity color scale is shown on the right hand side. Bragg sheets are clearly visible.

The diagonal ridge at $\alpha_i = \alpha_f$ is the specularly reflected intensity. Yoneda wings, clearly visible in the figure, result from enhanced reflection at those angular positions, where the incident (exit) beam impinges (leaves) at the critical angle of total external reflection with the sample surface. If the interfacial roughness is perfectly correlated in the vertical direction, the diffuse intensity along Q_z would be peaked at the Bragg conditions, visible as Bragg sheets. For random perpendicular roughness, the diffuse intensity will be spread out uniformly in Q_z [154, 196]. The multilayers studied here have a roughness correlation somewhere between these limiting cases. The Bragg sheets can easily be identified. The perpendicular roughness correlation exists, but the intensity is low, indicating that random roughness is predominant.

2D maps of specular and diffuse scattered intensity provide instantaneously a qualitative overview over roughness and its correlations. However, for a quantitative analysis
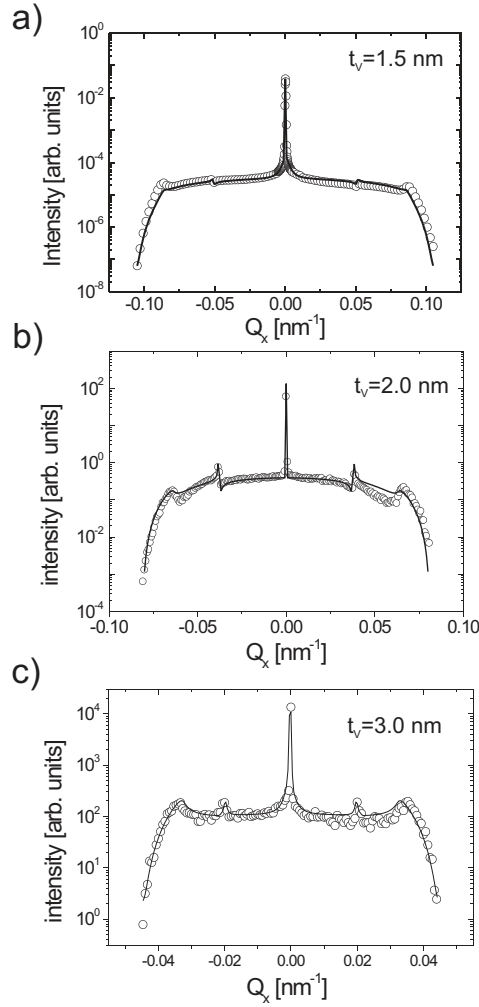
Figure 7.4.: Transverse Q_x scans of a series of $[Co_2MnGe(3nm)/V(t_V)]_{50}$ multilayers at the position of the second order Bragg peak (dots) together with a fit within the Mingh model [197] (line).

we have measured transverse Q_x scans of the samples discussed in Sec. 7.2.1, depicted in Fig. 7.4 together with a numerical simulation. The Q_x scans of the multilayers have been taken at the Q_z values corresponding to the second order Bragg peak. The experimental data are corrected for footprint effects arising from the fact that the probed volume of the sample changes with the angle of incidence. Besides the Yoneda wings additional peaks arising from the multilayer periodicity are visible. For the simulation we used the Mingh model [197], which describes an intermediate case between uncorrelated and completely correlated roughness and assumes that vertical correlations do not depend on the lateral scale of the roughness. The parameters used for this model are the vertical correlation length L_v, the horizontal correlation length L_h and the "hurst" parameter h, describing the jaggedness. The vertical correlation has been taken from the out-of-plane

coherence length obtained from large angle diffraction (see below). The jaggedness and the in-plane correlation length are left as the only free parameters, h being a value between 0.1 and 1. For small h values the surface is extremely jagged, if $h = 1$, the surface has smooth hills and valleys [196]. Best fits could be achieved for an in-plane correlation length ξ_1 in the order of 10 nm and $h_1 = 1$ (see Tab. 7.2). Including the instrumental resolution did not change the fit significantly. We attribute the horizontal correlation length to long-range disorder from grain boundaries.

For the sample $[Co_2MnGe(3\ nm)/V(1.5\ nm)]_{20}$ and $[Co_2MnGe(3\ nm)/V(3\ nm)]_{50}$ an additional component of diffuse scattering is visible at small Q_x values close to the specular peak. A fit within the Born approximation by a Lorentzian curve ($h_2 = 0.5$) derives a correlation length ξ_2 in the order of 1 μm, corresponding to the typical terrace length of the Al_2O_3 substrate due to its miscut angle.

Table 7.2.: Parameters of the transverse scans with the in-plane coherence lengths ξ_1 and ξ_2 and the hurst parameter h (see main text), derived at the position of the second Bragg peak (see main text).

	ξ_1 [nm]	h_1	ξ_2 [μm]	h_2
$[Co_2MnGe(3\ nm)/V(1.5\ nm)]_{20}$	10.0	1.0	0.4	0.5
$[Co_2MnGe(3\ nm)/V(2\ nm)]_{50}$	14.0	1.0	-	-
$[Co_2MnGe(3\ nm)/V(3\ nm)]_{50}$	20.0	1.0	1.0	0.5

High Angle Scattering

The $[Co_2MnGe/V]_N$ multilayers grow with perfect $Co_2MnGe(220)/V(110)$ texture out-of-plane. In Fig. 7.5 a representative longitudinal scan of the sample $[Co_2MnGe(3nm)/V(2nm)]_{50}$ at $\lambda = 0.177$ nm is depicted. Aside from the fundamental Bragg peak, the multilayer exhibits a rich satellite structure caused by chemical modulations. The spacing derived from the position of these satellite peaks corresponds exactly to the chemical modulation as determined from reflectivity measurements. Satellite peaks up to the order l=+2 and l=-3 can be resolved, indicative for a coherently grown superstructure in the growth direction. From the width of the satellite peaks at half maximum (FWHM) $\Delta(2\Theta)$ we derive the out-of-plane coherence length of the multilayer using the Scherrer equation $D_{coh} = 0.89\lambda/[\Delta(2\Theta) \cdot \cos(\Theta)]$ [188]. The calculation yields $D_{coh} = 13$ nm, thus comprising about 2 superlattice periods. (The values for the other samples of the study are listed in Tab. 7.1). The fundamental Bragg peak in Fig. 7.5 is positioned at $2\Theta = 49.75°$ i.e. at the middle position between the V (110)-Bragg
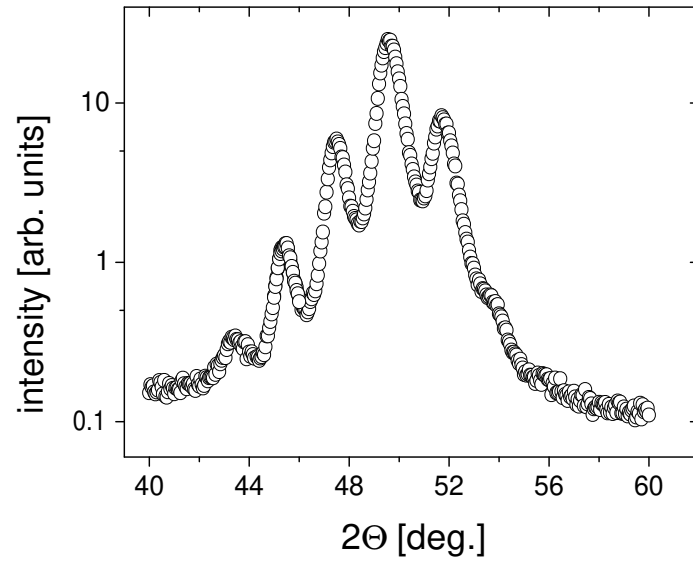
Figure 7.5.: Out-of-plane x-ray Bragg scan of the $[Co_2MnGe(3nm)/V(2nm)]_{50}$ multilayer at $\lambda = 0.177$ nm.

peak at $2\Theta = 48.8°$ and the Co_2MnGe (220)-peak at $2\Theta = 51.6°$, as expected for a coherently strained multilayer. As revealed by in-plane rocking scans all samples exhibit a broad distribution of in-plane Bragg peaks. Thus the samples can be characterized as polycrystalline multilayers rather than superlattices.

7.2.2. Soft X-ray Scattering

XMCD measurements on single thin Co$_2$MnGe films (see Sec. 6.4) revealed site disorder in the interior of the films and mixing and disorder at the interface, destroying the perfect $L2_1$ structure in the Heusler layer. This has the tendency to lower the ferromagnetic magnetization and concomitantly leads to a low or even vanishing spin polarization. In this context interfaces between Co$_2$MnGe and V layers in the studied multilayers need special attention, especially as the interface becomes more important with decreasing thickness of the Heusler layer. However, conventional structural x-ray characterization cannot resolve details of the magnetization profile of thin Heusler layers interleaved between V layers. For this purpose we have carried out a systematic investigation of x-ray resonant magnetic scattering (XRMS) on the Heusler multilayers using synchrotron radiation at the Co and Mn $L_{2,3}$ edges. XRMS combines the depth-resolving power of conventional small angle x-ray scattering with the element-sensitivity of XMCD. By observing the difference in the specular reflectivity for the two magnetization directions parallel and antiparallel to the photon helicity of circularly polarized x-rays in an energy scan across the $L_{2,3}$ edge of a magnetic element, one can derive the magnetization profile of a ferromagnetic thin film. This has been demonstrated convincingly for [Co$_2$MnGe/Au]$_{50}$ multilayers [182] and other systems [174, 198, 173]. Since in the [Co$_2$MnGe/V]$_{20}$ multilayers under study here, we have two magnetic elements, the analysis for Mn and Co can be carried out separately.

The soft XRMS experiments were performed with the diffractometer ALICE [185] at the undulator beamlines UE56/1-PGM and UE56/2-PGM2 at BESSY II (Berlin, Germany). The diffractometer comprises a two circle goniometer and works in horizontal scattering geometry. The vertical entrance and detector slits were set to 300 μm each, resulting in an instrument resolution of 0.14°. Circularly polarized light in the energy range of 600 eV - 900 eV was used with an energy resolution of approximately $\Delta E/E = 1 \cdot 10^{-4}$. A magnetic field can be applied in the scattering plane along the sample surface either parallel or antiparallel to the photon helicity, which corresponds to the longitudinal magneto-optical Kerr effect (L-MOKE) geometry. The maximum field was ± 0.11 T, high enough to fully saturate the ferromagnetic Co$_2$MnGe-layers. The magnetic contribution to the scattered intensity was measured by reversing the magnetic field while keeping the photon helicity fixed. In the L-MOKE geometry using circularly polarized soft x-rays the in-plane magnetization in the scattering plane is probed. The leading magnetic contributions to scattering arises from the charge-magnetic interference term (see Sec. 5.4).

In order to separate the structural and magnetic contribution to the scattered intensity

it is appropriate to measure the energy-dependent intensity at a fixed scattering angle 2Θ. All soft x-ray measurements shown below have been taken at room temperature.
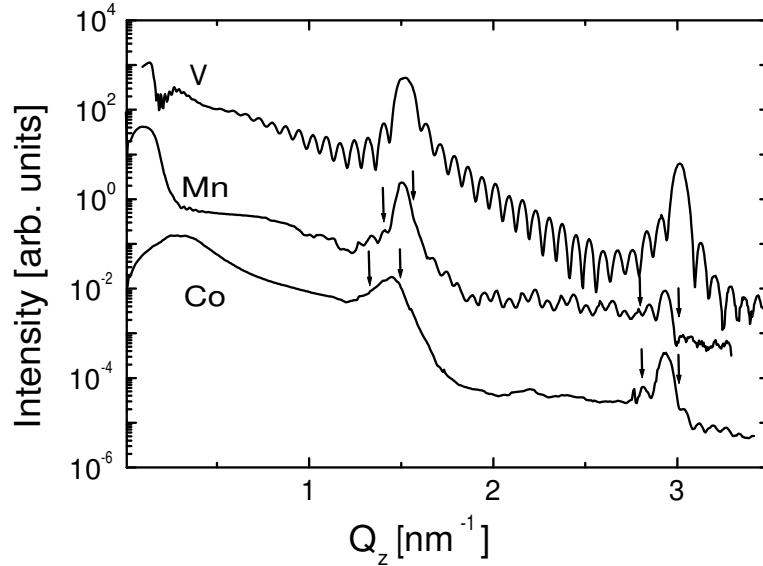
X-ray Resonant Magnetic Reflectivity

Figure 7.6.: Specular reflectivity of the sample $[\mathrm{Co_2MnGe(3nm)/V(1.5nm)}]_{20}$ measured with soft x-rays at the V ($E = 512$ eV), Mn ($E = 638$ eV) and Co ($E = 780$ eV) L_3 edges, respectively.

Fig. 7.6 shows the specular reflectivities of the $[\mathrm{Co_2MnGe(3nm)/V(1.5nm)}]_{20}$ multilayer up to the second-order Bragg peak, measured in remanence with circularly polarized soft x-rays at the V, Co and Mn L_3 edges in remanence. Due to the strong variation of the dispersion corrections at the absorption edges the Bragg peak positions in Q_z do not exactly coincide.

For the determination of the magnetization depth profile we have measured the reflected intensity of circularly polarized x-rays after magnetic saturation in the directions parallel (I_+) and antiparallel (I_-) to the photon helicity at the angular position of the Bragg peaks. The reflectivity spectra of the $[\mathrm{Co_2MnGe(3m)/V(1.5nm)}]_{20}$ multilayer are shown in Fig. 7.7 and 7.8 for the Co and Mn $L_{2,3}$ edges, respectively. Since the momentum transfer Q_z is proportional to the photon energy, a segment of the specular reflectivity is scanned, indicated by two vertical lines for each scan in Fig. 7.6.

The sum of the intensities $(I_+ + I_-)/2$ (upper panel in Figs. 7.7, 7.8) reflects the charge scattering and is independent of the magnetization of the sample. Clearly visible are the strong intensity variations due to resonant scattering, when the energy is passing
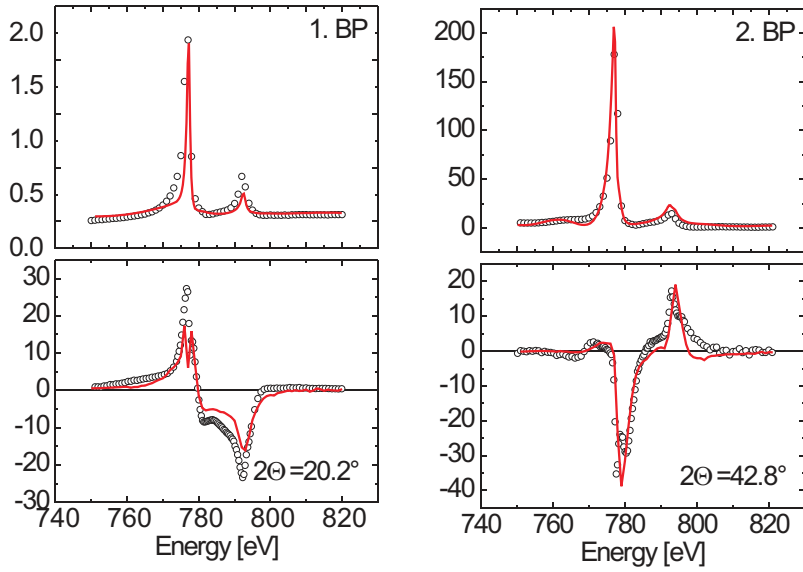
Figure 7.7.: Charge intensity $(I_+ + I_-)/2$ (top) and asymmetry $(I_+ - I_-)/(I_+ + I_-)$ for the sample [Co$_2$MnGe(3m)/V(1.5nm)]$_{20}$ at the first and second order Bragg peak (BP) at the Co $L_{2,3}$ absorption edges. The dots represent measured data, the lines are model calculations as described in the main text.
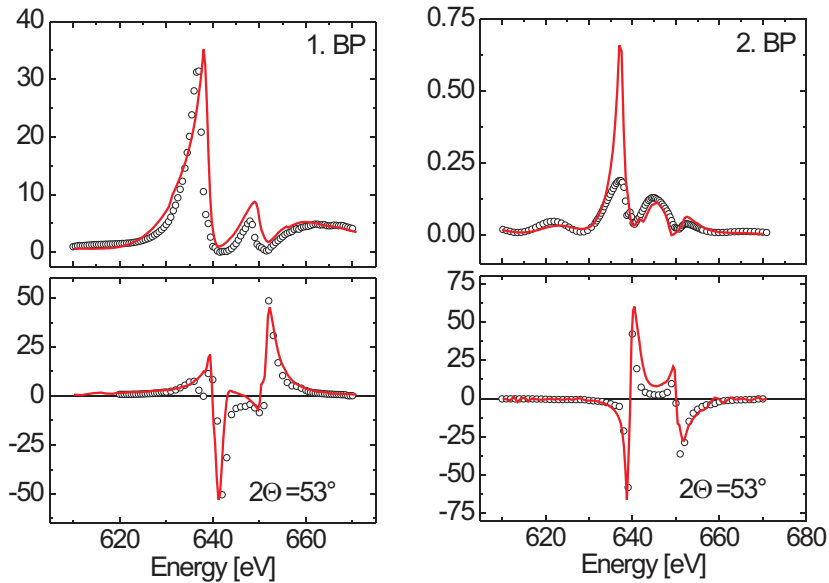
the L_3 and L_2 absorption edges of Co and Mn.

Figure 7.8.: Charge intensity (top) and asymmetry for the sample [Co$_2$MnGe(3m)/V(1.5nm)]$_{20}$ at the first and second order Bragg peak (BP) at the Mn $L_{2,3}$ absorption edges. The dots represent measured data, the lines are model calculations as described in the main text.

The magnetic contribution to the resonant scattering can best be visualized by taking the asymmetry ratio $(I_+ - I_-)/(I_+ + I_-)$ (second row in Figs. 7.7 and 7.8). In order to evaluate a magnetization depth profile for the multilayers from the magnetic part of the reflectivity spectra in Figs. 7.7 and 7.8, the energy-dependent intensities and asymmetries have been modelled within a magneto-optical matrix formalism developed by Zak et al. using the classical dielectric tensor (see Sec. 5.3). Within this formalism it is possible to calculate the reflectivity for electromagnetic radiation of arbitrary incidence angle and polarization on layered structures having an arbitrary magnetization depth profile. The formalism is not limited to Bragg reflections and has been used to model magneto-optical effects at soft x-ray energies in a number of publications before [170, 159, 199].

The analysis following Ref. [178] needs the knowledge of the energy dependence of the refractive index $n = 1 - (\delta_c + \delta_m) + i(\beta_c + \beta_m)$ with the charge contributions δ_c and β_c and the magnetic contributions δ_m and β_m (Fig. 7.9). This has been determined for a Co_2MnGe film in a separate x-ray absorption experiment [193]. The imaginary part of the refractive index is directly proportional to the absorption coefficient. The real part is then calculated using the Kramers-Kronig relations [200, 201]. Furthermore, from the previous analysis by hard x-ray small angle reflectivity we already have a set of well defined parameters characterizing the chemical structure, i.e. the thickness and roughness parameters, which we keep fixed in the fit of the spectra in Figs. 7.7 and 7.8.

In the upper panels of Figs. 7.7 and 7.8 we compare the measured and the calculated charge scattering intensity $(I_+ + I_-)/2$ taking all parameters from the hard x-ray measurements and the optical constants as just explained. One finds overall good agreement of the measured and calculated spectra.

The next and in the present context most essential step is to fit the asymmetry given in the lower panels in Figs. 7.7 and 7.8 with the same set of fixed structural and optical parameters. The only free parameter is the profile for the depth dependence of the ferromagnetic magnetization, in particular its shape, as described in detail below.

Assuming that the magnetic moment density profile is exactly identical to the chemical one, even qualitative features of the asymmetry spectra cannot be reproduced. Only if non-ferromagnetic interlayers at the interface of Co_2MnGe/V are allowed, the complex features of the experimental spectra can be modelled. Thus in the modelling we assume a magnetic moment density profile for Co and Mn which is narrower than the chemical density profile and may be asymmetric with respect to the chemical profile, i.e. the top non-ferromagnetic layer thickness t_t can be different from the bottom non-ferromagnetic layer thickness t_b. The best fits we obtained are shown as solid lines in the lower panels of
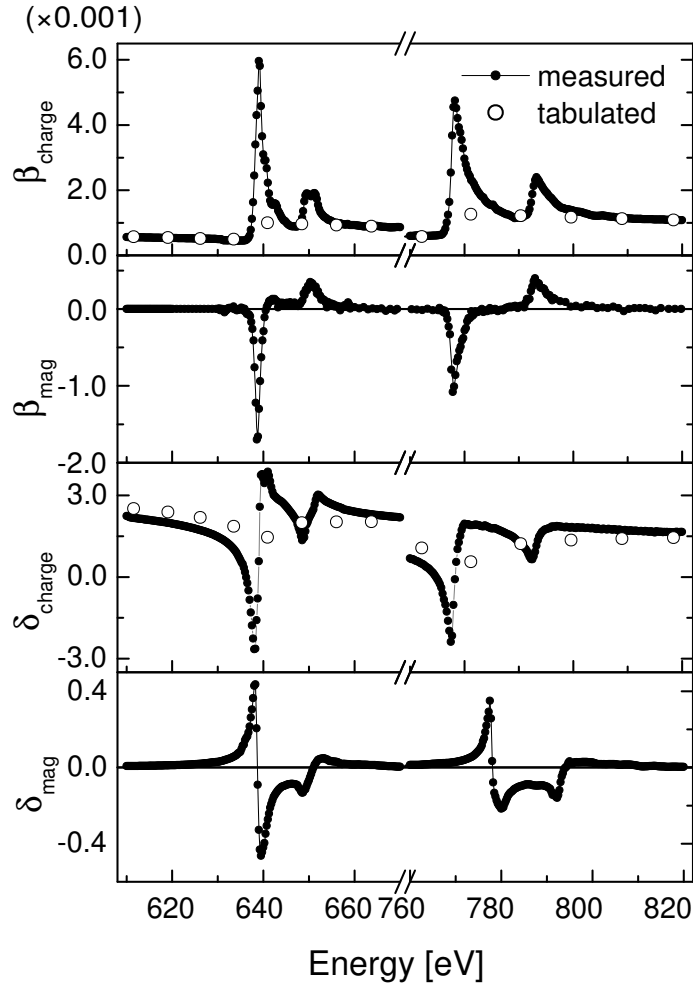
Figure 7.9.: Magneto-optical constants at the $L_{2,3}$ edges of Mn and Co and a comparison to the tabulated refractive index (open symbols) taken from Ref. [202].

Figs. 7.7 and 7.8 and reproduce the experimental spectra quite well. The corresponding magnetic moment density profiles of Co and Mn for the [Co$_2$MnGe/V]$_{20}$ multilayers are depicted in Fig. 7.10. For a better comparison of charge and magnetic profiles in Fig. 7.10 the refractive indices are normalized according to

$$\rho_c(z) = \frac{|\delta_c(z) - \delta_{c,\mathrm{V}}|}{|\delta_{c,\mathrm{Co_2MnGe}} - \delta_{c,\mathrm{V}}|}, \quad \rho_m(z) = \frac{\delta_m(z)}{\delta_{m,\mathrm{Co_2MnGe}}}, \tag{7.1}$$

so that $\rho(z) = 1$ ($\rho(z) = 0$) if the refractive index corresponds to the bulk Co$_2$MnGe (V) value. The corresponding imaginary part $\beta_{c,m}$ has the same z dependence as the real part. For Mn we derived a non-ferromagnetic layer thickness of $t_t = 0.4$ nm at the top and $t_b = 0.6$ nm at the bottom of the Co$_2$MnGe layer. For Co the fit yields $t_t = 0.3$ nm and $t_b = 0.3$ nm, respectively. The parameters describing the magnetic density profile

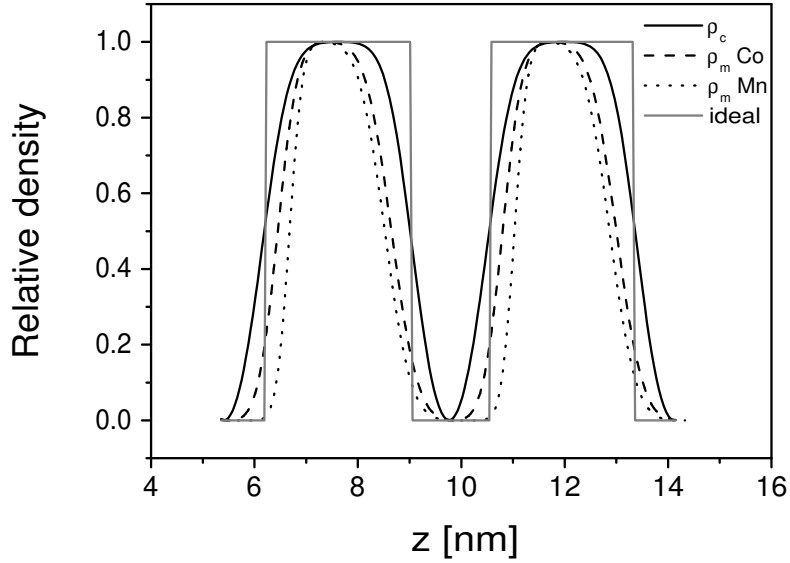Figure 7.10.: Structural and magnetic moment density profiles of Co and Mn for the sample $[Co_2MnGe(3nm)/V(1.5nm)]_{20}$ as determined from model calculations (see main text). z denotes an axis perpendicular to the film surface.

are summarized in Tab. 7.3. The profile is clearly asymmetric with the bottom non-ferromagnetic layer always thicker than the top non-ferromagnetic layer. One should note that the non-magnetic layer thickness derived for Mn is definitely larger than for Co.

The shape of the asymmetry at the Bragg peaks of different order is very sensitive to the magnetization profile assumed. In order to demonstrate this sensitivity we show a model calculation of the sample $[Co_2MnGe(3nm)/V(1.5nm)]_{20}$ for the second order Bragg peak of Co assuming a constant total non-ferromagnetic layer thickness $t_{nm} = t_t + t_b$ =0.7 nm and a variable t_b/t_t ratio in Fig. 7.11. Only the distribution with $t_t = 0.3$ nm and $t_b = 0.4$ nm can reproduce the experimental spectrum. It should be stressed that this asymmetric distribution yields the best fit in all orders of the Bragg peaks.

Table 7.3.: Parameters defining the magnetic moment density profile with the top and bottom non-ferromagnetic layer thickness t_t and t_b and the magnetic roughness parameter σ_{mag}.

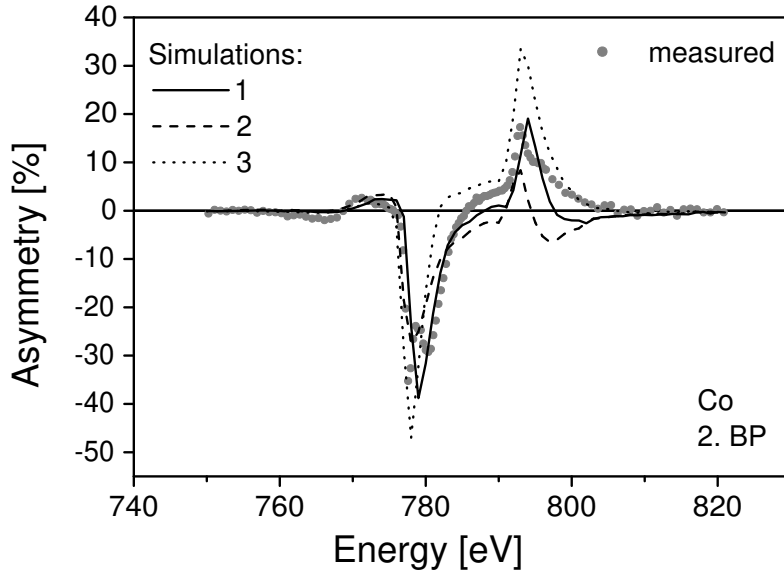|	Co $L_{2,3}$ edge			Mn $L_{2,3}$ edge		
	t_t [nm]	t_b [nm]	σ_{mag} [nm]	t_t [nm]	t_b [nm]	σ_{mag} [nm]
$[Co_2MnGe(3nm)/V(1.5nm)]_{20}$	0.3	0.4	0.3	0.4	0.6	0.3

Figure 7.11.: Model calculations of the second order BP compared to the experiment. The ratio of the bottom non-ferromagnetic layer thickness t_b and the top non-ferromagnetic layer thickness t_t is varied, while the sum $t_b+t_t = 0.7$ nm is kept fixed. (1) $t_t = 0.3$ nm, $t_b = 0.4$ nm, (2) $t_t = 0.1$ nm, $t_b = 0.6$ nm, (3) $t_t = 0.6$ nm, $t_b = 0.1$ nm

Microscopic Origin of the Magnetic Moment Density Profile

What remains to be explained is the microscopic origin for the magnetization profile inside the Heusler layers, and especially the origin of the very different Co and Mn profile. XRMS cannot resolve this question, it only proves its existence. In Fig. 7.12 we propose a qualitative model as an explanation, which is based on the intimate relationship between the chemical structure and the ferromagnetism of a thin Co₂MnGe layer. Starting from the bottom of the Heusler layer growing on a V film, the first few Heusler monolayers grow as a bcc-type random mixture of the Ge, Mn and Co atoms. This layer has a low saturation magnetization and appears essentially non-magnetic in the XRMS experiments at room temperature. Then the Heusler film starts developing chemical short-range order with each of the Heusler constituents beginning to occupy its own $L2_1$ type sublattice. However, there is still substantial site disorder between the Co and Mn positions. Theoretical model calculations [203] have shown that in this case there is an essential difference between the magnetic behavior of an antisite Co and an antisite Mn atom: Mn sitting on a regular Co position has its moment oriented antiparallel to the Co-nearest neighbours moments, whereas Co on a Mn position keeps its parallel moment direction. Thus in XRMS, which measures the average Mn moment density, the Mn moment is not yet visible, whereas the Co moment is detected. This
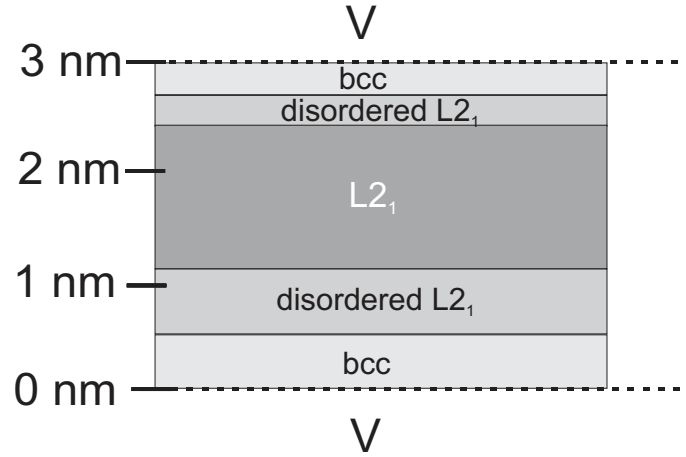
Figure 7.12.: Schematic picture of the sequence of structural phases in a 3 nm thick Co$_2$MnGe film between two V-layers. The vertical scale gives the distance from the bottom of the Co$_2$MnGe-film.

explains why the magnetization profile for Mn is narrower than the Co profile. Then, in the core of the Heusler layer, the chemical order approaches the ideal $L2_1$ superstructure and the Mn moments are seen in the XRMS signal.

Moving further towards the top of the Heusler film in Fig. 7.12 one finds the same sequence of magnetic phases in reversed order, however definitely thinner than at the bottom of the Heusler film. This indicates that upon the deposition of the top V layer a few monolayers of the ordered $L2_1$ type Heusler layer become disordered again. Thus it seems that interactions at the interface destroy the chemical ordering of the Heusler phase, or in other terms, at the interfaces in thermodynamic equilibrium the Heusler $L2_1$ type order is unstable.

Magnetic Diffuse Scattering

Similar to the case of the non-magnetic off-specular scattering, one also can study the off-specular magnetic scattering and derive information about the correlation of the magnetic roughness [204, 181, 183, 176]. Fig. 7.13 shows charge $(I_+ + I_-)/2$ and magnetic $(I_+ - I_-)$ transverse scans at the Q_z position of the first order superlattice peak for the sample studied at the Co and Mn edge, respectively. Both charge and magnetic scans exhibit three components: the specular peak at $Q_x = 0$, a narrow component due to the substrate roughness (ξ_1, h_1), and a broad diffuse component corresponding to a short-range in-plane correlation (ξ_2, h_2). The experimental data do not show any indication of total reflections like Yoneda wings or pseudo Bragg peaks from multiple reflectivity. Therefore, the Born approximation is sufficient to describe the diffuse scattering [181,
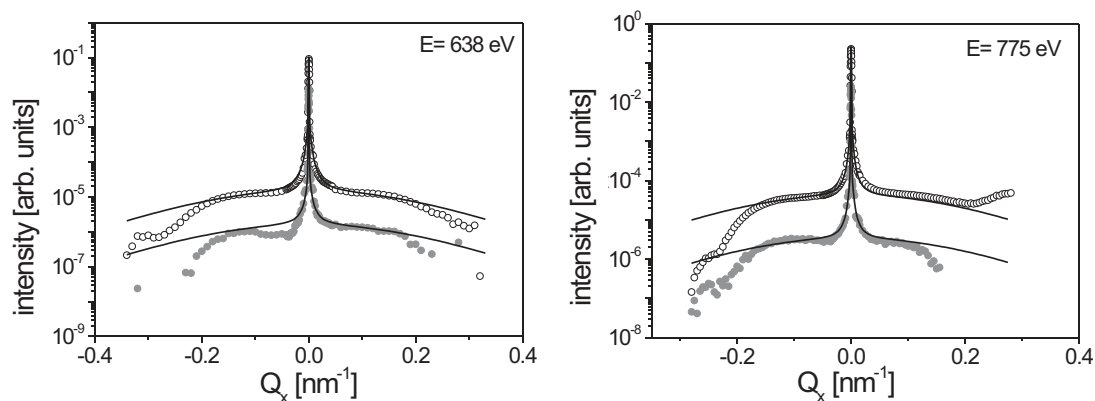
Figure 7.13.: Transverse Q_x scans at the Mn (a) and Co edge (b) for the [Co$_2$MnGe(3nm)/V(1.5nm)]$_{20}$ multilayer. The measured charge (open circles) and magnetic (grey circles) intensity is modelled within the framework of Born approximation (lines) as described in the main text.

183]. The parameters for the best fits of the transverse scans are listed in Tab. 7.4.

For simplicity the vertical correlation of the interfaces is assumed to be perfect. This assumption is justified by the fact that the vertical correlation length as determined from the hard x-ray data is larger than the penetration depth of the soft x-rays at these energies and incidence angles. The roughness parameters for the charge and the magnetization are taken from the simulation of the reflectivity.

Since the intensity difference $(I_+ - I_-)$ is dominated by the charge-magnetic interference term, the existence of magnetic diffuse scattering at the Bragg peaks already indicates that the chemical and magnetic interfaces are correlated. Within the experimental error bars the magnetic interface morphology follows exactly the chemical one (see Tab. 7.4). This observation confirms that the presence of non-ferromagnetic layers is intrinsically correlated to chemical disorder in the sample. Both chemical and magnetic interfaces have a correlated roughness on the scale of the in-plane crystallite size.

Table 7.4.: Parameters of the transverse scans with the in-plane coherence lengths ξ_1 and ξ_2 and the hurst parameter h (see main text) as derived from Fig. 7.13.

	[Co$_2$MnGe/V]$_{20}$			
	ξ_1 [μm]	h_1	ξ_2 [nm]	h_2
Co, charge	0.65	0.5	9.0	1.0
Co, charge-magnetic	0.55	0.5	9.0	1.0
Mn, charge	0.5	0.5	9.0	1.0
Mn, charge-magnetic	0.6	0.4	9.0	1.0

In summary of this section, XRMS has proven to be a powerful technique for the determination of the magnetic moment density profiles in Heusler multilayers. However, the procedure takes some efforts: First, one needs high quality multilayers and second, a complete set of fixed input parameters from the analysis of hard x-ray scattering and optical constants determined by x-ray absorption. Only then the magnetic moment density profile is left as the only free parameter in the fitting procedure and an unambiguous determination of the profile becomes possible.

For the multilayer system $[Co_2MnGe/V]_N$, which we have studied here, the analysis of the XRMS spectra revealed that at room temperature the Co_2MnGe layers interleaved between V possess non-ferromagnetic or weakly ferromagnetic layers at the interface with a thickness of about 0.5 nm at the bottom and 0.3 nm at the top. The loss of Mn moments caused by massive structural disorder leads to the fact that for a 3 nm Co_2MnGe layer typically only the inner core of about 1.5 nm thickness develops the full magnetization of the chemically ordered bulk Heusler compound. XRMS does not reveal the microscopic origin for the loss of magnetic moments as can be segregation of one of the Heusler atomic species at the interface, interdiffusion of atoms from the V layer, structural disorder or a combination of these effects. We think that beside chemical disorder additionally the diffusion of V into the Heusler surface layer contributes to disorder and loss of moments.

The non-ferromagnetic interface layers offer a plausible explanation for several peculiar magnetic features we have observed in the $[Co_2MnGe/V]_N$ multilayers. The small GMR amplitude [74] e.g. finds a natural explanation, since the main contribution to the GMR originates from an asymmetric spin dependent scattering at the interfaces.

More generally, it is feasible that in thin film heterostructures with Heusler compounds weakly ferromagnetic interface layers might be a common phenomenon. For the fabrication of tunnel junctions with an Al_2O_3 barrier e.g. one usually starts with the preparation of a metallic Al layer on the top of the Heusler film [57]. In a second step the Al film is oxidized thermally or by plasma oxidation. If during the deposition of the Al layer on top of the Heusler film the ferromagnetic order of a Heusler surface layer is weakened and concomitantly the full spin polarization is lost, one could easily explain the difficulty to observe the predicted 100% spin polarization experimentally in TMR junctions using the Heusler half-metals [205, 206].

7.3. Magnetic Properties

7.3.1. Magnetization Measurements

The magnetic measurements of the samples were carried out by a commercial SQUID-magnetometer (Quantum Design MPMS system). In Fig. 7.14 we depict magnetic
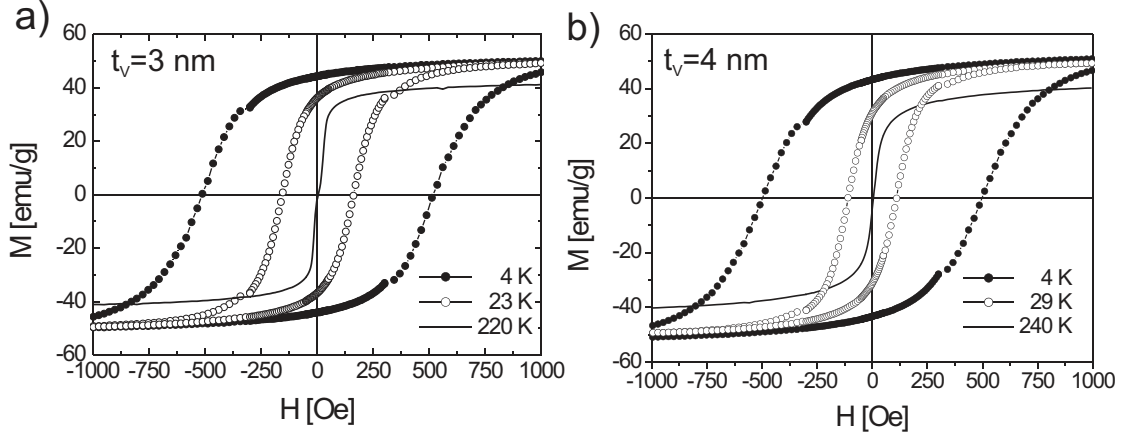

Figure 7.14.: Hysteresis loops of the multilayers [Co$_2$MnGe(3nm)/V(3nm)]$_{50}$ (#1) (a) and [Co$_2$MnGe(3nm)/V(4nm)]$_{20}$ (b) measured at different temperatures indicated in the figure. The mass in the magnetization unit refers to the magnetic layer. Shown only part of the hystereses. Saturation is higher.

hysteresis loops for [Co$_2$MnGe/V] multilayers with a V thickness $t_V = 3$ nm (a) and $t_V = 4$ nm (b), which are representative for all other multilayers studied. The ferromagnetic saturation magnetization at 4 K is about 50 emu/g, corresponding to 45% of the expected saturation magnetization, if all Heusler layers would exhibit the full bulk magnetization. The reduction should be attributed to the intermixing at the interfaces giving rise to non-ferromagnetic or weakly ferromagnetic interlayers. With the magnetic density profile derived from the soft x-ray scattering data, one can estimate that about 45% of the 3.0 nm thick Co$_2$MnGe layer belong to the interfaces.

The remanent magnetization of the samples is 90% of the saturation value at 4 K. Interestingly, there is no observable magnetic remanence at higher temperature, the magnetization curve is completely reversible for temperatures above about 150 K, while the saturation magnetization is only slightly reduced. We consider this as a first hint to an antiferromagnetic (af) order. Most of our multilayers possess a growth induced uniaxial magnetic anisotropy similar to the thick films discussed in Chap. 6, but with a definitely smaller amplitude on the order of 20 Oe for the anisotropy fields. For the hysteresis curve measurements in Fig. 7.14 the field is applied along the magnetic easy axis, thus the vanishing remanent magnetization cannot simply be explained by a

magnetic anisotropy field perpendicular to the field direction. A study revealed that the remanent magnetization vanishes for all thicknesses of the non-magnetic interlayer above $t_V = 1.5$ nm. This could indicate an af coupling, but then it would be independent of the interlayer thickness, which does not at all fit into the scheme of an IEC mechanism [18].
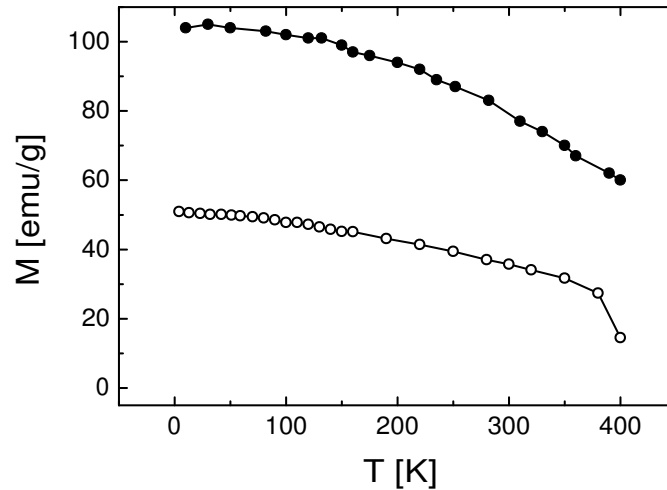

Figure 7.15.: Ferromagnetic saturation magnetization of bulk Co_2MnGe (solid circles) and the $[Co_2MnGe(3nm)/V(3nm)]_{50}$ multilayer (open symbols) versus temperature.

In Fig. 7.15 we have compared the ferromagnetic saturation magnetization of bulk Co_2MnGe and the sample $[Co_2MnGe(3nm)/V(3nm)]_{50}$. It is apparent that the saturation magnetization and the Curie temperature in the multilayer are much lower than in the bulk Co_2MnGe phase. We estimate a ferromagnetic Curie temperature T_c of about 450 K.

Fig. 7.16 shows hysteresis loops of the sample $[Co_2MnGe(3nm)/V(4nm)]_{20}$ measured with the magnetic field applied perpendicular to the film plane. In contrast to the case of the single films, the magnetization is strongly anisotropic with an easy axis lying in-plane.

The susceptibility χ of the two samples $[Co_2MnGe(3nm)/V(3nm)]_{50}$ and $[Co_2MnGe(3nm)/V(4nm)]_{20}$ measured in a dc field of $+10$ Oe after cooling in zero field (zfc) and in a field of $+2000$ Oe (fc) is shown in Fig. 7.17. For the sample with $t_V = 4$ nm the susceptibility is reversible and increases with decreasing temperature down to $T = 150$ K where one observes the onset of strong magnetic irreversibility and a maximum in $\chi(T)$. This is the classical behaviour of a spin glass or cluster glass transition at a freezing temperature T_f (see Chap. 3). As will be shown below, the sus-
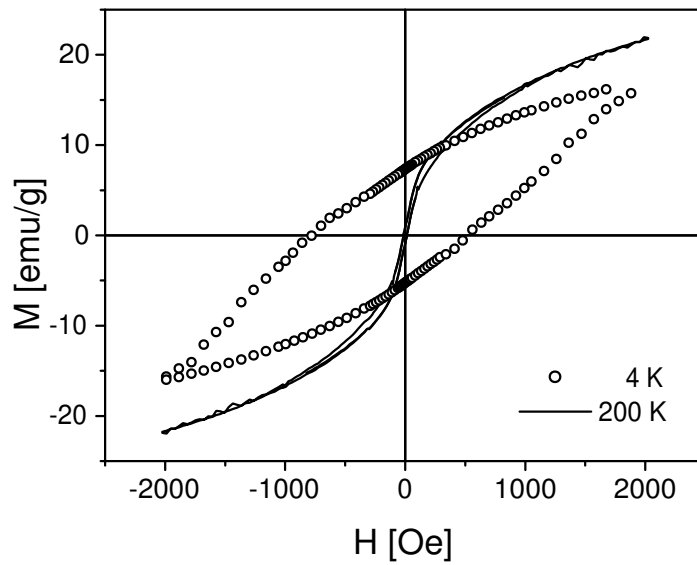
Figure 7.16.: Hysteresis loops of the sample [Co$_2$MnGe(3nm)/V(4nm)]$_{20}$ at 4 K (open circles) and 200 K (solid line). The magnetic field has been applied perpendicular to the film plane.
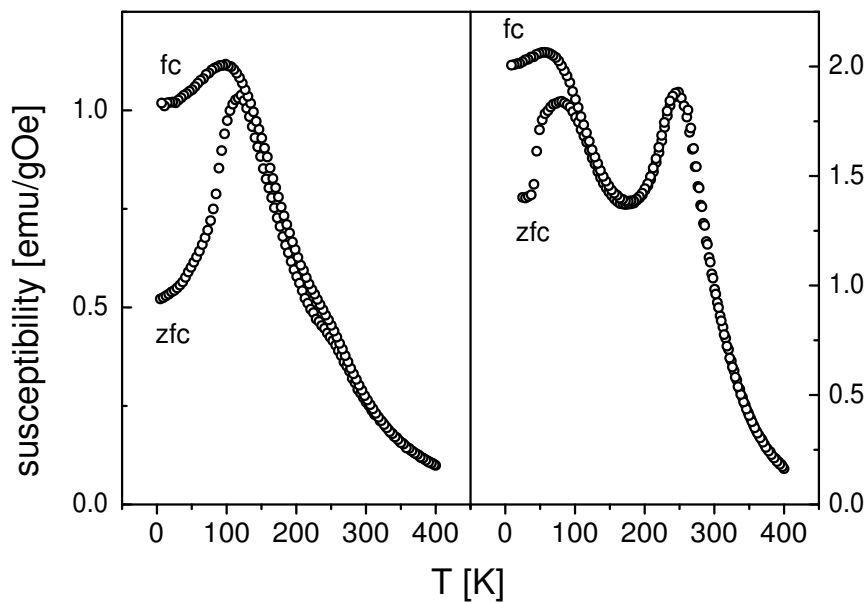

Figure 7.17.: The dc magnetic susceptibility measured in a field of +10 Oe for the [Co$_2$MnGe(3nm)/V(4nm)]$_{20}$ (left panel) and the [Co$_2$MnGe(3nm)/V(3nm)]$_{50}$ (#1) multilayer (right panel). The field cooled curve (fc) after cooling in $H = +2$ kOe and zero-field cooled curve (zfc) are plotted.

ceptibility above T_f reveals the existence of large clusters with ferromagnetic short-range order. Therefore the classification as cluster glass transition seems to be appropriate.

The low temperature susceptibility of the sample with $t_V = 3$ nm shows a strong irreversibility at 100 K. In addition there is a peak in the susceptibility at 250 K, indicating another magnetic phase transition. In the next section we will show that this transition temperature indicates an onset of antiferromagnetic interlayer long-range order.

7.3.2. Magnetic Neutron Scattering

Unpolarized and polarized neutron reflectivity measurements were performed to identify and characterize the magnetic structure of the multilayers. We obtained these data at the Institute Laue-Langevin in Grenoble (France) mainly with the ADAM reflectometer [207], but also with the EVA instrument [208]. The reflectometer ADAM is an angle dispersive fixed wavelength machine working at $\lambda = 0.44$ nm. Transmission supermirrors allow the polarization and analysis of the neutron spin direction. Using 180° spin flippers it is possible to measure the non-spin-flip (NSF) ((++) and (−−)) and spin-flip (SF) ((+−) and (−+)) scattered intensities, which are collected by a 2D position sensitive detector. The efficiency of spin polarizing and analyzing devices is typically 97%. A displex cryostat and a solenoid serve for a temperature range from 10 to 600 K and a field range up to 1 T. We used the ADAM reflectometer for polarized and unpolarized reflectivity studies applying the same scan geometries as in the x-ray experiments (see Fig. 7.1).

In the polarized neutron reflectivity scans all four cross sections (++), (−−), (+−) and (−+) are measured. Here +(−) denotes the up (down) spin polarization of the incident and reflected neutrons relative to an applied field at the sample position defining a polarization vector $\mathbf{P}$, here parallel to the sample plane. The non-spin-flip intensities contain information on the chemical structure and are sensitive to the projection of the in-plane magnetization of the sample parallel to $\mathbf{P}$. This leads to a splitting of the (++) and (−−) intensities, if the sample is ferromagnetic. The spin-flip channels are sensitive to the magnetic induction projected perpendicular to $\mathbf{P}$. The spin-flip is of purely magnetic origin and does not occur in coherent nuclear scattering. By measuring SF and NSF reflectivities the magnitude and orientation of the in-plane magnetic induction $B = 4\pi M$ of the sample can be determined.

7. [Co₂MnGe/V]ₙ Multilayers

Antiferromagnetic Coupling

In order to verify the hypothesis of an antiferromagnetic (af) interlayer order in the multilayers, we performed specular neutron reflectivity measurements. Fig. 7.18 shows the unpolarized neutron reflectivity scans of the multilayers $[Co_2MnGe/V(t_V)]_N$ with $t_V = 1.5, 2.0, 2.5$, and 3 nm measured in zero field at room temperature together with a numerical simulation. In addition to the first order structural superlattice peak there is a
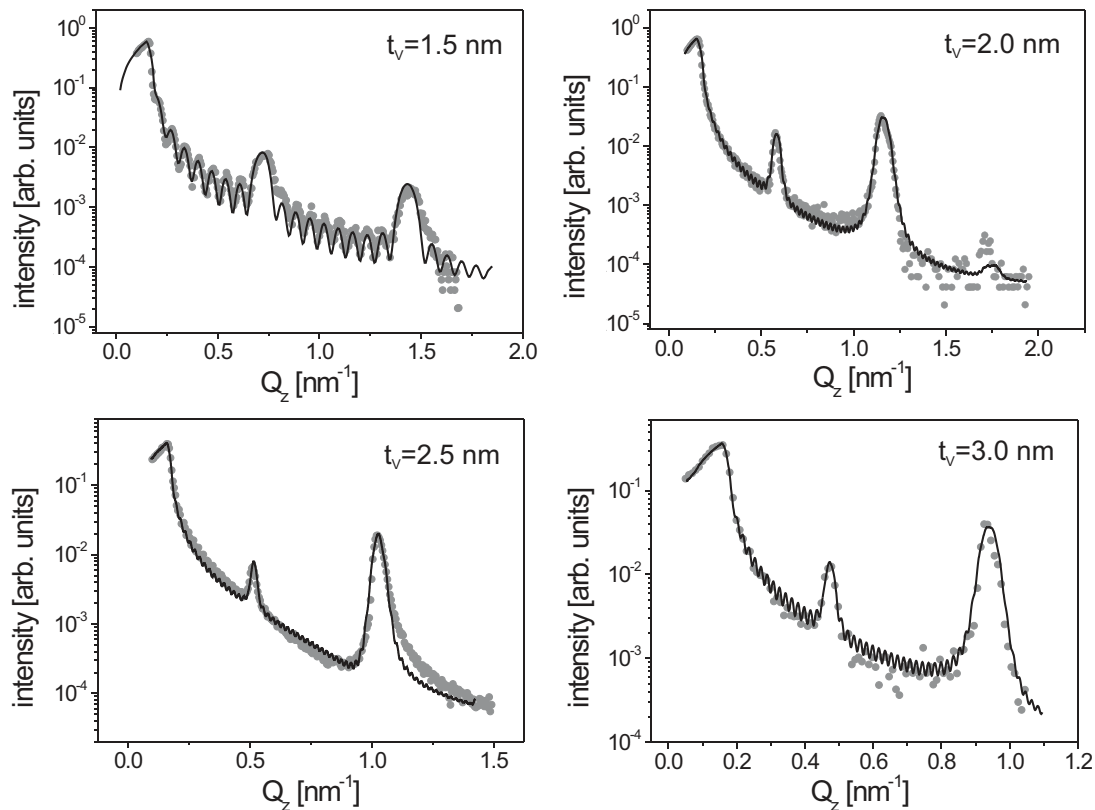

Figure 7.18.: Specular unpolarized neutron reflectivity scans of a series of samples $[Co_2MnGe/V(t_V)]_N$ with $t_V = 1.5, 2.0, 2.5$, and 3 nm at RT in remanence denoted by open symbols. The lines show a fit to the data points by the Parratt formalism. Aside from the structural peaks, half-order antiferromagnetic peaks are clearly visible.

magnetic half-order peak due to a doubling of the multilayer periodicity. For the sample $[Co_2MnGe(3nm)/V(2nm)]_{50}$ the second af peak can also be resolved. This and the narrow width of the af peaks indicate that the af order might be coherent throughout the whole multilayer stack. In order to simulate the unpolarized neutron reflectivity data in Fig. 7.18, we used the structural parameters from the simulation of the x-ray data in Sec. 7.2.1 and included non-ferromagnetic layers into the magnetization profile, as derived from the soft x-ray measurements in Sec. 7.2.2. We assumed a perfect

Table 7.5.: Magnetic moments of one Co$_2$MnGe formula unit derived for the multilayers [Co$_2$MnGe/V(t_V)]$_N$ with $t_V = 1.5, 2.0, 2.5,$ and 3 nm by simulations to the neutron reflectivity scans at RT.

t_V [nm]	m_{Co_2MnGe} [μ_B]
1.5	1.5
2.0	0.8
2.5	0.5
3.0	0.6

antiferromagnetic coupling through the multilayer stack and sublattices, which have equal magnetizations. This reduces the number of free parameters in the fit drastically, so that only the magnetic scattering length densities are left as free parameters. The simulations were performed using the super-iterative routine generalizing a conventional Parratt formalism for the case of reflection of spin 1/2 particles from a stack of magnetic layers [148, 209]. At a large number of layers this routine is numerically more stable than the super-matrix formalism proposed earlier [147, 145].

The result of the simulation is included in Fig. 7.18. The derived magnetic moments for one Co$_2$MnGe formula unit are summarized in Tab. 7.5. It should be noted that the fit of unpolarized neutron reflectivity provides values for the sublattice magnetic moments that are definitely lower than those determined with SQUID measurements.

We also studied other multilayers with intermediate V thicknesses by magnetization measurements and found that the coupling is always antiferromagnetic. Thus for a V layer thickness in the range between 1.5 nm$\leq t_V \leq$ 3 nm the samples show antiferro-magnetic long-range order. However, no indications of an oscillatory character of the af order, as expected for the IEC mechanism, could be discerned. For the samples with a V layer thickness $t_V \geq$ 4 nm no af peak could be detected, although the magnetization measurements at higher temperatures showed zero remanence.

Microscopic Picture

More detailed insight into the magnetization *vector* arrangement over the multi-layers stack can be achieved by an analysis of PNR data. Figure 7.19 shows specular PNR data collected for the multilayers [Co$_2$MnGe(3nm)/V(2nm)]$_{50}$ (a), [Co$_2$MnGe(3nm)/V(2.5nm)]$_{50}$ (b) and [Co$_2$MnGe(3nm)/V(3nm)]$_{50}$ (c). Two NSF cross sections and the spin-flip $(-+)$ channel are plotted together with the result of a computer simulation. The reflectivity scans were performed at 12 K after zero-field cooling

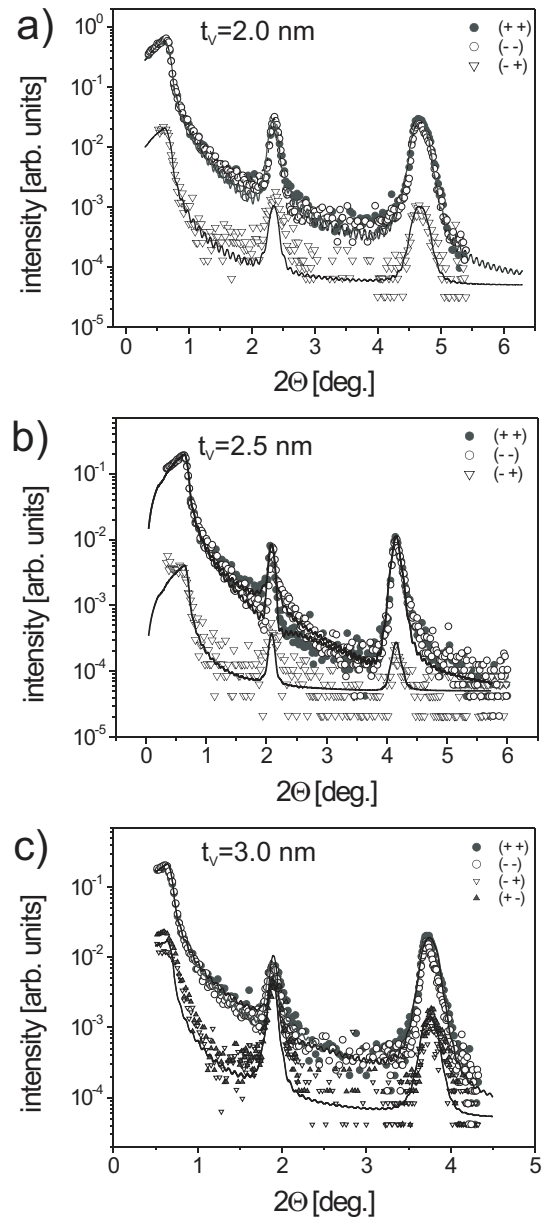and applying a small field of 10 Oe to provide a neutron guide field. For the multilayer

Figure 7.19.: Specular polarized neutron reflectivity scans for non-spin-flip ((++) and (−−)) and for spin-flip ((−+),(+−)) channels of the multilayers (a) $[Co_2MnGe(3nm)/V(2nm)]_{50}$, (b) $[Co_2MnGe(3nm)/V(2.5nm)]_{50}$ and (c) $[Co_2MnGe(3nm)/V(3nm)]_{50}$ (#1). Measurements are taken at 12 K.

with $t_V = 3$ nm there is only a small splitting of the NSF cross sections at the structural first order peak, well within the range of the error bars. Moreover, the total reflection edges for the (++) and (−−) channel coincide. This indicates that there is essentially no ferromagnetic contribution to the first order peak in the magnetic ground state. The SF
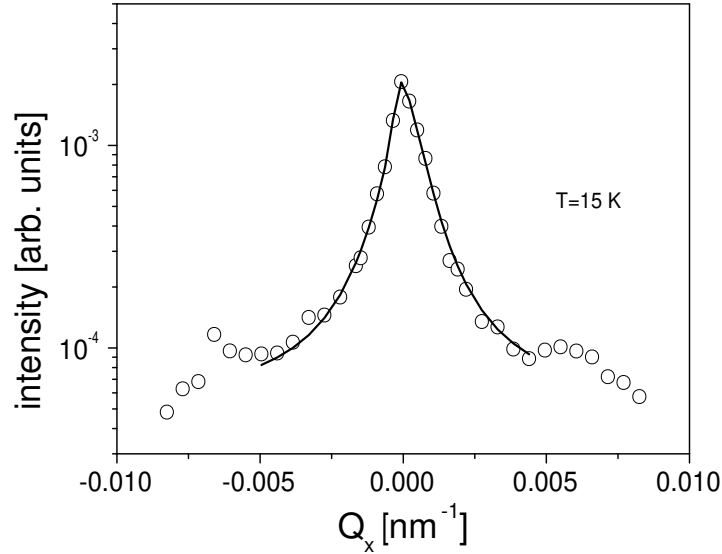
Figure 7.20.: Neutron transverse scan of the $[Co_2MnGe(3nm)/V(3nm)]_{50}$ (#1) sample at the position of the half-order Bragg peak (dots) together with a fit within the framework of the Born approximation (line).

cross section is peaked at the af half-order peak and possesses nearly the same intensity as the NSF cross sections. The specular PNR data can well be simulated using a model, which assumes a coherent af coupling through the multilayer stack, the antiferromagnetic sublattice having the magnetic moments m_1 and $-m_2$, respectively. In order to provide both spin-flip and non-spin-flip reflections at the af peak position, the model assumes that the sublattice magnetizations have projections parallel and perpendicular to the applied field. This is introduced by the fitting parameter $\langle \cos \gamma \rangle$, where γ is the angle between the af axis and the applied field. The transverse dispersion $\langle \sin^2 \gamma \rangle$ with the constraint $\langle \cos \gamma \rangle^2 \leq \langle \cos^2 \gamma \rangle = 1 - \langle \sin^2 \gamma \rangle$ accounts for a possible spread in the af axis directions over the sample surface.

This model can perfectly describe the sets of data in Fig. 7.19 with the parameters consistent with those obtained from the fit of the data in Fig. 7.18 (see Tab. 7.5). In particular, for the sample with $t_V = 3$ nm one gets: $m_1 = m_2 \approx 0.8 \ \mu_B/formula$ $unit$, $\langle \cos \gamma \rangle = 0.7$, $\langle \sin^2 \gamma \rangle = 0.35$. Then one can speculate on the reasons for an appreciable loss of the layer magnetization in this sample with respect to the saturation magnetization which is $m_1 = m_2 = 2.5 \ \mu_B/formula \ unit$, as well as with respect to the value determined above with magnetometry.

The results of our PNR simulations are based on the hypothesis that the layers are homogeneously magnetized over the neutron coherence area: specular reflectivity does not provide any direct information on the lateral length scales of the film, completely

7. *[Co₂MnGe/V]$_N$ Multilayers*

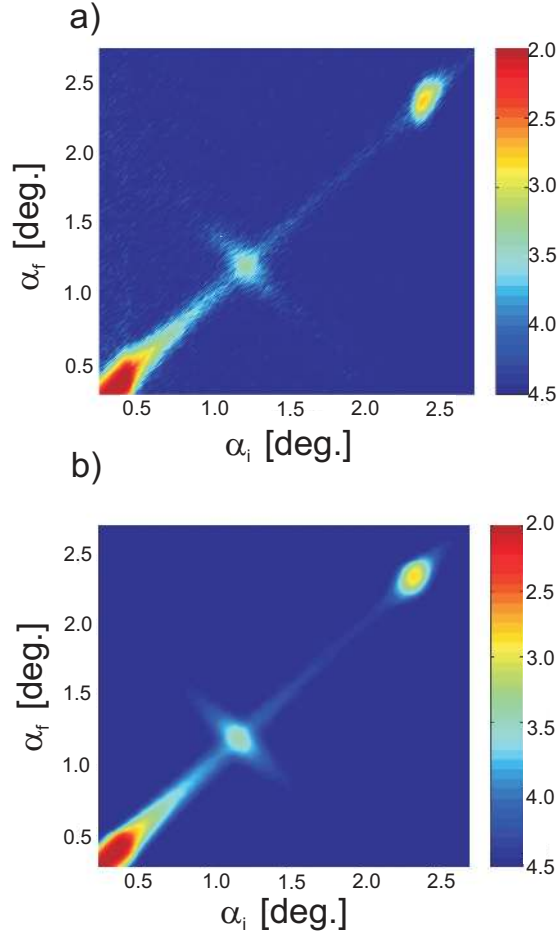Figure 7.21.: (a) 2D map of the neutron intensity scattered from the af coupled [Co$_2$MnGe(3nm)/V(3nm)]$_{50}$ (#1) multilayer in zero applied field at 15 K. The Bragg sheet at the af peak is purely of magnetic ordering. The centered intensity is the first order structural peak. (b) The simulation of the corresponding map within a super-iterative based version of the Distorted Wave Born Approximation.

ignoring their crystalline structure and possible large-scale inhomogeneities. Fig. 7.20 shows a transverse scan of the [Co$_2$MnGe(3nm)/V(3nm)]$_{50}$ (#1) multilayer measured in zero field at 15 K at the position of the af peak. The presence of magnetic off-specular scattering indicates that the magnetization in the single layers is broken up into domains, the size of which being smaller than the longitudinal projection $L_{\parallel} \sim L/\sin\alpha$ of the neutron coherence length $L \approx 1/\Delta Q$, where ΔQ is the uncertainty in the wave vector value due to experimental resolution. The longitudinal projection of the lateral coherence length is estimated to be about 60 μm, while the transverse coherence length (perpendicular to the reflection plane), $L_{\perp} \sim L$, is only a few nm due to the focussing condition of the monochromator. Remarkably is the fact that in the transverse scan
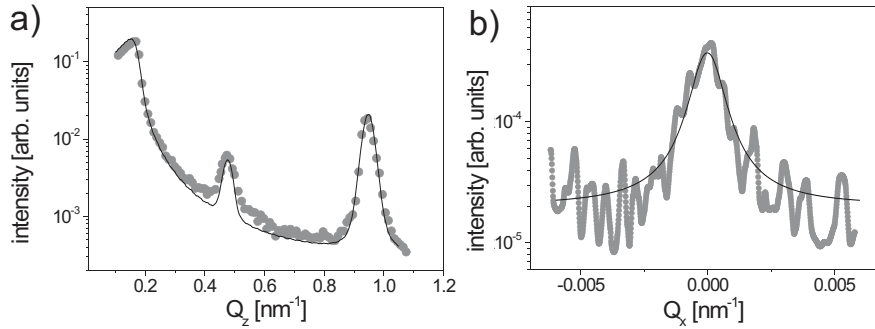
Figure 7.22.: (a) Cut along the specular line of the 2D map shown in Fig. 7.21 and (b) a Q_x cut at the position of the half-order peak. The measured data is denoted by circles, the simulation is given by the solid line.

through the af peak no resolution limited Gaussian profile is apparent, and in contrast to the structural Bragg peak, that the af scan can well be fitted by a Lorentzian line shape. This gives a strong hint that the af peak on the specular reflectivity line is mainly due to a contribution of off-specular scattering to the specular reflection within the range of their overlap. Hence, being simulated with the model given above and assuming only specular reflectivity leads to a false result for this sample. Therefore quantitative evaluation of both, PNR and off-specular scattering, collected over a broad range of incidence and scattering angles is required for a realistic description of the present system. Fig. 7.21 depicts an unpolarized 2D $\alpha_i - \alpha_f$ map of the scattering intensity of the $[Co_2MnGe(3nm)/V(3nm)]_{50}$ (#1) multilayer in zero field measured at 15 K together with a simulation. The specular ridge with the first order nuclear Bragg peak, as well as the Bragg sheet crossing the reflectivity ridge at the half-order Bragg peak position can be observed.

To achieve a good fit quality we simulated the map and directly compared the cut along the specular line and a vertical cut at the position of the af peak with the measured data (see Fig. 7.22). Simultaneously we provided spin polarized simulations of the off-specular data using the same fitting parameters as for the unpolarized case and compared the reflectivity cuts through the maps with the measured polarized reflectivity scans (see Fig. 7.23).

The maps were simulated within a super-iterative based version of the Distorted Wave Born approximation (DWBA) [148, 209]. The underlying model has the following fit parameters: the lateral domain size ξ, the depth correlation factor n_0 giving the out-of-plane (af)correlation length, the mean value $\langle \cos \varphi \rangle$ determining mean magnetization averaged over lateral domains in the coherence area, $\Delta\varphi$, giving deviations of domain magnetization vectors from the mean magnetization direction.
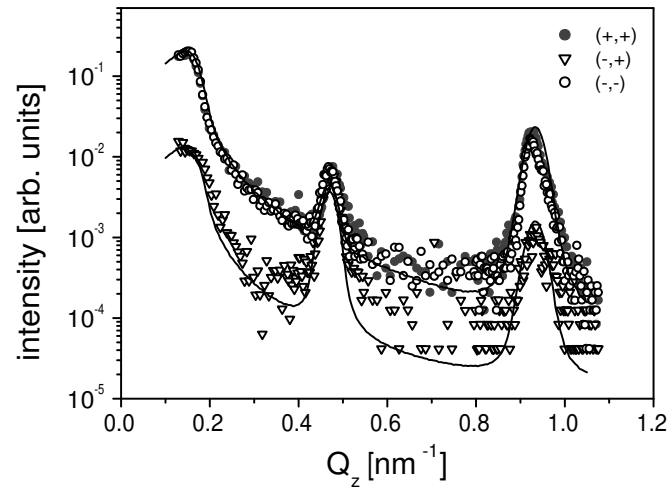
Figure 7.23.: PNR scan of the sample [Co₂MnGe(3nm)/V(3nm)]₅₀ (#1) together with a simulation. The simulated polarized reflectivity scans represent cuts along the specular line of polarized 2D maps calculated within the Distorted Wave Born approximation.

As the result from the numerical simulation we get the microscopic picture of small, completely coherent columnar domains with alternating angle $\Delta\varphi = 45°/225°$ and a lateral domain size of 2.1 μm. The sample breaks up into a Landau type of pattern [210] with four possible types of domains with perfect antiferromagnetic coupling (see Fig. 7.24). From fits to the transverse scans at the position of the half-order af peaks
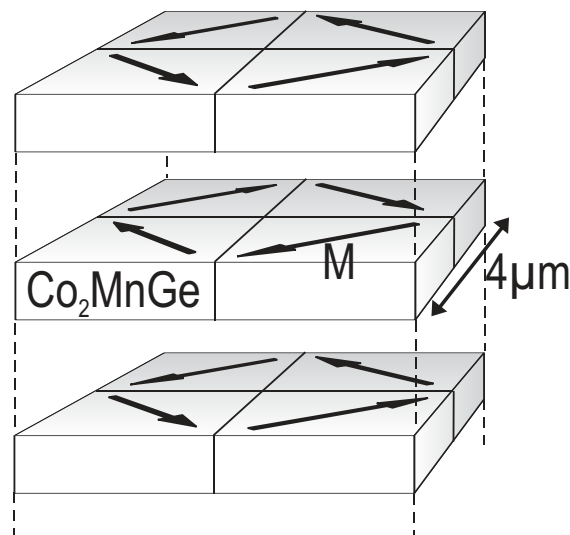

Figure 7.24.: Sketch of the microscopic picture for the antiferromagnetic state of the sample [Co₂MnGe(3nm)/V(3nm)]₅₀ (#1) with four different types of domains.

taken at different temperatures we extracted the temperature dependence of the domain sizes. All Q_x scans could well be fitted within the framework of the Born approximation by a Lorentzian line shape. Fig. 7.25 clearly shows that the size of the af domains increases with increasing temperature from 2.1 μm at 15 K to 3.2 μm at 300 K.
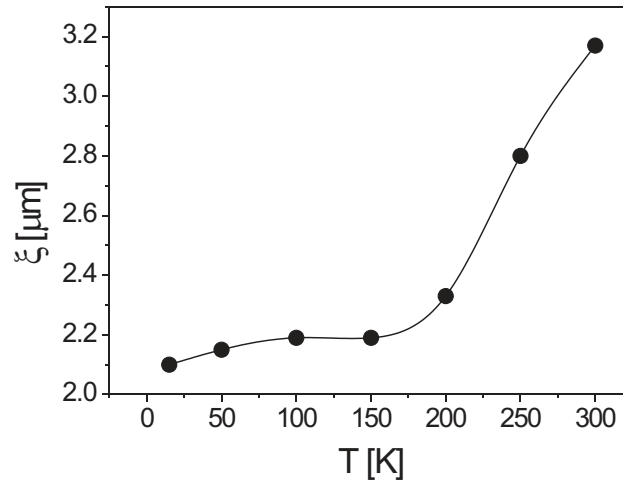

Figure 7.25.: Size of the antiferromagnetically coupled domains in the $[Co_2MnGe(3nm)/V(3nm)]_{50}$ (#1) multilayer versus temperature.

For the multilayer with $t_V = 2$ nm the situation is quite different, although this sample equally shows the transverse antiferromagnetic ordering and lateral domains. Similar to the previous case, essentially no splitting of the NSF cross sections at the structural first order peak is apparent, i.e. no ferromagnetic contribution to the first order peak in the magnetic ground state exists. But in this case, there is also no intensity in the SF channel apart from a very small peak at the position of the af peak, caused by not 100% efficiency of the polarizing elements. The multilayer seems to be nearly perfectly af aligned with the sublattice magnetizations collinear with the guiding field. The collinear arrangement is, in fact, not very surprising, since it turned out that a growth induced uniaxial magnetic anisotropy for the measurements in Fig. 7.19(a) is parallel to the direction of the external field. A relatively low guiding field for the neutron polarization does not cause a spin-flop transition into the state with the magnetization direction perpendicular to the field [211].

In contrast to the previous case, Q_x scans through the af peak show a resolution limited Gaussian line shape for the specularly reflected beam. The latter is superimposed onto an almost flat background of diffuse scattering (not shown here). This indicates the presence of antiferromagnetic ordering on a scale bigger than the neutron coherence length simultaneously with the magnetization fluctuations on a shorter length scale.

Unfortunately neither of those scales can immediately be determined from the data: the specular peak width gives just a lower limit (60 μm) for the long-range af order, while af fluctuations contributing to diffuse scattering are too small in size to be deduced from the line shape analysis of off-specular scattering, as the range of the lateral moment transfer is restricted.

On the other hand, the diffuse intensity contribution at the position of the specular reflection is small with respect to the Gaussian component. This justifies the fitting procedure of the reflectivity line in Fig. 7.19(a) described above and proves the values of the deduced physical parameters for this sample. The reduction of the sublayer magnetization values is due to the averaging of the layer magnetization over lateral domains within the coherence range. A domain configuration which can explain our observations for this sample is sketched in Fig. 7.26. Again, the data suggest that in each of the lateral and columnar-like domains the magnetization of the sublayers alters sign across the multilayer stack. However, now one can distinguish between two kinds of domains. The main set of relatively large domains separated by 180° domain wall mostly cause non-spin-flip specular reflection, as the domain magnetization is collinear with the guiding field for the neutron polarization. The size of those domains allows a few of them to be simultaneously illuminated coherently. Namely this coherent averaging reduces the effective magnetic optical potential, while fluctuations around its mean value contribute in non-spin-flip diffuse scattering. The other set of so called 'closure' small domains [210] cause a diffuse background of spin-flip scattering. In the present experiments
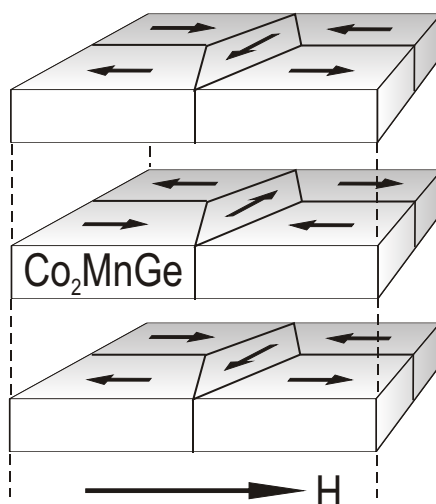

Figure 7.26.: Sketch of the microscopic picture for the antiferromagnetic state of the sample [Co$_2$MnGe(3nm)/V(2nm)]$_{50}$ with two kinds of domains: large domains separated by 180° domain walls and 'closure' domains.

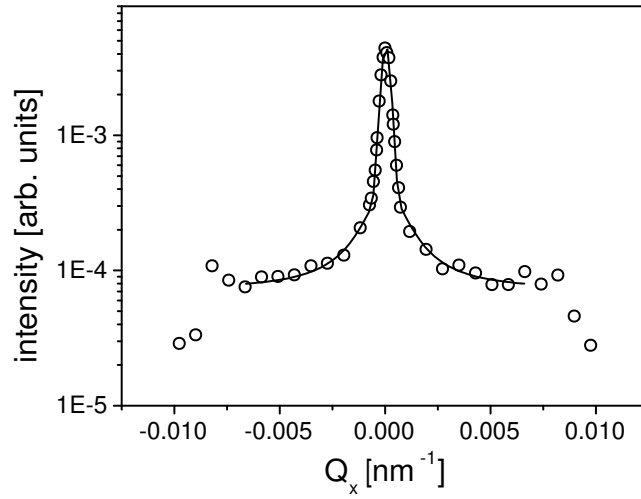Figure 7.27.: Neutron transverse scan of the $[Co_2MnGe(3nm)/V(2.5nm)]_{50}$ sample at the position of the half-order Bragg peak (dots) together with a fit (line). The diffuse background exhibits a Lorentzian line shape.

polarization analysis of diffuse scattering was not possible. Therefore, the contribution of the closure domains to the off-specular scattering cannot be determined unambiguously.

The specular PNR data for the multilayer $[Co_2MnGe(3nm/V(2.5nm)]_{50}$ is very similar to the previous case, i.e. there is no ferromagnetic contribution to the first order peak and no spin-flip scattering intensity after correction for efficiency of the polarizing elements. Thus the multilayer seems to be perfectly af aligned with the sublattice magnetization collinear with the neutron guide field. Q_x scans at the position of the af peak reveal a resolution limited Gaussian line shape for the specular reflected beam superimposed onto a background of diffuse intensity, exhibiting a Lorentzian line shape (see Fig. 7.27). In this sense the sample with $t_V = 2.5$ nm represents an intermediate case between the multilayers discussed above. Without polarization analysis of the off-specular scattering the microscopic picture for the antiferromagnetic state is difficult to draw. A domain formation similar to the previous case with a higher degree of random patterns can well explain the measured data.

Remagnetization Process

To get insight into the remagnetization process in this system, a detailed study of diffuse scattering is not required. Instead, it is sufficient to carry out corresponding fits for the specular reflectivity curves. The latter were measured on the $[Co_2MnGe(3nm)/V(2nm)]_{50}$ and $[Co_2MnGe(3nm)/V(2.5nm)]_{50}$ multilayer at different fields at 10 K. Two representative field dependent PNR measurements with an applied

field of $H = 70$ Oe and $H = 350$ Oe are plotted in Fig. 7.28 together with model simulations. To account for the limited available beamtime, the curves were measured only in the region of the af peak and the structural peak. The intensity around the edge of total reflection is adjusted to the intensity of the polarized reflectivity scans in Fig. 7.19. To ensure a well defined magnetic state, the samples have been saturated at room temperature and cooled down in zero-field. The results of the fit are summarized in Fig. 7.29,
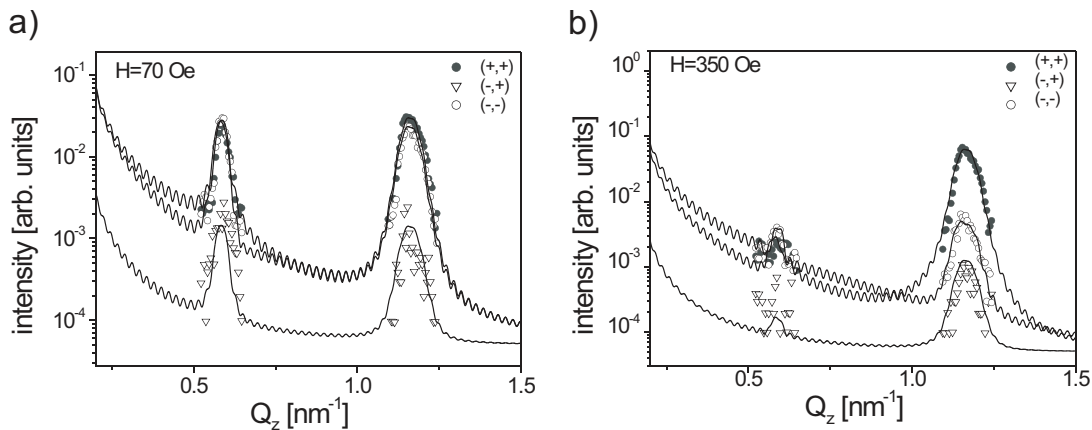

Figure 7.28.: PNR measurements of the multilayer $[Co_2MnGe(3nm)/V(2nm)]_{50}$ as a function of the applied field together with model simulations.

where the field dependence of the antiferromagnetic, $(m_1 - m_2)/2$, and ferromangnetic, $(m_1 + m_2)/2$, order parameters is depicted. The qualitative behaviour of both samples is very similar. With increasing field the af order parameter continuously decreases and is nearly completely suppressed at $H = 350$ Oe and $H = 500$ Oe, respectively. On the contrary, the ferromagnetic order parameter, almost vanishing in zero field, increases continuously reaching the value expected for ferrromagnetic saturation at these fields.

Remembering that these samples have an antiferromagnetic configuration collinear with the applied field, one should expect some scattering intensity in the spin-flip channel, if the system would undergo a spin-flop transition and approaches the saturation via rotation of the sublattice magnetization. Surprisingly however, the remagnetization process is quite different. There is no resolvable spin-flip scattering over the entire magnetic field range (Fig. 7.30) indicating that the remagnetization takes place solely by domain wall movements for domains in the sublayer with the magnetization direction opposite to the applied field. From the upper panel in Fig. 7.30 it follows that the af order parameter continuously degrades as the intensity of the half-order af reflection decreases. Simultaneously the increasing ferromagnetic order parameter manifests itself in the splitting of the $(++)$ and $(--)$ channel intensities (lower panel in Fig. 7.30). At saturation the $(--)$ channel exhibits nearly zero intensity. This is a special features of

a)

b)
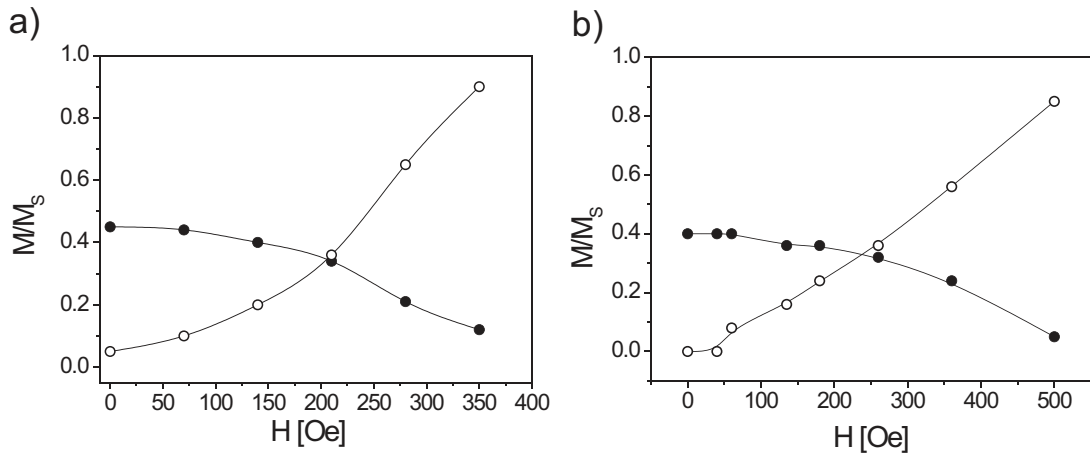
Figure 7.29.: Field dependence of the antiferromagnetic, $(m_1 - m_2)/2$ (filled circles), and ferromangnetic, $(m_1 + m_2)/2$ (open circles), order parameters for the sample $[Co_2MnGe(3nm)/V(2nm)]_{50}$ (a) and $[Co_2MnGe(3nm)/V(2.5nm)]_{50}$ (b) measured at 10 K.

several Heusler alloys, which has been used for the construction of neutron polarizers [212].

Fig. 7.31 shows the field dependence of the af peak intensity of the $[Co_2MnGe(3nm)/V(3nm)]_{50}$ multilayer taken at 15 K and 150 K. At 15 K the af peak intensity is not restored after switching off the field, whereas at 150 K about 30% of
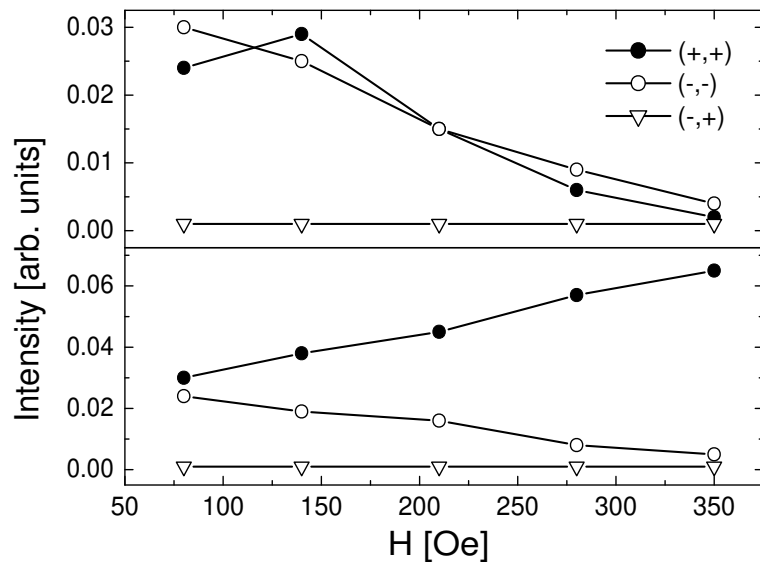
Figure 7.30.: Field dependence of the af peak intensity (upper panel) and first order structural peak (lower panel) for the spin-flip $(-+)$ and non-spin-flip $((++)$ and $(--))$ channels for the multilayer $[Co_2MnGe(3nm)/V(2nm)]_{50}$ at 10 K.

the af peak intensity is recovered. The af coupling is apparently very weak at 150 K, a field of about 50 Oe already destroys the af order. For antiferromagnetically coupled multilayers the effective coupling energy J can be estimated by the formula [213]

$$J = M_{\mathrm{S}}t_{\mathrm{Heusler}}H_S/4, \tag{7.2}$$

where M_{S} is the saturation magnetization, t_{Heusler} the thickness of a single Co_2MnGe layer and H_{S} the ferromagnetic saturation field. The values obtained by Eq. (7.2) are $J = 6.8 \times 10^{-7}$ J/m², $J = 9.3 \times 10^{-7}$ J/m² and $J = 1.1 \times 10^{-6}$ J/m² for the $[Co_2MnGe(3nm)/V(t_{\mathrm{V}})]_N$ multilayers with $t_{\mathrm{V}} = 2$ nm, 2.5 nm and 3.0 nm, respectively. Compared to typical values for e.g. Co/Cu superlattices of the order of 10^{-4} J/m², the coupling strength in our samples is very weak [214]. The temperature dependence of
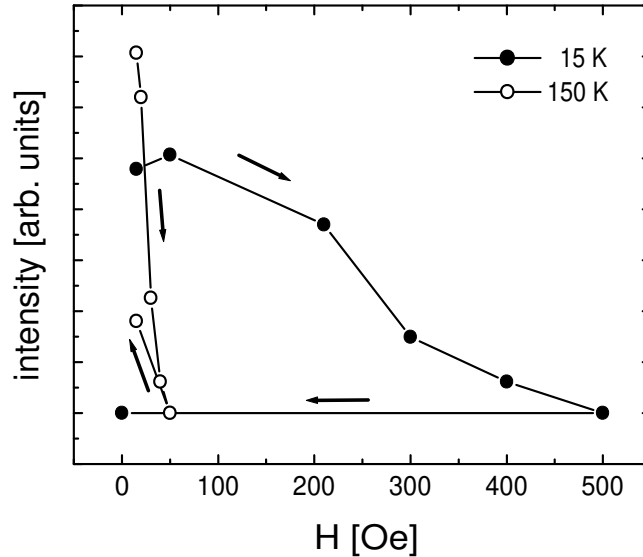
Figure 7.31.: Field dependence of the af peak intensity of the $[Co_2MnGe(3nm)/V(3nm)]_{50}$ (#2) multilayer taken at $T = 15$ K (solid dots) and $T = 150$ K (open dots).

the af peak intensity for the $[Co_2MnGe(3nm)/V(3nm)]_{50}$ multilayer as measured after cooling in zero-field and after cooling in a field of 1000 Oe and then switching off the field at the measuring temperature is displayed in Fig. 7.32 as a representative example. After zero-field cooling the af peak intensity develops below 250 K in a phase transition like fashion, reaches a maximum at about 150 K and decreases slightly towards lower temperatures. After cooling in a field of 1000 Oe there is no detectable af peak intensity below 100 K, but approaching the phase transition at $T_N = 250$ K, the af order recovers after switching off the field. Close to the transition temperature the peak

intensity coincides with that measured after zero-field cooling. Since the half-order peak intensity is proportional to the squared sublattice magnetization in an antiferromagnet, this behavior clearly reveals a reversible phase transition at 250 K. Remarkably this temperature is far below the ferromagnetic ordering temperature of a single Co_2MnGe film of comparable thickness, which is about 600 K [194].
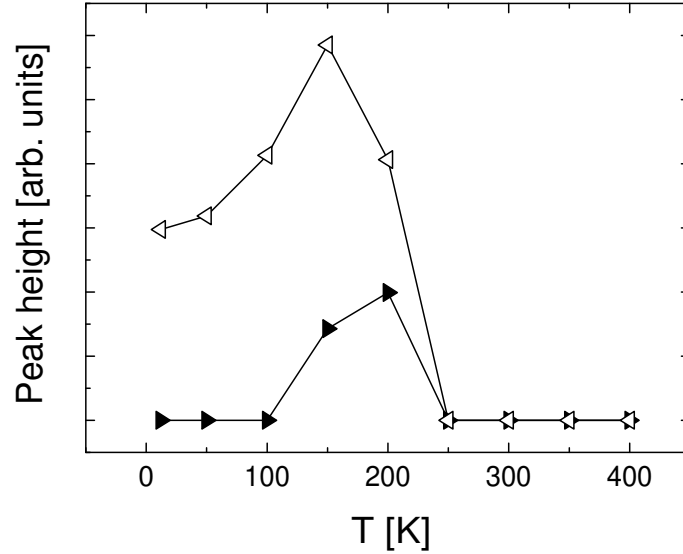
Figure 7.32.: Temperature dependence of the af peak intensity of the multilayer $[Co_2MnGe(3nm)/V(3nm)]_{50}$ (#1) measured after field cooling (solid triangles) and zero field cooling (open triangles).

7.4. Magnetic Phase Diagram

The neutron scattering results of the previous section clearly prove that in the $[Co_2MnGe/V]$ multilayers there is antiferromagnetic interlayer ordering in the thickness range $t_V \leq 3$ nm. The Néel temperature derived from the peak in the susceptibility and the vanishing intensity of the half-order peak are combined in a magnetic phase diagram in Fig. 7.33. The Néel temperature decreases continuously with increasing thickness of the V layers. There is no indication of an oscillatory character of the magnetic coupling. We have confirmed for additional intermediate thicknesses by magnetization measurements that the interlayer ordering is always antiferromagnetic. Actually the magnetic state of the $[Co_2MnGe/V]$ multilayers above the Néel temperature is not simply paramagnetic but exhibits superparamagnetic properties. In Fig. 7.34 the reversible magnetization of the $[Co_2MnGe(3nm)/V(3nm)]_{50}$ multilayer for temperatures above T_N
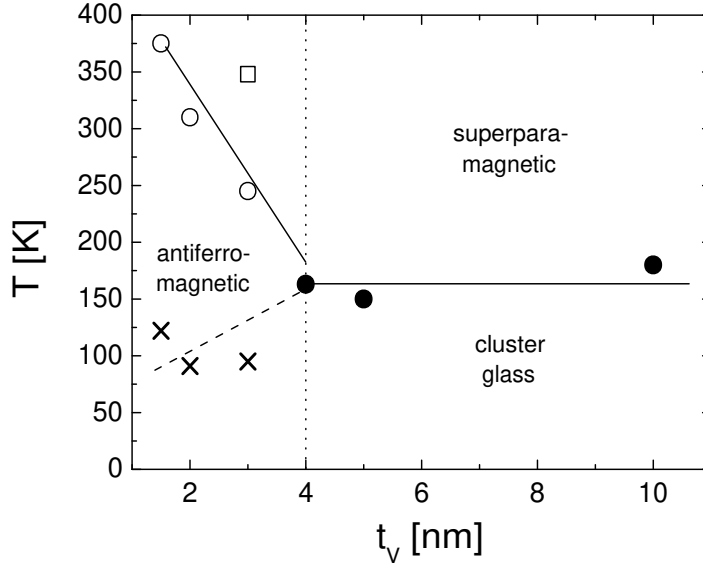
Figure 7.33.: Magnetic phase diagram for multilayers $[Co_2MnGe(3nm)/V(t_V)]_{50}$ as a function of the V thickness t_V with the Néel temperature (open circles) and cluster glass temperature (filled circles). The open square designs T_N for the sample $[Co_2MnGe(3nm)/V(3nm)]_{50}$ (#2), (see Tab. 7.1). The crosses indicate the onset of a strong magnetic irreversibility.

is depicted. The magnetization curves reveal typical superparamagnetic behavior with a linear $M(H)$-curve at low fields and saturation at higher fields. For non-interacting superparamagnetic clusters the magnetization should scale as [116]

$$M(H,T) = N_c\mu_c\mathcal{L}(\frac{\mu_c H}{k_b T}),\qquad(7.3)$$

with the number of magnetic clusters N_c, the cluster magnetic moment μ_c and the Langevin function $\mathcal{L}(x)$. Experimentally the magnetization isotherms fall progressively below the commonly supposed Langevin function. Essentially we attribute this behaviour to cluster interactions [215] and to anisotropy of the clusters [216]. Furthermore the clusters probably exhibit a size distribution leading to deviations from Eq. (7.3). More sophisticated models taking these effects into account were applied, but could not reproduce the magnetization curves either. Thus we used the low field approximation $\mathcal{L}(x) \approx 1/3x$, which yields the magnetization

$$M(H,T) = \frac{N_c\mu_c^2 H}{3k_b T}.\qquad(7.4)$$
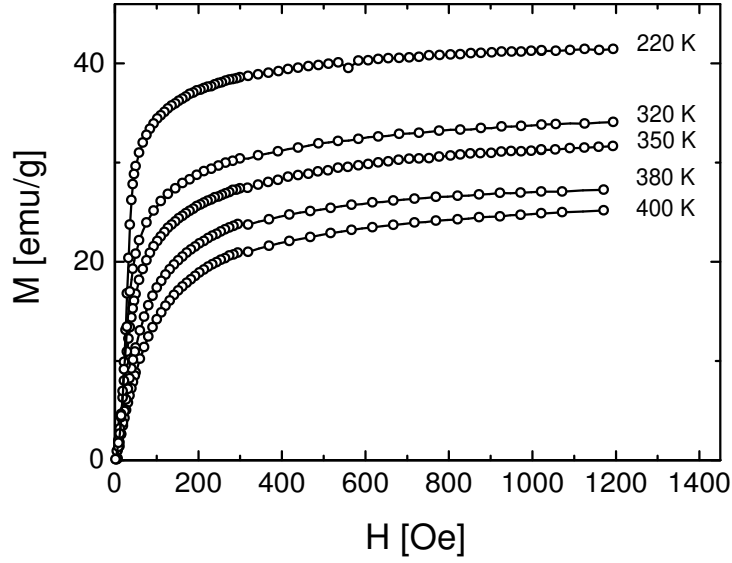
Figure 7.34.: Magnetization curves of the multilayer $[\mathrm{Co_2MnGe(3nm)/V(3nm)}]_{50}$ (#1) measured at different temperatures T given in the figure.

Fitting Eq. (7.4) to the $M(H,T)$ curves in Fig. 7.34 we derive a cluster moment of $1.6 \times 10^5 \; \mu_B$ at 400 K. At 250 K just above the Néel temperature we get $\mu_c = 4 \times 10^5 \; \mu_B$. This magnetic moment corresponds to 7×10^5 or 2×10^6 $\mathrm{Co_2MnGe}$ formula units combining one cluster and gives an average dimension of 120×120 nm^2 and 200×200 nm^2 for the lateral cluster size, respectively. The superparamagnetic cluster type of behaviour is similar for all multilayers of the present study. In Fig. 7.35 we compare the temperature development of the superparamagnetic cluster moments for the thickness $t_V = 3$ nm and $t_V = 4$ nm, where only the former compound orders antiferromagnetically. The temperature dependence of the cluster moment indicates that the clusters are not independent, but show interaction [116]. Thus the antiferromagnetic interlayer magnetic ordering in the $[\mathrm{Co_2MnGe/V}]$ multilayers develops from a superparamagnetic state and not from a conventional paramagnetic state. An interesting question concerns the magnetic order of the samples with $t_V \geq 4$ nm, which do not exhibit an antiferromagnetic interlayer order. Here one finds all ingredients of a cluster glass transition at a transition temperature T_f. Below T_f the coercive force strongly increases (Fig. 7.36), which can approximately be described by $H_c \propto H_0 e^{-\alpha T}$. The onset of strong irreversibility in the low field susceptibility occurs below the cluster glass transition temperature $T_f \approx 150$ K [217, 111]. The rectangular hysteresis loops at these temperatures suggest cooperative behavior among a large number of clusters [112]. We have included the cluster glass transition temperature T_f in the phase diagram of Fig. 7.33. It is essentially independent of the thickness
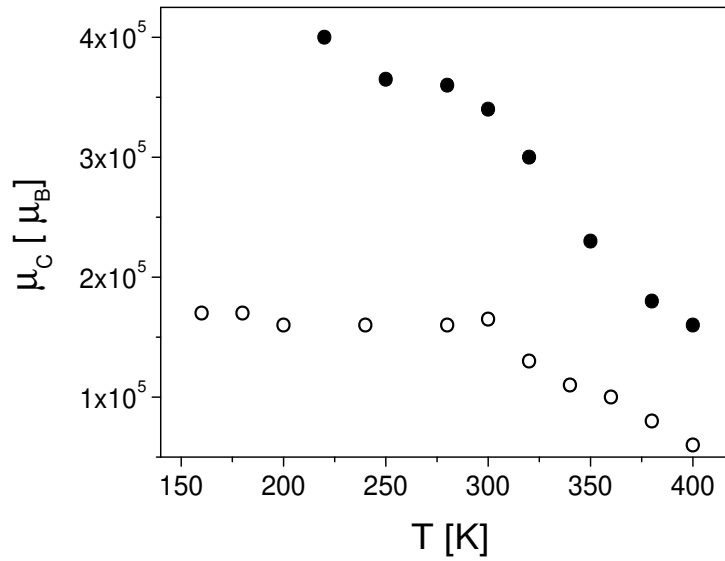
Figure 7.35.: Temperature dependence of the cluster magnetic moment μ_C for the [Co$_2$MnGe(3nm)/V(3nm)]$_{50}$ (#1) multilayer (filled circles) and the [Co$_2$MnGe(3nm)/V(4nm)]$_{50}$ multilayer (open circles).

t_V. The cluster glass transition continues below the antiferromagnetic phase transition line (see dashed line in Fig. 7.33), where it characterizes the onset of strong magnetic irreversibility below T_N. This line resembles the reentrance phase transition line which is found in conventional spin glass systems close to the critical concentration of long
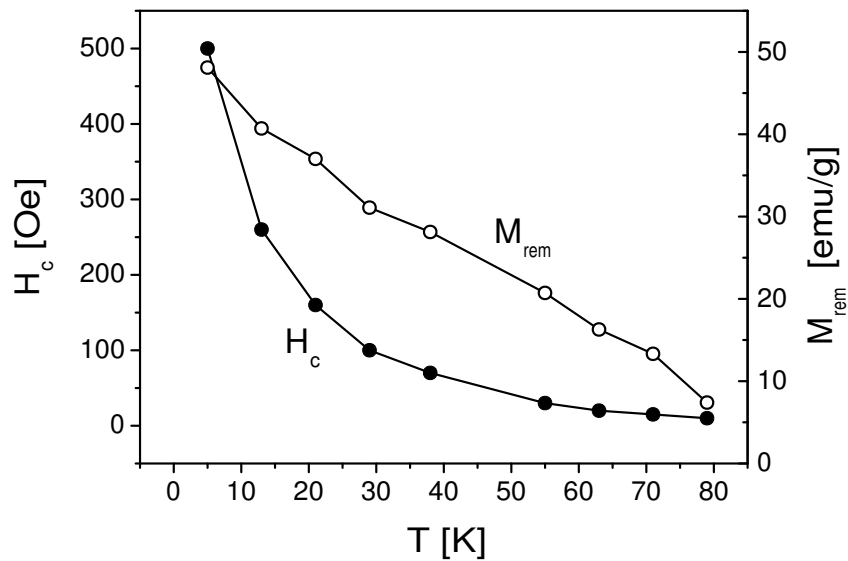
Figure 7.36.: Coercive field (solid circles) and remanent magnetization (open circles) versus temperature for the multilayer [Co$_2$MnGe(3nm)/V(3nm)]$_{50}$ (#1).

range order [101]. This line is usually discussed in terms of the coexistence of both, the short and the long-range order parameters at low temperatures.

7.5. Discussion

We now discuss the microscopic origin leading to the peculiar magnetic phase diagram in Fig. 7.33. There are two essential ingredients one has to explain. The first is the origin of the cluster type magnetism, which is most obvious in the superparamagnetic behaviour at high temperatures, and in the cluster glass transition at low temperatures. Second, the question concerning the magnetic interactions causing the formation of the antiferromagnetic interlayer ordering needs to be clarified.

The magnetic cluster type behaviour is related to the crystalline microstructure of the single Co_2MnGe layers in the multilayer. We have shown in Chap. 6 that a single 3 nm thick Co_2MnGe layer embedded between two V layers exhibits typical small particle ferromagnetism with a ferromagnetic hysteresis loop virtually identical for the magnetic field applied perpendicular and parallel to the film plane, although the surface of the magnetic film is atomically flat [74]. The reason for this cluster type of ferromagnetism is that the very small crystalline grains in the Co_2MnGe film are magnetically decoupled at the grain boundaries which are chemically disordered and weakly ferromagnetic. A superparamagnetic high temperature state is the natural consequence of small particle magnetism, if the interactions between the clusters are weak and the magnetic anisotropy is small. In contrast, in a single Co_2MnGe thin film grown on a V seed layer we did not observe superparamagnetism in the temperature range up to the maximum experimental temperature of 400 K.

In the [Co_2MnGe/V] multilayers with the same thickness of the magnetic layers, however, superparamagnetic behavior already exists at room temperature, probably due to a slightly different microstructure and a larger topological roughness of the Co_2MnGe layers. Thus alloying and roughening at the interfaces and atomic disorder at the grain boundaries cause the Co_2MnGe layers in the multilayers to break up into weakly coupled magnetic clusters. The mean grain size of the crystallites in the multilayers as determined from the off-specular x-ray reflectivity is about 20 nm. The average lateral magnetic cluster size we derived from the superparamagnetic moment just above T_N is of the order of 200 nm i.e. one magnetic cluster is combined of many crystalline grains. In the antiferromagnetically ordered phase we determined an average lateral size for the magnetic domains of several μm. Thus, in the antiferromagnetically ordered state many magnetic clusters within one Co_2MnGe layer belong to one magnetic domain.

7. [Co$_2$MnGe/V]$_N$ Multilayers

Concerning the magnetic interactions responsible for the antiferromagnetic interlayer magnetic ordering, we can exclude interlayer exchange coupling. Non-ferromagnetic interfaces and thickness fluctuations seem to weaken the IEC coupling drastically. We are thus led to the conclusion that the dipolar interactions between the planes cause the antiferromagnetic interlayer ordering. This would explain the absence of an oscillatory character of the interlayer coupling and the weak antiferromagnetic coupling field. Actually dipolar stray fields protruding at the grain boundaries are a natural consequence of the internal granular structure of the Co$_2$MnGe films. The influence of the dipolar fields from neighbouring layers also explains the anisotropy, existing in the [Co$_2$MnGe/V]$_N$ multilayers, although the single thin Co$_2$MnGe films are isotropic. In Fig. 7.37 we have drawn schematically, how interlayer dipolar interactions may arrange the antiferromagnetic interlayer order in the [Co$_2$MnGe/V] multilayer system. The im-
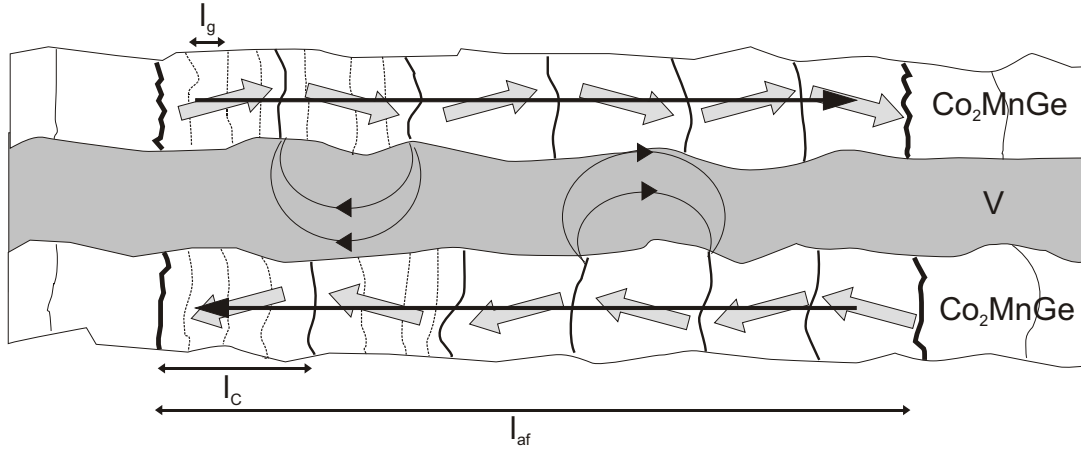
Figure 7.37.: Schematic picture of the interlayer order in the [Co$_2$MnGe(3nm)/V(t_V)]$_N$ multilayers. The size of the crystallites is about $l_g = 20$ nm, the average magnetic cluster size is of the order $l_c = 200$ nm and the size for the magnetic domains l_{af} is of several μm. The arrows indicate the direction of the local magnetization.

portance of interlayer dipolar interactions in multilayer systems is well established in the literature. Theoretical model calculations show that the dipolar coupling in multilayers can be ferromagnetic or antiferromagnetic, depending on the interface topology [218, 219, 220, 221]. In a system with corrugated interfaces the so called 'orange peel' coupling [222] may give rise to a ferromagnetic interlayer coupling. For the case of uncorrelated roughness, antiferromagnetic coupling is more probable [219]. Experimentally an antiferromagnetic interlayer ordering induced by dipolar interactions has been observed in [Co/Cu] multilayers with 6 nm thick Cu layers [221]. In multilayer systems [Nb/Fe] and [FeNi/Ag], af interlayer order due to dipolar interactions has also been discussed

[223, 224]. However, at variance to the system studied here, none of these multilayers exhibits a reversible af phase transition and a superparamagnetic state above the Néel temperature.

7. *[Co$_2$MnGe/V]$_N$ Multilayers*

8. Summary and Conclusions

Within the framework of this thesis a detailed study of the structural and magnetic properties of single thin Co_2MnGe films and $[Co_2MnGe/V]_N$ multilayers with different thickness of the V layers has been presented. In the multilayers a new magnetic ordering phenomenon has been found.

The investigations on single films have shown that thick films of the Heusler compound Co_2MnGe can be grown with a saturation magnetization and structural quality comparable to bulk samples. However, when decreasing the thickness to the order of 3 nm, the films show a definitely lower value of the saturation magnetization and exhibit properties reminiscent of small particle ferromagnets. This behaviour is interpreted by a magnetic decoupling of the Heusler films at the grain boundaries of the very small grains forming the film. Structural disorder and a high concentration of antisite defects at the grain boundaries weaken the ferromagnetism drastically.

As it has been demonstrated by the XMCD measurements on a single Co_2MnGe film at the Mn and the Co $L_{2,3}$ absorption edges, it is only the Mn atom in the Heusler compounds which reduces the saturation magnetization. Theoretical model calculations suggest that this originates from an antiparallel spin orientation of antisite Mn spins rather than from a loss of the atomic magnetic moment of Mn.

Based on the study of the single Heusler films a series of $[Co_2MnGe/V]_N$ multilayers has been prepared and analyzed with special emphasis on their interface properties and their magnetic ordering phenomenon.

X-ray scattering revealed a high structural quality of the multilayers with smooth interfaces exhibiting mainly uncorrelated roughness. The ferromagnetic saturation magnetization of the Co_2MnGe layers in the multilayer system is found to be reduced to about 50% of the bulk value.

In order to examine the magnetization at the interfaces, depth resolved magnetic moment density profiles for Co and Mn have been derived by simulations of XRMS spectra measured at the Co and Mn $L_{2,3}$ edges. The profiles clearly reveal the existence of non-ferromagnetic or weakly ferromagnetic Co_2MnGe layers at the interface with a

8. Summary and Conclusions

thickness of about 0.5 nm at the bottom and 0.3 nm at the top. This phenomenon can be attributed to a gradual transition of the metallurgical order in the Co_2MnGe film from a disordered bcc phase at the interface to the well ordered $L2_1$ phase in the core of the layer, taking into consideration that the Mn moments are more effected by disorder than the Co moments.

Neutron reflectivity and magnetization measurements have led to the detection of a peculiar antiferromagnetic interlayer magnetic ordering in the $[Co_2MnGe/V]$ multilayers with a well defined Néel temperature far below the ferromagnetic Curie temperature of a single Heusler layer of the same thickness. The antiferromagnetic ordering exists in the thickness range of the V interlayer between 1 nm and 3 nm, very unlike the antiferromagnetic interlayer order in multilayer systems coupled by the interlayer exchange mechanism. The antiferromagnetic order is directly related to the granular ferromagnetic structure of very thin Heusler layers. The small ferromagnetic particles defined by the weak magnetic coupling at the grain boundaries exhibit superparamagnetic behaviour above the Néel temperature. The interlayer dipolar interactions between the superparamagnetic particles cause a reversible magnetic phase transition with antiferromagnetic order between the layers and ferromagnetic order within the layers at a well defined Néel temperature.

Finally, simulations of specular and diffuse polarized neutron scattering allowed to draw a microscopic picture of the antiferromagnetic domain distribution within the $[Co_2MnGe/V]_N$ multilayers. It turns out that the antiferromagnetic columnar domains exhibit a Landau type of pattern. Furthermore the antiferromagnetic ordering seems to be perfectly correlated through the whole multilayer stack.

Regarding the perspective of the Heusler compounds as full spin polarized ferromagnetic layers in magnetoelectronic devices, the results above indicate the severe difficulties one inevitably encounters. The constraints in the preparation of thin film heterostuctures in many cases prohibit the optimum preparation conditions for the Heusler phase, thus rendering it difficult to get the $L2_1$ structure with a high degree of atomic order. At the interfaces additional problems arise since they tend to be strongly disordered and weakly ferromagnetic. However, these problems could be overcome by a Heusler phase with a more robust spin polarization at the Fermi level, which principally might already exist among the many new Heusler half-metals which have been predicted theoretically. In any case, the Heusler alloys still offer new and promising perspectives for basic research and applications.

Bibliography

[1] G.A. Prinz. *Science*, 282:1660, 1998.

[2] D. Awschalom and J. Kikkawa. *Physics Today*, 52:33, 1999.

[3] J.F. Gregg, I. Petey, E. Jougelet, and C. Dennis. *J. Phys. D: Appl. Phys.*, 35:R121, 2002.

[4] R. J. Soulen, J. M. Byers, M. S. Osofsky, B. Nadgorny, T. Ambrose, S. F. Cheng, P. R. Broussard, C. T. Tanaka, J. Nowak, J. S. Moodera, A. Barry, and J. M. D. Coey. *Science*, 282:85, 1998.

[5] A. Stroppa, S. Picozzi, A. Continenza, and A.J. Freeman. *Phys. Rev. B*, 68:155203, 2003.

[6] H. Akai. *Phys. Rev. Lett.*, 81:3002, 1998.

[7] I. Galanakis, P. H. Dederichs, and N. Papanikolaou. *Phys. Rev. B*, 66:174429, 2002.

[8] I. Galanakis, P. H. Dederichs, and N. Papnikolaou. *Phys. Rev. B*, 66:134428, 2002.

[9] C. Felser, B. Heitkamp, F. Kronast, D. Schmitz, S. Cramm, H. A. Dürr, H-J. Elmers, G. H. Fecher, S. Wurmehl, T. Block, D. Valdaitsev, S. A. Nepijko, A. Gloskovskii, G. Jakob, G. Schönhense, and W. Eberhardt. *J. Phys.: Condens. Matter*, 15:7019, 2003.

[10] S. Picozzi, A. Continenza, and A. J. Freeman. *Phys. Rev. B*, 69:094423, 2004.

[11] M. P. Raphael, B. Ravel, Q. Huang, M. A. Willard, S. F. Cheng, B. N. Das, R. M. Stroud, K. M. Bussmann, J. H. Claassen, and V. G. Harris. *Phys. Rev. B*, 66:104429, 2002.

[12] C.T. Tanaka, J. Nowak, and J.S. Moodera. *J. Appl. Phys.*, 86:6239, 1999.

Bibliography

[13] Y. Sakuraba, J. Nakata, M. Oogane, H. Kubota, Y. Ando, A. Sakuma, and T. Miyazaki. *Japan. J. Appl. Phys.*, 44:L1100, 2005.

[14] M. Oogane, Y. Sakuraba, J. Nakata, Y. Ando, A. Sakuma, and T. Miyazaki. *J. Phys. D: Appl. Phys.*, 39:834, 2006.

[15] S. Ishida, T.Masaki, S. Fujii, and S. Asano. *Physica B*, 245:1, 1998.

[16] I. Galanakis. *J. Phys.: Condens. Matter*, 14:6329, 2002.

[17] U. Geiersbach, A. Bergmann, and K. Westerholt. *Thin Solid Films*, 425:226, 2003.

[18] P. Bruno. *Phys. Rev. B*, 52:411, 1995.

[19] D. Gibbs, D. R. Harshman, E. D. Isaacs, D. B. McWhan, D. Mills, and C. Vettier. *Phys. Rev. Lett.*, 61:1241, 1988.

[20] J. P. Hannon, G. T. Trammel, M. Blume, and D. Gibbs. *Phys. Rev. Lett.*, 61:1245, 1988.

[21] F. Heusler. *Verh. Dtsch. Phys. Ges.*, 5:219, 1903.

[22] P. J. Ziebeck and K. R. A. Webster. *Landolt-Börnstein New Series III/19c*, 1986.

[23] S. Ishida, S. Fujii, and S. Kashiwagi. *Journal of the Physical Society of Japan*, 64:2152, 1995.

[24] S. Picozzi, A. Continenza, and A. J. Freeman. *Phys. Rev. B*, 66:094421, 2002.

[25] Y. Miura, K. Nagao, and M. Shirai. *Phys. Rev. B*, 69:144413, 2004.

[26] K.R.A. Ziebeck and P.J. Webster. *J. Phys. F*, 5:1756, 1975.

[27] P.J. Webster and R.S. Tebbel. *J. Appl. Phys*, 39:471, 1968.

[28] P.J. Webster. *J. Phys. Chem. Sol.*, 32:1221, 1971.

[29] K.H.J. Buschow and P.G. van Engen. *J. Magn. Mag. Mat.*, 25:90, 1983.

[30] J. Kübler, A. R. Williams, and C. B. Sommers. *Phys. Rev. B*, 28:1745, 1983.

[31] I. Galanakis and P.H. Dederichs. Half-metallicity and Slater-Pauling Behavior in the Ferromagnetic Heusler Alloys. In P.H. Dederichs and J. Galanakis, editors, *Half-metallic Alloys - Fundamentals and Applications*, Lecture Notes in Physics. Springer, 2005.

[32] K.H.J. Buschow and M. Erman. *J. Magn. Magn. Mat.*, 30:374, 1983.

[33] J. Pierre, R.V. Skolozdra, and Yu. V. Stadnyk. *J. Magn. Magn. Mat.*, 128:93, 1993.

[34] Y. Nishino, M. Kato, S. Asano, K. Soda, M. Hayasaki, and U. Mizutani. *Phys. Rev. Lett.*, 79:1909, 1997.

[35] A. Siebarski, M. B. Maple, E. J. Freeman, C. Sirvent, D. Tworuszka, M. Orzechowska, A. Wrona, A. Jezierski, S. Chiuzbaian, and M. Neumann. *Phys. Rev. B*, 62:3296, 2000.

[36] H. Okamura, J. Kawahara, T. Nanba, S. Kimura, K. Soda, U. Mizutani, Y. Nishino, M. Kato, I. Shimoyama, H. Miura, K. Fukui, K. Nakagawa, H. Nakagawa, and T. Kinoshita. *Phys. Rev. Lett.*, 84:3674, 2000.

[37] R. de Groot and P. van Engen. *Phys. Rev. Lett.*, 50:2024, 1983.

[38] S. Fujii, S. Sugimura, S. Ispida, and S. Asano. *J. Phys.: Cond. Matter*, 2:8583, 1990.

[39] S. Ishida, S. Kashiwagi, S. Fujii, and S. Asano. *Physica B*, 210:140, 1995.

[40] I. Galanakis, P. H. Dederichs, and N. Papnikolaou. *Phys. Rev. B*, 66:134428, 2002.

[41] K.E.H.M Hansen, P.R. Mijnarends, L.P.L.M. Rabou, and K.H.J. Buschow. *Phys. Rev. B*, 42:1533, 1990.

[42] M.J. Otto, R.A.M. van Woerden, P.J. van der Valk, J. Wijngaard, C.F. van Bruggen, and C. Haas. *J. Phys.: Cond. Matter*, 1:2351, 1989.

[43] C. Hordequin, J. Pierre, and R. Currat. *J. Magn. Magn. Mat.*, 162:75, 1996.

[44] M.M. Kirillova, A.A. Makhnev abd E.I. Shreder, V.P. Dyakina, and N.B. Gorina. *Phys. Stat. Sol (b)*, 187:231, 1995.

[45] R.J. Soulen, J.M. Byers, M.S. Osofsky, B. Nadgony, T. Ambrose, S.F. Cheng, P.R. Broussard, C.T. Tanaka, J. Nowak, J.S. Moodera, A. Barry, and J.M.D. Coey. *Science*, 282:85, 1998.

[46] P.J. Brown, K.U. Neumann, P.J. Webster, and K.R.A. Ziebeck. *J. Phys.: Cond. Matter*, 12:1827, 2000.

[47] L. Ritchie, G. Xiao, Y. Ji, T.Y. Chen, M. Zhang, C. L. Chien, M. Zhang, J. Chen, Z. Liu, G. Wu, and X.X. Zhang. *Phys. Rev. B*, 68:104430, 2003.

[48] D. Ristoiu, J. P. Nozieres, C. N. Borca, T. Komesu, H.-K. Jeong, and P. A. Dowben. *Europhys. Lett.*, 49:624, 2000.

[49] W. Zhu, B. Sinkovic, E. Vescovo, C. Tanaka, and J. S. Moodera. *Phys. Rev. B*, 64:060403(R), 2001.

[50] G.A. Prinz. *Science*, 282:1660, 1998.

[51] D. Awschalom and J. Kikkawa. *Physics Today*, 52:33, June 1999.

[52] I. Žutić, J. Fabian, and S. Das Sarma. *Rev. Mod. Phys.*, 76:323, 2004.

[53] S.A. Wolf, D.D. Awschalom, R.A. Buhrman, J.M. Daughton, S. von Molnar, M.L. Roukes, A.Y. Chtchelkanova, and D.M. Treger. *Science*, 294:5546, 2001.

[54] G. Schmidt, D. Ferrand, L.W. Molenkamp, A.T. Filip, and B.J. van Wees. *Phys. Rev. B*, 62:R4790, 2000.

[55] C. Cacho, Y. Lassailly, H.-J. Drouhin, G. Lampel, and J. Peretti. *Phys. Rev. Lett.*, 88:066601, 2002.

[56] B. Dieny. *J. Magn. Magn. Mater.*, 136:335, 1994.

[57] J. Moodera, R. Kinder, L. T. Wong, and R. Meservey. *Phys. Rev. Lett.*, 74:3273, 1998.

[58] Iosif Galanakis and Phivos Mavropoulos. *Phys. Rev. B*, 67:104417, 2003.

[59] S. Picozzi, A. Continenza, and A.J. Freeman. Role of Structural Defects on the Half-Metallic Character of Heusler Alloys and Their Junctions with Ge and GaAs. In P.H. Dederichs and J. Galanakis, editors, *Half-metallic Alloys - Fundamentals and Applications*, Lecture Notes in Physics. Springer, 2005.

[60] R. Meservey, D. Pereskevopoulus, and P.M. Tedrow. *Phys. Rev. Lett.*, 37:858, 1976.

[61] M. Julliere. *Phys. Lett.*, 54A:225, 1975.

[62] C. Hordequin, J.P. Nozieres, and J. Pierre. *J. Magn. Magn. Mat.*, 183:225, 1998.

[63] C. Tanaka, J. Novak, and J.S. Moodera. *J. Appl. Phys*, 81:5515, 1997.

[64] J. Schmalhorst, S. Kämmerer, M. Sacher, G. Reiss, A. Hütten, and A. Scholl. *Phys. Rev. B*, 70:024426, 2004.

[65] A. Hütten, S. Kämmerer, J. Schmalhorst, A. Thomas, and G. Reiss. *Phys. Stat. Sol. (a)*, 201:3271, 2004.

[66] A. Hütten, S. Kämmerer, J. Schmalhorst, and G. Reiss. Heusler Alloyed Electrodes Integrated in Magnetic Tunnel-Junctions. In P.H. Dederichs and J. Galanakis, editors, *Half-metallic Alloys - Fundamentals and Applications*, Lecture Notes in Physics. Springer, 2005.

[67] M. Yamamoto, T. Ishikawa, K. Matsuda, T. Uemura, and M. Arita. *J. Phys. D: Appl. Phys.*, 39:824, 2006.

[68] T. Marukame, T. Kasahara, K. Matsuda, T. Uemra, and M. Yamamoto. *Japan. J. Appl. Phys.*, 44:L521, 2005.

[69] T. Marukame, T. Kasahara, K. Matsuda, T. Uemra, and M. Yamamoto. *IEEE Trans. Magn.*, 41:2603, 2005.

[70] K. Inomata, S. Okamura, A. Miyazaki, M. Kikuchi, N. Tezuka, M. Wojcik, and E. Jedryka. *J. Phys. D: Appl. Phys.*, 39:816, 2006.

[71] E. Clifford, M. Venkatesan, R. Gunning, and J.M.D. Coey. *Solid State Commun.*, 131:61, 2004.

[72] T. Ambrose and O. Mryasov. Growth and Magnetotransport Properties of Thin Co_2MnGe Layered Structures. In P.H. Dederichs and J. Galanakis, editors, *Half-metallic Alloys - Fundamentals and Applications*, Lecture Notes in Physics. Springer, 2005.

[73] T. Ambrose, J. J. Krebs, and G. A. Prinz. *J. Appl. Phys.*, 89:7522, 2001.

[74] K. Westerholt, A. Bergmann, J. Grabis, A. Nefedov, and H. Zabel. Magnetism and Structure of Multilayers Based on the Fully Spin Polarized Heusler Alloys Co_2MnGe and Co_2MnSn. In P.H. Dederichs and J. Galanakis, editors, *Half-metallic Alloys - Fundamentals and Applications*, Lecture Notes in Physics. Springer, 2005.

[75] E.E. Fullerton, M.J. Cobover, J.E. Mattson, C.H. Sowers, and S.D. Bader. *Appl. Phys. Lett.*, 63:1699, 1993.

Bibliography

[76] R. Fiederling, M. Keim, G. Reuscher, W. Ossau, G. Schmidt, A. Waag, and L.W. Molenkamp. *Nature*, 76:323, 1999.

[77] Y. Ohno, D.K. Young, B. Beschoten, F. Matsukura, H. Ohno, and D.D. Awschalom. *Nature*, 402:790, 1999.

[78] X. Jiang, R. Wang, S. van Dijken, R. Shelby, R. Macfarlane, G. S. Solomon, J. Harris, and S.S.P. Parkin. *Phys. Rev. Lett.*, 90:256603, 2003.

[79] J. Strand, B.D. Schultz, A.F. Isakovic, C.J. Palmstrøm, and P.A. Crowell. *Phys. Rev. Lett.*, 91:036602, 2003.

[80] W. Van Roy and M. Wójcik. Epitaxial Growth of NiMnSb on GaAs by Molecular Beam Epitaxy. In P.H. Dederichs and J. Galanakis, editors, *Half-metallic Alloys - Fundamentals and Applications*, Lecture Notes in Physics. Springer, 2005.

[81] X.Y. Dong, C. Adelmann, J.Q. Xie, C.J. Palmstrøm, X. Lou, J. Strand, P.A. Crowell, J.-P. Barnes, and A.K. Petford-Long. *Appl. Phys. Lett.*, 86:102107, 2005.

[82] B. Ravel, J.O. Cross, M.P. Raphael, V.G. Harris, R. Ramesh, and V. Saraf. *Appl. Phys. Lett.*, 81:2812, 2002.

[83] H.J. Elmers, G.H. Fecher, D. Valdaitsev, S.A. Nepijko, A. Gloskovskii, G. Jakob, G. Schönhense, S. Wurmehl, T. Block, C. Felser, P.-C. Hsu, W.-L. Tsai, and S. Cramm. *Phys. Rev. B*, 67:104412, 2003.

[84] C. Felser, H.-J. Elmers, and G.H. Fecher. The Properties of $Co_2Cr_{1-x}Fe_xAl$ Heusler Compounds. In P.H. Dederichs and J. Galanakis, editors, *Half-metallic Alloys - Fundamentals and Applications*, Lecture Notes in Physics. Springer, 2005.

[85] H. Ebert and G. Schütz. *J. Appl. Phys.*, 69:4627, 1991.

[86] D. Orgassa, H. Fujiwara, T. C. Schulthess, and W. H. Butler. *Phys. Rev. B*, 60:13237, 1999.

[87] T. Ambrose, J.J. Krebs, and G.A. Prinz. *J. Appl. Phys.*, 87:5463, 2000.

[88] C. M. Fang, G.A. de Wijs, and R.A. de Groot. *J. Appl. Phys.*, 91:8340, 2002.

[89] I. Galanakis. *J. Phys.: Condens. Matter*, 14:6329, 2002.

[90] G.A. de Wijs and R.A. de Groot. *Phys. Rev. B*, 64:020402, 2001.

[91] S.J. Jenkins. *Phys. Rev. B*, 70:245401, 2004.

[92] S. Ishida, T.Masaki, S. Fujii, and S. Asano. *Physica B*, 245:1, 1998.

[93] A. Debernadi, M. Peressi, and A. Baldereschi. *Mat. Sci. Eng. C*, 23:743, 2003.

[94] I. Galanakis, P. Mavropoulos, and P.H. Dederichs. *J. Phys. D: Appl. Phys.*, 39:765, 2006.

[95] S. Picozzi, A. Continenza, and A. J. Freeman. *J. Appl. Phys.*, 94:4723, 2003.

[96] In P.A. Dowben and A. Miller, editors, *Surface Segregation Phenomena*, page 145. CRC Press, Boston, 1990.

[97] H.-K. Jeong, A. Caruso, and C.N. Borca. Surface Segregation and Compositional Instability at the Surface of Half-Metal Ferromagnets and Related Compounds. In P.H. Dederichs and J. Galanakis, editors, *Half-metallic Alloys - Fundamentals and Applications*, Lecture Notes in Physics. Springer, 2005.

[98] J. A. Mydosh. *J. Magn. Magn. Mat.*, 157/158:606, 1996.

[99] A.F.J. Morgownik and J.A. Mydosh. *Solid State Commun.*, 47:321, 1983.

[100] V. Cannella and J.A. Mydosh. *Phys. Rev. B*, 6:4220, 1972.

[101] K. Binder and A.P. Young. *Rev. Mod. Phys.*, 58:801, 1986.

[102] J.K. Srivastava. *Phys. Stat. Sol. (b)*, 210:159, 1998.

[103] D. X. Li, S. Nimori, Y. Shiokawa, Y. Haga, E. Yamamoto, and Y. Onuki. *Phys. Rev. B*, 68:172405, 2003.

[104] W. Luo, S. R. Nage, T. F. Rosenbaum, and R. E. Rosensweig. *Phys. Rev. Lett.*, 19:2721, 1991.

[105] P. M. Shand, A. D. Christianson, T. M. Pekarek, L. S. Martinson, J. W. Schweitzer, I. Miotkowski, and B. C. Crooker. *Phys. Rev. B*, 58:12876, 1998.

[106] S. Nakashima, K. Fujita, K. Tanaka, and K. Hirao. *J. Phys.: Condens. Matter*, 17:137, 2005.

[107] N. Veglio, F. J. Bermejo, J. Gutierrez, J. M. Barandiarán, A. Peña, M. A. González, P. P. Romano, and C. Mondelli. *Phys. Rev. B*, 71:212402, 2005.

Bibliography

[108] G.S.Patrin, V.O. Vas'kovskii, D.A. Velikanov, A.V. Svalov, and M.A. Panova. *Phys. Lett. A*, 309:155, 2003.

[109] J. Dho, W.S. Kim, and N.H. Hur. *Phys. Rev. Lett.*, 89:027202, 2002.

[110] W.R. Chen, F.C. Zhang, J. Miao, B. Xu, X.L. Dong, L.X. Cao, X.G. Qiu, and B.R. Zhao. *Appl. Phys. Lett.*, 87:042508, 2005.

[111] J. A. Mydosh. *Spin glasses : An Experimental Introduction*. London: Taylor & Francis, 1993.

[112] K. Westerholt and H. Bach. *Phys. Rev. Lett.*, 47:1925, 1981.

[113] M.A. Rudermann and C. Kittel. *Phys. Rev.*, 96:99, 1954.

[114] H. Maletta, G. Aeppli, and S.M. Shapiro. *Phys. Rev. Lett.*, 48:1490, 1982.

[115] G. Aeppli, S.M. Shapira, H. Maletta, R.J. Birgenau, and H.S. Chen. *J. Appl. Phys.*, 55:1628, 1984.

[116] B.D. Culity. *Introduction to Magnetic Materials*. Addison-Wesley, London, 1972.

[117] A.F.J. Morgownik and J.A. Mydosh. *Phys. Rev. B*, 24:5277, 1981.

[118] K.V. Rao, M. Fähnle, E. Figueroa, O. Beckman, and L. Hedman. *Phys. Rev. B*, 27:3104, 1983.

[119] C.A.M. Mulder, A.J. Duyneveldt, and J.A. Mydosh. *Phys. Rev. B*, 23:1384, 1981.

[120] S. Nagata, P.H. Keesom, and H.R. Harrison. *Phys. Rev. B*, 19:1633, 1979.

[121] R.W. Knitter and J.S. Kouvel. *J. Magn. Magn. Mater.*, 15-18:173, 1980.

[122] R. V. Chamberlin, M. Hardiman, L. A. Turkevich, and R. Orbach. *Phys. Rev. B*, 25:6720, 1982.

[123] P. Monod and H. Bouchiat. *J. Phys. Lett.*, 43:145, 1982.

[124] C. M. Soukoulis, K. Levin, and G.S. Grest. *Phys. Rev. B*, 28:1495, 1983.

[125] P. Monod, J.J. Prejean, and B. Tissier. *J. Appl. Phys.*, 50:7324, 1979.

[126] J.J. Prejean and J. Souletie. *J. Phys.*, 41:1335, 1980.

[127] J. Chadwick. *Nature*, 129:312, 1932.

[128] D. Richter. Properties of the neutron, elementary scattering processes. In T. Brückel, G. Heger, and D. Richter, editors, *Neutron Scattering*, Matter and Materials, Vol. 5. Schriften des Forschungszentrums Jülich, 2000.

[129] M.S. Deweyand and J.E.G.Kessler. *J. Res. Natl. Inst. Stand. Technol.*, 105:11, 2000.

[130] G.L. Squires. *Introduction to the theory of thermal neutron scattering.* Cambridge University Press, Cambridge, 1978.

[131] J.J. Sakurai. *Modern Quantum Mechanic.* Addison-Wesley, Reading, 1994.

[132] T. Fließbach. *Quantenmechanik.* Spektrum Akademischer Verlag, Heidelberg, 1995.

[133] V.F. Sears. *Neutron Optics.* Oxford University Press, Oxford, 1989.

[134] T. Brückel and W. Schweika, editors. *Polarized Neutron Scattering.* Forschungszentrum Jülich, Jülich, 2002.

[135] S.W. Lovesey. *Theory of neutron scattering from condensed matter*, volume 2. Clarendon Press, Oxford, 1987.

[136] G.E. Bacon. *Neutron Diffraction.* Clarendon Press, Oxford, 1975.

[137] J. Als-Nielson and D. McMorrow. *Elements of Modern X-Ray Physics.* Wiley, 2001.

[138] L. G. Parratt. *Phys. Rev.*, 95:359, 1954.

[139] L. Nevot and P. Croce. *Rev. Phys. Appl.*, 15:761, 1980.

[140] H. Zabel and K. Theis-Bröhl. *J. Phys.: Condens. Matter*, 15:S505, 2003.

[141] G.P. Felcher, R.O. Hilleke, R.K. Crawford, J. Haumann, R. Kleb, and G. Ostrowski. *Rev. Sci. Instrum.*, 58:609, 1987.

[142] C.F. Majkrzak. *Physica B*, 156,157:619, 1989.

[143] C.F. Majkrzak. *Physica B*, 173:75, 1991.

[144] F. Radu and V.K. Ignatovich. *Physica B*, 268:175, 1999.

[145] A. Rühm, B.P. Toperverg, and H. Dosch. *Phys. Rev. B*, 60:16073, 1999.

Bibliography

[146] B. P. Toperverg. *Physica B*, 297:160, 2001.

[147] B.P. Toperverg, A. Rühm, W. Donner, and H. Dosch. *Physica B*, 267-268:198, 1999.

[148] B.P. Toperverg. Polarized Neutron Reflection and Off-specular Scattering. In Th. Brückel and W. Schweika, editors, *Polarized Neutron Scattering*, Matter and Materials, Vol. 12. Schriften des Forschungszentrums Jülich, 2002.

[149] S.A. Stepanov and R. Köhler. *J. Appl. Phys.*, 76:7809, 1994.

[150] S. K. Sinha, E. B. Sirota, S. Garoff, and H. B. Stanley. *Phys. Rev. B*, 38:2297, 1988.

[151] S. K. Sinha. *J. Phys. III*, 4:1543, 1994.

[152] J. P. Schlomka, M. Tolan, L. Schwalowsky, O. H. Seeck, J. Stettner, and W. Press. *Phys. Rev. B*, 51:2311, 1995.

[153] V. Holy and T. Baumbach. *Phys. Rev. B*, 49:10668, 1994.

[154] D. E. Savage, J. Kleiner, N. Schimke, Y.-H. Phang, T. Jankowski, J. Jacobs, R. Kariotis, and M. G. Lagally. *J. Appl. Phys.*, 69(3):1411, 1991.

[155] N. Mott and H.S.W. Messey. *The Theory of Atomic Collisions*. Clarendon Press, Oxford, 1965.

[156] R. Siebrecht, A. Schreyer, U. English, U. Pietsch, and H. Zabel. *Physica B*, 241-243:169, 1998.

[157] M. Faraday. *Phil. Trans. Roy. Soc.*, 136:1, 1846.

[158] J. Kerr. *Phil. Mag.*, 3:321, 1877.

[159] H.-C. Mertins, S. Valencia, D. Abramsohn, A. Gaupp, W. Gudat, and P. M. Oppeneer. *Phys. Rev. B*, 69:064407, 2004.

[160] H.-C. Mertins, D. Abramsohn, A. Gaupp, F. Schäfers, and W. Gudat. *Phys. Rev. B*, 66:184404, 2002.

[161] C. Kao, J. B. Hastings, E. D. Johnson, D. P. Siddons, G. C. Smith, and G. A. Prinz. *Phys. Rev. Lett.*, 65:373, 1990.

[162] J. L. Erskine and E. A. Stern. *Phys. Rev. B*, 12:5016, 1975.

[163] G. Schütz, W. Wagner, W. Wilhelm, P. Kienle, R. Zeller, R. Frahm, and G. Materlik. *Phys. Rev. Lett.*, 58:737, 1987.

[164] P. Carra, B. T. Thole, M. Altarelli, and X. Wang. *Phys. Rev. Lett.*, 70:694, 1993.

[165] B. T. Thole, P. Carra, F. Sette, and G. van der Laan. *Phys. Rev. Lett.*, 68:1943, 1992.

[166] D. McMorrow J. Als-Nielsen. *Modern X-Ray Physics.* John Wiley & Son , Ltd, 2001.

[167] S. W. Lovesey and S. P. Collins. *X-ray Scattering and Absorption by Magnetic Materials.* Oxford Series on Synchrotron Radiation. Oxford University Press, 1996.

[168] P. Carra and M. Altarelli. *Phys. Rev. Lett.*, 64:1286, 1990.

[169] M. Blume. *J. Appl. Phys.*, 57:3615, 1985.

[170] J. B. Kortright and S.-K. Kim. *Phys. Rev. B*, 62:12216, 2000.

[171] R. W. James. *The Optical Principles of the Diffraction of X-Rays.* Oxbow Press, 1982.

[172] J. M. Tonnerre, L. Seve, D. Raoux, G. Soullie, B. Rodmacq, and P. Wolfers. *Phys. Rev. Lett.*, 75:740, 1995.

[173] N. Jaouen, J.M. Tonnerre, D. Raoux, E. Bontempi, L. Ortega, M. Müenzenberg, W. Felsch, A. Rogalev, H.A. Dürr, E. Dudzik, G. van der Laan, H. Maruyama, and M. Suzuki. *Phys. Rev. B*, 66:134420, 2002.

[174] J. Geissler, E. Goering, M. Justen, F. Weigand, G. Schütz, J. Langer, D. Schmitz, H. Maletta, and R. Mattheis. *Phys. Rev. B*, 65:020405(R), 2002.

[175] D. R. Lee, S. K. Sinha, D. Haskel, Y. Choi, J. C. Lang, S. A. Stepanov, and G. Srajer. *Phys. Rev. B*, 68:224409, 2003.

[176] D. R. Lee, S. K. Sinha, C. S. Nelson, J. C. Lang, C. T. Venkataraman, G. Srajer, and R. M. Osgood III. *Phys. Rev. B*, 68:224410, 2003.

[177] J. Zak, E. R. Moog, C. Liu, and S. D. Bader. *J. Magn. Magn. Mat.*, 89:107, 1990.

[178] J. Zak, E. R. Moog, C. Liu, and S. D. Bader. *Phys. Rev. B*, 43:6423, 1991.

[179] J. Zak, E. R. Moog, C. Liu, and S. D. Bader. *Phys. Rev. B*, 46:5883(E), 1992.

Bibliography

[180] J. Grabis. *Soft X-ray Resonant Scattering from Magnetic Heterostructures.* PhD thesis, Ruhr-Universität Bochum, 2005.

[181] R. M. Osgood III, S. K. Sinha, J. W. Freeland, Y. U. Idzerda, and S. D. Bader. *J. Magn. Magn. Mat.*, 198-199:698, 1999.

[182] J. Grabis, A. Bergmann, A. Nefedov, K.Westerholt, and H. Zabel. *Phys. Rev. B*, 72:024438, 2005.

[183] C. S. Nelson, G. Srajer, J. C. Lang, C. T. Venkataraman, S. K. Sinha, H. Hashizume, N. Ishimatsu, and N. Hosoito. *Phys. Rev. B*, 60:12234, 1999.

[184] J. W. Freeland, K. Bussmann, Y. U. Idzerda, and C. C. Kao. *Phys. Rev. B*, 60:R9923, 1999.

[185] J. Grabis, A. Nefedov, and H. Zabel. *Rev. Sci. Instr.*, 74:4048, 2003.

[186] U. Geiersbach, A.Bergmann, and K.Westerholt. *J. Magn. Magn. Mater.*, 240:546, 2002.

[187] U. Geiersbach, A. Bergmann, and K. Westerholt. *Thin Solid Films*, 425:226, 2003.

[188] B. E. Warren. *X-ray diffraction.* New York, Dover Publications, Inc., 1990.

[189] M. Goto, T. Kamimori, H. Tange, K. Kitao, S. Tomioshi, K. Ooyama, and Y. Yamaguchi. *J. Magn. Magn. Mater.*, 140-145:277, 1995.

[190] J. Stöhr. *J. Magn. Magn. Mater.*, 200:470, 1999.

[191] I. Galanakis, P. H. Dederichs, and N. Papanikolaou. *Phys. Rev. B*, 66:174429, 2002.

[192] H. A. Dürr, G. van der Laan, D. Spanke, F. U. Hillebrecht, and N. B. Brookes. *Phys. Rev. B*, 56:8156, 1997.

[193] J. Grabis, A. Bergmann, A. Nefedov, K. Westerholt, and H. Zabel. *Phys. Rev. B*, 72:024437, 2005.

[194] U. Geiersbach, A.Bergmann, and K.Westerholt. *J. Magn. Magn. Mater.*, 240:546, 2002.

[195] H. Zabel. *Appl. Phys. A*, 58:159, 1994.

[196] S. K. Sinha, E. B. Sirota, S. Garoff, and H. B. Stanley. *Phys. Rev. B*, 38:2297, 1988.

[197] Z.H. Mingh, A. Krol, Y.L. Soo, Y.H. Kao, J.S. Park, and K.L.Wang. *Phys. Rev. B*, 47:16373, 1993.

[198] L. Seve, N. Jaouen, J. M. Tonnerre, D. Raoux, F. Bartolome, M. Arend, W. Felsch, A. Rogalev, J. Goulon, C. Gautier, and J. F. Berar. *Phys. Rev. B*, 60:9662, 1999.

[199] D. Lott. *Magnetic X-ray Reflectivity*. PhD thesis, Ludwig-Maximilians-Universität München, 2001.

[200] J. E. Prieto, F. Heigl, O. Krupin, G. Kaindl, and K. Starke. *Phys. Rev. B*, 68:134453, 2003.

[201] K.-E. Peiponen, E. M. Vartiainen, and T. Asakura. *Dispersion, Complex Analysis and Optical Spectroscopy*, volume 147 of *Springer Tracts in Modern Physics*. Springer, 1999.

[202] B. L. Henke, E. M. Gullikson, and J. C. Davis. *At. Data Nucl. Data Tables*, 54:180, 1993.

[203] S. Picozzi, A. Continenza, and A. J. Freeman. *Phys. Rev. B*, 69:094423, 2004.

[204] J. F. MacKay, C. Teichert, D. E. Savage, and M. G. Lagally. *Phys. Rev. Lett.*, 77:3925, 1996.

[205] J. Schmalhorst, S. Kämmerer, M. Sacher, G. Reiss, A. Hütten, and A. Scholl. *Phys. Rev. B*, 70:024426, 2004.

[206] M. Oogane, J. Nakata, H. Kubota, Y. Ando, A. Sakuma, and T. Miyazaki. *Jap. J. Appl. Phys. Part 2*, 44:L760, 2005.

[207] A. Scheyer, R. Siebrecht, U. English, U. Pietsch, and H. Zabel. *Physica B*, 267-268:355, 1999.

[208] H. Dosch, K. Alusta, A. Lied, W. Drexel, and J. Peisl. *Rv. Sci. Instrum.*, 63:5533, 1992.

[209] U. Rücker E. Kentzinger and B.P. Toperverg. *Physica B*, 335:82, 2003.

[210] A. Hubert and R. Schäfer. *Magnetic Domains. The Analysis of Magnetic Microstructures*. Springer, Berlin-Heidelberg-New York, 1998.

Bibliography

[211] V. Lauter-Pasyuk, H. J. Lauter, B. P. Toperverg, L. Romashev, and V. Ustinov. *Phys. Rev. Lett.*, 89:167203, 2002.

[212] A. Delapalme, J. Schweizer, G. Couderchon, and R. Perrier de la Bathie. *Nucl. Instr. amd Meth. A*, 95:589, 1994.

[213] A. Bartélémy, A. Fert, M.N. Baibich, S. Hadjoudj, F. Petroff, P. Etienne, R. Cabanel, S. Lequien, F. Nguyen Van Dau, and G. Creuzet. *J. Appl. Phys.*, 67:5908, 1990.

[214] D.E. Bürgler, P. Grünberg, S.O. Demokritov, and M.T. Johnson. Interlayer exchange coupling in layered magnetic structures. In K.H.J. Buschow, editor, *Handbook of Magnetic Materials, Vol. 13*. Elsevier, Amsterdam, 2002.

[215] L. Wang, J. Ding, Y. Li, Y. P. Feng H. Z. Kong, and W. Z. Wang. *J. Phys.: Condens. Matter*, 12:4253, 2000.

[216] F. Wiekhorst, E. Shevchenko, H. Weller, and J. Kötzler. *Phys. Rev. B*, 22:224416, 2003.

[217] K.H. Fischer. *Phys. Stat. Sol. B*, 120:13, 1985.

[218] D. Altbir, M. Kiwi, R. Ramírez, and I. K. Schuller. *J. Magn. Magn. Mat.*, 149:L246, 1995.

[219] J. P. Hill and D. F. McMorrow. *Acta Cryst. A*, 52:236, 1996.

[220] J. C. Slonczewski. *J. Magn. Magn. Mater.*, 150:13, 1995.

[221] J. A. Borchers, P. M. Gehring, R. W. Erwin, J. F. Ankner, C. F. Majkrzak, T. L. Hylton, K. R. Coffey, M.A. Parker, and J. K. Howard. *Phys. Rev. B*, 54:9870, 1996.

[222] L. Néel. *Cr. Hebd. Acad. Sci.*, 255:1676, 1962.

[223] J. A. Borchers, J. A. Dura, J. Unguris, D. Tulchinsky, M. H. Kelley, C. F. Majkrzak, S. Y. Hsu, R. Loloee, W. P. Pratt, Jr. Bass, and J. Bass. *Phys. Rev. Lett.*, 82:2796, 1999.

[224] C. Rehm, D. Nagengast, F. Klose, H. Maletta, and A. Weidinger. *Europhys. Lett.*, 38:61, 1997.

List of publications

1. A. Bergmann, J. Grabis, A. Nefedov, K. Westerholt, H. Zabel, *X-ray resonant magnetic scattering study of $[Co_2MnGe/Au]_n$ and$[Co_2MnGe/V]_n$ multilayers, J. Phys. D: Appl. Phys.*, **39**, 842 (2006).

2. F. Radu, A. Nefedov, J. Grabis, G. Nowak, A. Bergmann, H. Zabel, *Soft X-ray resonant magnetic scattering studies on Fe/CoO exchange bias system, JMMM*, **300**, 206 (2006).

3. A. Bergmann, J. Grabis, B.P. Toperverg, V. Leiner, M. Wolff, H. Zabel, K. Westerholt, *Antiferromagnetic dipolar ordering in $[Co_2MnGe/V]_N$ multilayers, Phys. Rev. B*, **72**, 214403 (2005).

4. K. Westerholt, A. Bergmann, J. Grabis, A. Nefedov, H. Zabel, *Magnetism and structure of magnetic multilayers based on the fully spin polarized Heusler alloys Co_2MnGe and Co_2MnSn* in: *Half-metallic Alloys*, Lecture Notes in Physics, Springer 2005.

5. J. Grabis, A. Bergmann, A. Nefedov, K. Westerholt, H. Zabel, *Element-specific x-ray circular magnetic dichroism of Co_2MnGe Heusler thin films, Phys. Rev. B*, **72**, 024437 (2005).

6. J. Grabis, A. Bergmann, A. Nefedov, K. Westerholt, H. Zabel, *Element-specific characterization of the interface magnetism in $[Co_2MnGe/Au]_n$ multilayers by x-ray resonant magnetic scattering, Phys. Rev. B*, **72**, 024438 (2005).

7. A. Nefedov, J. Grabis, A. Bergmann, F. Radu, and H. Zabel, *X-ray resonant magnetic scattering of Fe/Cr superlattices, Superlattices and Microstructures*, **37**, 99 (2005).

8. A. Bergmann, J. Grabis, V. Leiner, M. Wolff, H. Zabel, K. Westerholt, *Spin polarized neutron reflectivity measurements on Heusler $[Co_2MnGe/V]_n$ multilayers, Superlattices and Microstructures*, **34**, 137 (2003).

9. A. Nefedov, J. Grabis, A. Bergmann, K. Westerholt, H. Zabel, *Soft X-ray resonant magnetic scattering studies on Co_2MnGe Heusler films, Physica B*, **345**, 250 (2003).

Publications

10. U. Geiersbach, A. Bergmann, K. Westerholt, *Preparation and structural properties of thin films and multilayers of the Heusler compounds Cu_2MnAl, Co_2MnSn, Co_2MnSi and Co_2MnGe, Thin Solid Films*, **425**, 225 (2003).

11. K. Westerholt, U. Geiersbach, A. Bergmann, *Exchange bias in $[Co_2MnGe/Au]_n$, $[Co_2MnGe/Cr]_n$ and $[Co_2MnGe/Cu_2MnAl]_n$ multilayers, JMMM*, **257**, 239 (2003).

12. U. Geiersbach, A. Bergmann, K. Westerholt, *Structural, magnetic and magnetotransport properties of thin films of the Heusler alloys Cu_2MnAl, Co_2MnSi, Co_2MnGe and Co_2MnSn, JMMM*, **240**, 546 (2003).

Danksagung

Von Herzen möchte ich allen danken, die zum erfolgreichen Gelingen dieser Arbeit beigetragen haben, besonders danke ich:

- Herrn Prof. Dr. K. Westerholt für die interessante Themenstellung und die engagierte Betreuung. Sein stets offenes Ohr für Probleme aller Art und seine Diskussionsbereitschaft haben wesentlich zum Erfolg der Arbeit beigetragen.

- Herrn Prof. Dr. Dr. h.c. H. Zabel für die Ermöglichung dieser Arbeit, die wissenschaftliche Unterstützung und die anregenden Diskussionen.

- Frau Dr. K. Theis-Bröhl, Herrn Dr. J. Grabis, Herrn Dr. M. Ay, Herrn Dr. A. Nefedov, Herrn Dr. A. Remhof, Herrn Dr. T. Schmitte, Herrn Dr. V. Leiner, Herrn Dr. M. Wolff, Herrn Dr. F. Radu, Herrn A. Westphalen und Herrn G. Nowak für die freundschaftliche Zusammenarbeit, Hilfe bei gemeinsamen Experimenten und fruchtvollen Diskussionen in vielen Strahlzeiten.

- Herrn Dr. O. Seeck, Herrn Dr. T. Kachel, Herrn Dr. V. Leiner und Herrn Dr. M. Wolff für die Betreuung und reibungslose Organisation bei Strahlzeiten.

- Herrn Prof. Dr. B. Toperverg für seine Hilfe bei der Simulation von Neutronenstreuung.

- allen Mitgliedern des Lehrstuhls EP IV und der AG Oberflächenphysik für das angenehme Arbeitsklima.

- "Dr. h.c." H. Glowatzki für die gute Nachbarschaft und seine Lebensweisheiten abseits der Wissenschaft.

- Frau S. Erdt-Böhm, Herrn P. Stauche und Herrn J. Podschwadek für ihre jederzeitige Hilfsbereitschaft und die Präparation der Proben.

- Frau P. Hahn, Frau I. Bickmann, Frau I. Gottmannshausen und Frau C. Wulf für die (un)bürokratischen Hilfen.

- der Werkstatt unter Leitung von Herrn J. Meermann für ihre technische Kompetenz.

- Herrn Dr. J. Grabis, Herrn Dr. T. Vogel, Herrn Dr. M. Ay und Herrn T. Last für ihre Freundschaft und Unterstützung in allen Lebenslagen.

Danksagung

- Herrn Dr. J. Grabis und Herrn Dr. G. Poschmann für die Durchsicht des Manuskripts.

- meiner Freundin für ihre Motivationsbereitschaft und den Rückhalt.

- meinen Eltern für ihre liebevolle Unterstützung.

Lebenslauf

Name	Andre Bergmann
Geburtsdatum	6. Juni 1976
Geburtsort	Essen
Familienstand	ledig
1982 - 1986	Grundschule in Essen
1986 - 1995	Gymnasium Essen-Überruhr
Mai 1995	Abitur
1995 - 1996	Zivildienst
1996 - 2001	Studium der Physik an der Ruhr-Universität in Bochum
1998	Vordiplom
2000 - 2001	Diplomarbeit
	am Lehrstuhl für Experimentalphysik/ Festkörperphysik,
	Ruhr-Universität Bochum (Prof. Dr. Dr. h.c. H. Zabel),
	Thema: Ladungstransporteigenschaften von Schichtsystemen
	aus Heusler-Verbindungen
Juni 2001	Diplom
seit 9/2001	Wissenschaftlicher Mitarbeiter
	am Lehrstuhl für Experimentalphysik/ Festkörperphysik,
	Ruhr-Universität Bochum (Prof. Dr. Dr. h.c. H. Zabel)